J. Verschuur

Delft University of Technology

The impact of uncertain Antarctic ice sheet dynamics for future coastal erosion

A probabilistic approach for a data-scarce environment in the Caribbean

J. Verschuur

TU Delft

Koninklijk Nederlands Meteorologisch Instituut
Ministerie van Infrastructuur en Waterstaat

Koninklijk Nederlands Meteorologisch Instituut
Ministerie van Infrastructuur en Waterstaat

TU Delft

The impact of uncertain Antarctic ice sheet dynamics for future coastal erosion

A probabilistic approach for a data-scarce environment in the Caribbean

J. Verschuur

Delft University of Technology
Department of Hydraulic Engineering

MSc Thesis

Student number:	4275675	
Project duration:	Febuari 5, 2017 – September 14, 2017	
Thesis committee:	Dr. C.A. Katsman (chair),	Delft University of Technology
	Prof. dr. ir. S.G.J. Aarninkhof,	Delft University of Technology
	Dr. ir. S. de Vries,	Delft University of Technology
	Dr. D. Le Bars,	Royal Netherlands Meteorological Institute
	Prof. dr. S.S. Drijfhout	Royal Netherlands Meteorological Institute

This thesis will be publicly defended on the 14th of September, 2018

TU Delft Delft University of Technology

Koninklijk Nederlands Meteorologisch Instituut
Ministerie van Infrastructuur en Waterstaat

”And on that wave
we will all have to navigate,
all who are nourished
by the fruits of the Earth.”
- Carlo Rovelli in *’The Order of Time’*

On the cover: Sint Maarten’s famous Maho Beach completely washed away by the storm waves generated during Hurricane Irma (2017). ©Dutch Ministry of Defence

Abstract

Key Points

- Sea level rise projections are deeply uncertain due to the contribution of the Antarctic ice sheet, in particular the possibility of rapid disintegration of the ice sheet.
- For coastal management purposes, insight in low-probability but high-impact events is essential.
- Excluding rapid mass loss from impact studies into future coastal storm erosion and coastal recession may greatly underestimate the risk faced.
- Risk-averse coastal managers are prone to misconception about their level of safety set.

Sandy beaches comprise large parts of the world's shorelines and act as a natural buffer for many exposed people and assets that are concentrated in the coastal zone. Many coastal communities are vulnerable to the impact of sea-level rise (SLR) that can amplify the episodic erosion from storms and drive structural erosion. The way communities adapt to SLR hinge critically on future SLR projections. One of the major uncertainties is the potential rapid disintegration of large fractions of the Antarctic ice sheet (AIS) that can accelerate sea-level rise, albeit neglected in the latest SLR estimates of the 'Intergovernmental Panel on Climate Change (IPCC)'. Accounting for rapid AIS mass loss in coastal impact assessments is essential for risk-averse coastal managers that disfavour events with large consequences.

Although methods to predict future erosion estimates under SLR have been developed, hitherto no study has assessed the impact of different cases of AIS dynamics to erosion estimates. Here, a case-study to the island of Sint Maarten is considered to evaluate the implications for strategies to manage coastal erosion under SLR uncertainty. Regional SLR projections are made for a case consistent with the IPCC, a case with a skewed probability distribution function of the AIS dynamics and a high-end scenario of Antarctic mass loss. SLR projections are incorporated within a probabilistic erosion framework using synthetic storm time series for two beaches on the island. Future retreat distances from storms and long term coastal recession are calculated, and the different scenarios are compared and contrasted.

For a future 1/100 year retreat distance of storm erosion, often used for zoning policies, estimates may be exceeded up to 1.11-2.22 times as frequent for inclusion of skewness, and 2.22-67 times as frequent for the high-end scenario compared to the IPCC case. These numbers further increase when additional climate model uncertainty is introduced. In terms of long-term recession, the 1% exceedance probability in 2100 for the IPCC case has a 2-4.5 % exceedance probability for a skewed distribution function and a 37-88% exceedance probability under a high-end scenario of the AIS. Lower exceedance probabilities, essential for risk-averse coastal managers, are underestimated relatively more leading to potential disillusion about the safety level that is set.

In conclusion, precluding AIS uncertainty from SLR projections that feed coastal impact assessments may lead to ill-informed decisions on SLR adaptation. Risk-averse coastal managers should thus be better informed on deep uncertainty in SLR projections to prevent maladaptation of vulnerable areas.

Acknowledgements

This thesis marks the end of my master programme in Hydraulic Engineering. Although my focus during this master was on river and coastal engineering, I quickly realised that my interest is more broader than just the engineering viewpoint. This thesis resembles this and has, apart from the engineering scope, viewpoints from the field of climate research and decision-making. I can freely say that I have learned more than I had ever imagined over the last few months.

Personally, I think sea-level rise is one of the major challenges we face as a global society in terms of potential economic and environmental consequences, but also in terms of the ethical dilemmas it brings forward. This all makes adaptation to sea-level rise a purely interdisciplinary work environment. With this thesis, I hope to have brought the fields of climate research and coastal research a step closer together. I think that further cross-cutting research initiatives are needed to learn from each other and collaboratively move forward.

I also learned a few things about myself. Although I never considered a future career in academia, I now realize that I like it much more than I first though. Luckily, I had the freedom to develop my own research scope and thereby 'prove' to myself that I am able to frame a research scope that contributes (or at least I think it does) to the scientific body of literature. For the future, I hope to find myself in a role on the interface between science and policy, with a clear focus on climate change and decision-making under uncertainty.

I should acknowledge a few people who supported me during this research. First of all, I would like to thank Arjen Luijendijk for providing me with the satellite data of the shoreline. Second, I would like to acknowledge Rosh Ranasinghe. Rosh, I really appreciate the time and effort you took for meeting with me a few times to discuss this topic with me. I am also really grateful to my commission members for all fruitful discussions over the months. Stefan, Sierd and Sybren, thank you for the structural comments and discussions. Caroline, thanks a lot for being my chair and helping me with the necessary steps throughout the thesis period, and your thorough reading of my report. Dewi, I owe you a lot for given me the opportunity do a thesis research at KNMI, introducing me to a number of people, and in particular for all the time you spend hearing out my thoughts. I really enjoyed working with you and I look back with great pleasure on our discussions concerning sea-level rise, the philosophy of science and numerous other things.

At last, I am sincerely grateful for all others that directly or indirectly contributed to this work. This includes the people at KNMI for all laughs during lunch and coffee breaks. Daan and Brechtje, thanks for going through my research to check the consistency and grammar. Lars, thanks for helping me with some programming problems. Finally, credits to my friends and family for their mental support throughout the period.

Nomenclature

List of Abbreviations

AIS	Antarctic Ice Sheet
AR5	Assessment Report 5
CDF	Cumulative Distribution Function
CMIP5	Coupled Model Intercomparison Project Phase 5
CR	Coastal Recession
DB	Dawn Beach
ECDF	Empirical Cumulative Distribution Function
GIA	Glacial Isostatic Adjustment
GIC	Glaciers & Ice Caps
GIS	Greenland Ice Sheet
GMSL	Global Mean Sea-Level
GMST	Global Mean Surface Temperature
IPCC	Intergovernmental Panel on Climate Change
LW	Land Water Storage
MICI	Marine Ice Cliff Instability
MISI	Marine Ice Sheet Instability
OB	Orient Bay
PDF	Probabilistic Density Function
R	Retreat Distance
RCP	Representative Concentration Pathways
RSLR	Regional Sea-Level Rise
SDS	Satellite Derived Shoreline
SIDS	Small Island Developing States
SMB	Surface Mass Balance
SSTS	Synthetic Storm Time Series

Contents

1 Introduction

Sandy beaches comprise 31% of the world's ice-free shoreline (Luijendijk et al., 2018). Apart from their economic, environmental and aesthetic value, beaches function as natural buffer for hazardous events (e.g. storms), thereby protecting many people and assets located in the coastal zone (McGranahan et al., 2007, Hallegatte et al., 2013). Nowadays, 24% of the world's sandy beaches are in a state of erosion (Luijendijk et al., 2018), and sea-level rise (SLR) will inevitably exacerbate the retreat of shorelines (Stive, 2004, Ranasinghe and Stive, 2009, Hinkel et al., 2013, Anderson et al., 2015, FitzGerald et al., 2008). The design of coastal defence and zoning policies hinge critically on SLR projections, making them key information tools (Nicholls and Cazenave, 2010, Wong et al., 2017). However, SLR projections are deeply uncertain, in particular the uncertainty surrounding the potential rapid disintegration of the Antarctic ice sheet (AIS). The latest report (AR5) of the 'Intergovernmental Panel on Climate Change (IPCC)' projects end-century global mean sea-level (GMSL) rise to be 26-98 cm, depending on the climate scenario (Church et al., 2013). The IPCC, however, aims for scientific consensus and do not account for poorly understood mechanisms such as the AIS rapid dynamics (Horton et al., 2014, Bakker et al., 2017). Coastal managers tend to be risk-averse, disfavouring events with large consequences, and the IPCC-projections are found ill-suited for quantifying events with low-exceedance probabilities (Hinkel et al., 2015). Increased understanding of mechanisms that could destabilize the AIS and accelerate mass loss have been quantified over the years following AR5 (Ritz et al., 2015, Golledge et al., 2015, DeConto and Pollard, 2016). Recent SLR projections have focused on both including the latest understanding of the sensitivity of the AIS to climate change and better quantifying the upper tail of the distribution function (Jackson and Jevrejeva, 2016, Le Bars et al., 2017, Bakker et al., 2017, Kopp et al., 2017). These projections are better tailored for the needs of risk-averse coastal managers and yield substantially higher estimates of GMSL rise compared to the projections of the IPCC.

Regional sea-level rise (RSLR) departs from the global average in most regions due to spatial variability of local ocean processes and self-gravitational effect of mass loss from ice sheets (Slangen et al., 2014, Jevrejeva et al., 2016, Carson et al., 2016). The direct implication of this is that societies need to adapt differently to SLR, making adaptation an local issue.

1.1. Problem Statement

Beaches are dynamic systems that naturally exhibit a variety of periodicities and associated temporal and spatial scales (Stive et al., 2002). On time scales associated with storms, elevated water levels together with extreme waves initiate episodic retreat of the shoreline, after which recovery takes place. The traditional way to assess storm erosion is to force a numerical model with a design wave height in order to determine the

design storm erosion. Storm erosion is governed by factors such as storm surge, wave height, wave period, wave angle, duration (henceforth called storm parameters) and beach morphology (van Rijn, 2009). Storm parameters are however stochastic in nature and covary with each other (De Michele et al., 2007), making this approach erroneous (Callaghan et al., 2008). SLR will increase the frequency of extreme water levels (Tebaldi et al., 2012, Buchanan et al., 2017, Vitousek et al., 2017), and may therefore contribute to an amplification of storm-induced erosion (Ranasinghe, 2016).

On longer time-scales, SLR may cause structural erosion, or recession, of the beach. For instance, the widely applied 'Bruun Rule' governs the re-orientation of the active profile (between berm and closure depth) landward and upward to maintain its equilibrium shape, thereby moving sediment particles from onshore to offshore (Bruun, 1954). However this approach is widely scrutinized for its practicality (Cooper and Pilkey, 2004, Stive, 2004, Ranasinghe and Stive, 2009). Ranasinghe et al. (2012) came up with an alternative approach to model SLR-induced recession. It deviates from the 'Bruun Rule' by coupling the morphodynamic interaction of storm erosion and longer term recession. This is particularly useful since advanced numerical models are not yet suitable for long term coastal evolution modelling (Hanson et al., 2003, Ranasinghe, 2016). In addition, it has the advantage of providing probabilistic estimates of coastal recession. Apart from recession estimates, a similar methodology has been used to estimate probabilistic shoreline positions for the development of setback lines (zoning policy that prohibits development beyond a given shoreline position) (Jongejan et al., 2016), and probabilistic projections of dune erosion that serve the design of nourishment schemes (Li et al., 2014).

Given the potential billion dollars of assets at risk, effectively managing the coastal zone is essentially a risk-management issue that needs probabilistic projections of erosion risk to guide coastal managers in making risk-informed decisions (Cowell et al., 2006, Oppenheimer and Alley, 2016, Ranasinghe, 2016). Traditional approaches to determine coastal erosion are no longer adequate for this, as they only provide deterministic estimates, favouring approaches that can handle stochastic input. Moreover, SLR uncertainty including potential deep uncertainties in SLR projections should be explored and integrated into design practises. Deep uncertainty can be defined as the situation where "experts cannot agree upon or are not willing to provide probabilistic uncertainty ranges" (Lempert and Collins, 2007), with the AIS dynamics as a example of this. A simple and transparent way to present deep uncertainty is to provide the decision-maker with multiple plausible probability density functions of likely futures (Lempert and Collins, 2007). This is essential for quantifying the tail risks (i.e. events with low-probability but large consequences), which steer the mitigation alternatives and the perspective of the decision-maker (Kunreuther et al., 2013). Until now, the quantification and evaluation of erosion tails risks associated with SLR in a probabilistic framework is lacking in literature. Therefore, although the climate community has moved forward by providing sea-level information specifically for coastal management purposes, the coastal communities have not followed this trend accordingly.

1.2. Objective and research questions

Using the island of Sint Maarten as a case study, this study aims to better assess the role of SLR uncertainties for coastal erosion (both episodic and structural), with an emphasis on the uncertainty that arises from the potential contribution of the AIS to SLR. Moreover, this work aims to evaluate the implications for strategies to manage coastal erosion if AIS uncertainty is not included appropriately.

The following research questions are defined:

- How does regional sea-level rise in the Caribbean Sea evolve under different climatic forcings for the 21st century in the Caribbean Sea?
- What are the major contributors and uncertainties for regional sea-level rise in the Caribbean Sea?
- How does regional sea-level rise in the Caribbean Sea evolve under more extreme scenarios of mass loss from the Antarctic Ice Sheet?
- How does sea-level rise, including uncertainty, affect the episodic erosion from storms over the years in Sint Maarten?
- How does sea-level rise, including uncertainty, affect the structural erosion over the years in Sint Maarten?
- What are the differences between multiple plausible cases of Antarctic Ice Sheet dynamics in sea-level rise projections for future coastal erosion risk in Sint Maarten?

1.3. Approach

Three different cases of including the AIS dynamics in SLR projections are investigated; a case consistent with the latest report of the IPCC (Church et al., 2013), a skewed distribution function of AIS dynamics based on Levermann et al. (2014), and a high-end case based on DeConto and Pollard (2016). Probabilistic estimates of episodic storm erosion and long-term recession (hereafter referred to as erosion risk) of the shoreline are derived by considering an approach using synthetic storm time series (SSTS) that are fed into an analytical erosion model and shoreline prediction model. SSTS are based on observed time series of storm parameters and their interdependency to fit a multi-dimensional covariance model (i.e. copula) (Callaghan et al., 2008, Li et al., 2014, Wahl et al., 2016, Davies et al., 2017). With the SSTS, many plausible multi-variate storms can be sampled, which can be coupled to plausible SLR trajectories. The rationale of the erosion model used builds on previous work (Ranasinghe et al., 2012, Li et al., 2014), but the focus here is on the implications of SLR uncertainty for strategies to manage erosion risk.

For context, Sint Maarten lacks a tide gauge, wave buoy, nearshore bathymetry data and detailed validation data from beach measurements. A methodology is adopted that makes use of satellite-based products that have a global coverage. This makes it generic and easily applicable in other data-scarce environments, which is desirable given that coastal data is still a scarce good worldwide (Vafeidis et al., 2008). The numbers should, however, be interpreted as first-order magnitude estimates.

First, the recent developments in SLR research is outlined together with an introduction into behaviour of the shoreline on time scales relevant for SLR (Section 2.1-2.2). Thereafter, the interaction between climate research, coastal engineering and decision-making is described (Section 2.3-2.4). The case study to Sint Maarten is introduced (Section 3). Regional probabilistic SLR projections for three different cases of the AIS dynamics are constructed (Section 4.1). Two future emission scenarios are included, RCP4.5 and RCP8.5. These SLR projections are then combined with the SSTS and incorporated into a probabilistic erosion model to assess changes in erosion risk of the coast (Section 4.2). Finally, we compare and contrast the results for the different scenarios (Section 5) to evaluate the implications for decision-making to mitigate coastal erosion (Section 6). This is supported by a discussion (Chapter 7.1), way forward (Chapter 7.2), reproducibility and upscaling recommendations (Chapter 7.3) and conclusions of the research (Chapter 8).

2 Theoretical background

2.1. Sea-level rise: current observations

Global mean sea-level (GMSL) rise can be attributed to the summed changes of five components: ocean thermal expansion and mass loss from glaciers and small ice caps (GIC), the Greenland ice sheet (GIS), the Antarctic ice sheet (AIS) and land water storage (LW).

Using satellites, an acceleration of GMSL rise could be detected over the last 25 years (Chen et al., 2017, Nerem et al., 2018). These estimates are reported to be 3.0 mm yr^{-1} with an acceleration of 0.084 mm yr^{-2}, which is already more than double the estimates of the 20th century GMSL rise (e.g. Hay et al., 2015, Dangendorf et al., 2017). Over this 25 year period, ocean thermal expansion has accounted for almost 40% of the change, whereas mass loss from GIC and GIS have dominated the remaining part (Dieng et al., 2017). Anthropogenic forcing is now steering the current trend in SLR (Slangen et al., 2016), making future SLR strongly dependent on the future emission pathway taken (van Vuuren et al., 2011). Still, a certain residual SLR, or sea-level rise commitment, is inevitable due to system inertia (Levermann et al., 2013, Mengel et al., 2018).

Different methods to estimate GMSL rise have been developed ranging from semi-empirical models (Rahmstorf, 2007, Vermeer and Rahmstorf, 2009, Mengel et al., 2016), simple mechanically motivated models (Bakker et al., 2017, Mengel et al., 2018) up to process-based probabilistic approaches (Church et al., 2013, Kopp et al., 2014, Jevrejeva et al., 2014, Le Bars et al., 2017). On the one hand, process-based models use physical laws to model the individual physical mechanisms that contribute to SLR. This is usually a combination of climate models and models of other physical processes that are not yet incorporated in the climate models (e.g. GIC, GIS and AIS). On the other hand, semi-empirical models are statistical models that directly link GMSL rise to the global mean surface temperature (GMST), or top of atmosphere radiative balance. This model is then directly forced by future temperature.

2.1.1. The Antarctic ice sheet

The largest source of uncertainty is the contribution of the AIS to GMSL. The AIS holds a total volume of ~65 m of SLR-equivalent (Church et al., 2013). Studies that predict the end-century contribution deviate significantly ranging from 0.2 up to more than 1.0 meter (left panel Figure 2.2). The deviation is due to differences in predicting the behaviour of recently discovered mechanisms that could lead to rapid disintegration of the ice sheet, inherent model uncertainties and due to difficulties in calibrating the models with observations (Fuller et al., 2017). In particular, the West Antarctic Ice Sheet (WAIS) is vulnerable and ongoing recession of the marine ice sheet may trigger a possible collapse as a result of anthropogenic warming (Rignot, 1998).

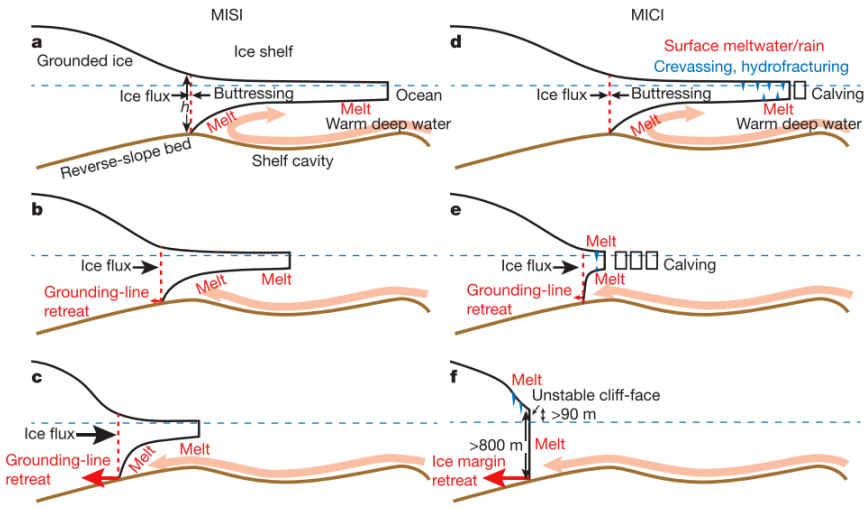

Figure 2.1: On the left, the Marine Ice Sheet Instability (MISI). Warm ocean water penetrates underneath the ice shelf, causing retreat of the groundline line. The retreat under a reverse-sloping bed results in increased ice flux. Right the Marine Ice Cliff Instability (MICI). Calving of ice cliff when reaching an aerial elevation of 90m causes larger elevation ice cliffs to fail as well. Reinforced by surface melt and crevasses at the surface. Both adopted from DeConto and Pollard (2016)

The marine terminating ice-shelves that surround the WAIS are in direct contact with ocean. Increased melt underneath the ice-shelves (basal melt) due to an influx of warm ocean water can drive dynamic ice sheet loss and retreat of the grounding line (junction shelf and bedrock). Theory suggest that ice flux at the grounding line is strongly dependent on ice thickness there, so a thicker ice layer leads to a larger ice flux. If on a reverse bed slope, the process can lead to a runaway feedback causing the ice to become rapidly unstable, known as the Marine Ice Sheet Instability (MISI, Figure 2.1a-c) (Ritz et al., 2015). Evidence suggest that this mechanisms has contributed to mass loss in the WAIS (Joughin et al., 2014, Favier et al., 2014). Studies that included MISI into their model have estimated future SLR from Antarctic dynamics alone to be 2.3-46 cm (Ritz et al., 2015) or 0.1-0.39 cm (Golledge et al., 2015) (both 5-95%) in 2100. Another potential runaway feedback is known as the Marine Ice Cliff Instability (MICI, Figure 2.1d-f). This process can be initiated by the mechanisms of hydrofracturing by surface water, and large ice-cliff failure (Pollard et al., 2015). If ice cliff height is approaching 90 m aerial elevation, the yield stress of the cliff may be surpassed. This leads to calving of the ice cliff, exposing a new ice cliff with larger aerial height, hence accelerated collapse (Pattyn, 2018). Apart from sub-shelf melt, surface melt and rainfall can drain into crevasses (fracture in ice shelf) that can further destabilize the ice cliff. A numerical model study by DeConto and Pollard (2016) included both MICI and MISI, and concluded that GMSL rise from the AIS may be more than a meter by 2100 under the highest 'Representative Concentration Pathways (RCP)', RCP8.5.

2.1.2. Future projections

Large discripancy have been found among studies projections future SLR. The differences arise mainly from different model assumptions used and non-trivial model choices such as the inclusion of deeply uncertain processes (Bakker et al., 2017). Updated projections of GMSL rise using the latest understanding and sensitivity of the AIS to climate change have reported systematically higher values compared to AR5 (right panel Figure 2.2). Apart from process-based studies, a way to include the deep uncertainties is to facilitate a structured expert elicitation among experts in the field as done by Bamber and Aspinall (2013) (henceforth BA13). They estimated future ice sheet melt to be 29-84 cm for the 50-95 percentile under RCP8.5 in 2100. Kopp et al. (2014) scaled the BA13 estimates to the 66% bandwidth of the AR5 dynamic mass loss estimates (thus keeping the tail). In contrast, Jackson and Jevrejeva (2016) replaced the AR5 dynamic loss by the BA13. More

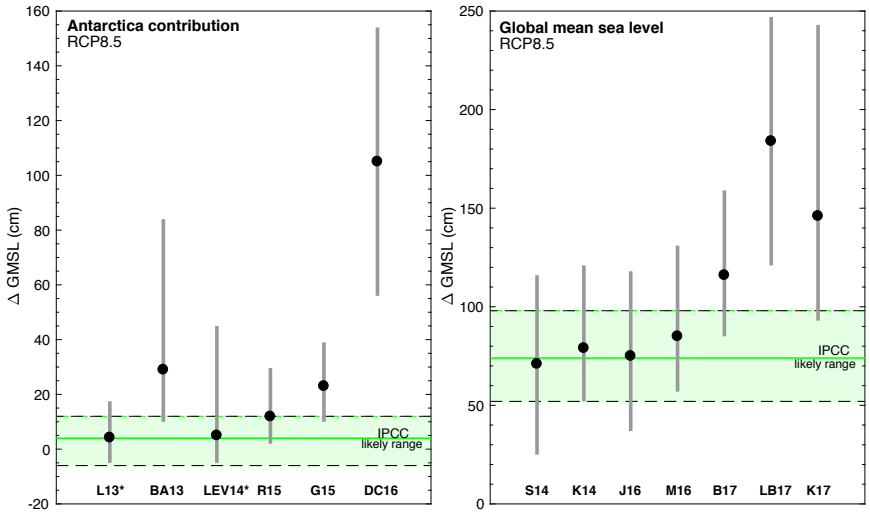

Figure 2.2: Overview of different sources of 2100 Antarctica contribution (median and 90%) together with the IPCC likely range. L13 (Little et al., 2013), BA13 (Bamber and Aspinall, 2013), LEV14 (Levermann et al., 2014), R15 (Ritz et al., 2015), G15 (Golledge et al., 2015), DC16 (DeConto and Pollard, 2016). Overview of 2100 GMSL sources. S14 (Slangen et al., 2014), K14 (Kopp et al., 2014), J16 (Jackson and Jevrejeva, 2016), M16 (Mengel et al., 2016), B17 (Bakker et al., 2017), LB17 (Le Bars et al., 2017), K17 (Kopp et al., 2017). *For L13 and LEV14, the SMB as reported in AR5 is added according to the percentiles to make them comparable.

recently, the results of DeConto and Pollard (2016) have been included into probabilistic projections of GMSL rise (Le Bars et al., 2017, Kopp et al., 2017). These studies have now reported end-century GMSL rise to be 79-184 cm (59-105 cm) with 95th-percentile values of 121-247 cm (93-158 cm) for RCP8.5 (RCP4.5) (Figure 2.2 K14, J16, LB17, K17), which is considerably higher than the reported 95% bandwidth of the IPCC (see green area denoted IPCC *likely range* in Figure 2.2).

2.1.3. Regional sea-level rise

Regional SLR (RSLR) may substantially deviate from the global mean (Slangen et al., 2014, Carson et al., 2016, Jevrejeva et al., 2016). These differences arise from several processes; (1) non-climatic geological processes, such as glacial isostatic adjustment (GIA), tectonic, mantle dynamics and sediment compaction (Kopp et al., 2015), (2) ocean dynamic changes associated with variations of wind-driven or buoyancy-driven ocean circulations (Hu and Bates, 2018), (3) gravitational effects from diminishing gravitational pull by the melting ice sheets and changes in land water storage (Mitrovica et al., 2011, Wada et al., 2012).

Due to melting of the ice sheets, the attraction of ocean water by the ice sheet diminishes. Close to the ice sheet, the sea-level changes relative to the Earth's surface drops whereas it will rise at larger distances (Slangen et al., 2012). Furthermore, the Earth is a rotating and visco-elastic body and changes in the local surface load affects the Earth's gravity field and rotation rate (Mitrovica et al., 2011). To scale global mass loss from land ice to RSLR, a regional scaling factor, or 'sea-level fingerprint', is introduced for all mass components. Recently, the existence of these sea level fingerprints could be detected using satellites (Hsu and Velicogna, 2017).

2.2. Shoreline response on engineering time scales

Beaches are complex systems that constantly adapt to short term morphological processes dominated by time-varying forcings such as waves, tides and currents (Hanson et al., 2003). On the long term, shoreline changes are driven by the interaction of processes that govern the sediment losses and gains. Time scales most relevant to engineers typically encompass everything from storm-induced changes (O(hours)) up to long-term changes associated with SLR (O(decades)) (Miller and Dean, 2004). Apart from storms and SLR, beaches exhibit cyclic

behaviour on inter-annual to decadal time scales. Interannual and decadal variability can be due to natural ('free') behaviour of the system or related to large-scale atmospheric dynamics (Stive et al., 2002, Robinet et al., 2016). Because of the complexity and large number of interacting processes, advanced numerical models are not yet suitable for long term coastal evolution modelling (Hanson et al., 2003). Instead, a number of practical approaches are proposed to bridge the chasm and provide coastal managers with long-term projections, ranging from heuristic formulas to physics-based statistical approaches.

2.2.1. Approaches: from storm events up to SLR

On time scales from hours to days, storms dominate the morphodynamic shoreline response. Episodic storms erode the beach and move sediments offshore, followed by longer periods of beach recovery (Stive et al., 2002). The magnitude of shoreline change is therefore a balance between storm response, storm frequency and post-storm recovery (Scott et al., 2016). Because of the complexity of processes during beach/dune erosion and overwash (overflow of water and sediment over a dune during a storm), simple predictive equations using only the cross-shore dimension have dominated past research and are still applied for large scale applications (e.g. Kriebel and Dean, 1993, Larson et al., 2004, van Rijn, 2009). More advanced models have been developed, such as the semi-empirical one-line model *SBEACH* (Larson and Kraus, 1989). Both the analytical models and *SBEACH* impose an equilibrium profile into their formulation. The underlying assumption here is that beaches tend to approach an equilibrium cross-shore profile under constant forcing. A well-known example of this is the equilibrium profile proposed by Dean (1977) that reads $h(y) = Ax^{2/3}$. The depth (h) here is a function of cross-shore distance (x) to the power two-third and a dimensional constant A. Adding more complexity to the calculations done by making use of a fully process-based model *XBEACH* (Roelvink et al., 2009). A common practises in coastal engineering to find the design storm erosion is to force a numerical model with a design wave height in order to determine the design storm erosion. However, storm erosion is governed by multiple hydrodynamic parameters, which all covary with each other (De Michele et al., 2007). This approach assumes that, for example, a 1:100 yr storm wave height results in a 1:100 yr storm erosion volume, which may not necessarily be the case (Callaghan et al., 2008).

In addition, conceptional equilibrium models have been developed that predicts shoreline response on time frames between individual storms and decadal-scale trends (Yates et al., 2009, Davidson et al., 2013, Splinter et al., 2014). On these time scales, the rapidly varying forcing caused by prevailing wave conditions is the main driver of cross-shore change of the shoreline. These models start from the same reasoning stating that a shoreline approaches an equilibrium state under steady-state forcing at an approximately exponential rate (Miller and Dean, 2004). Rather than using the cross-shore equilibrium profile, they link beaches response to the instantanious disequilibrium of beach state relative to the equilibrium beach state. The beach state is a concept introduced by Wright and Short (1984) who related the morphological state of a beach to the dimensional fall velocity, $\Omega = H_b/(w_s T)$. The morphological state links the characteristics of the sediment (fall velocity w_s) and the wave climate (via wave period T and breaking wave height H_b). Beaches tend to approach one of the two end states, either reflective ($\Omega < 1$) or dissipative $\Omega > 6$), via four intermediate states. This beach state is an important characteristic for the morphodynamic behaviour, with intermediate state beaches being most morphologically active (Aagaard et al., 2013). Moreover, beaches have a certain memory effect, making the behaviour dependent on the antecedent conditions. Both statements imply that the shoreline may react differently given similar hydrodynamic forcing. More specifically, this means that for the

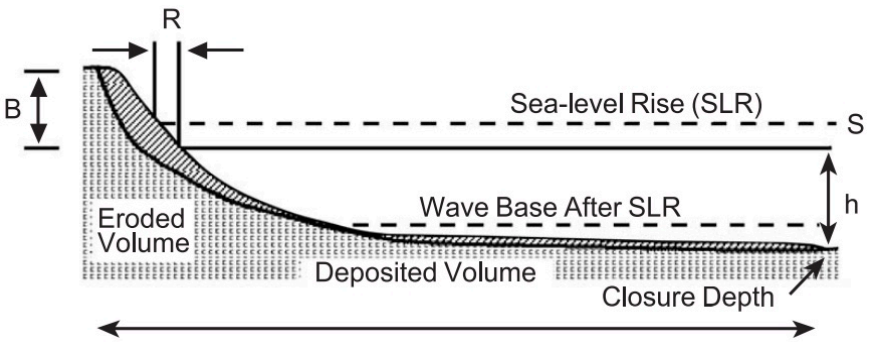

Figure 2.3: Schematisation of the Bruun rule. The recession of the cross-shore profile (R) from SLR (S) is a function of the active slope between berm (B) and closure depth (h). Obtained from Cooper and Pilkey (2004)

same offshore wave conditions, a beach may show an erosive behaviour if in a state of accretion, while it can accrete an already eroded beach (Yates et al., 2009).

To forecast shoreline recession (structural erosion) due to SLR, the Bruun rule (Bruun, 1962) has been widely used as a predictor (see Figure 2.3). Following SLR, the active profile will re-orientate landward and upward to maintain its (equilibrium) shape, thereby moving sediment particles from onshore to offshore. The active profile here is the distance between berm height and depth of closure, the latter being the depth beyond which littoral transport processes are not taking place. It has been widely scrutinized for its predictive skill (Cooper and Pilkey, 2004, Ranasinghe et al., 2012). Known difficulties are, for instance, selecting the depth of closure, which generally comes from a empirical formulation that vary by about 500% (Ranasinghe and Stive, 2009). Others have commented that the Bruun rule is an idealized case under the assumption of no other sediment sources and sinks, which is hardly found in nature (Stive, 2004). Despite the deficiencies, the Bruun rule and its extensions are still widely used in applied coastal engineering (Hinkel et al., 2013, Yates et al., 2011, Baron et al., 2015).

Studies focused on the including concomitant phenomena from storm erosion up to SLR are rare (Ranasinghe, 2016). For instance, a vector autoregressive model of shoreline position was used in combination with the Bruun rule by Toimil et al. (2017). Baron et al. (2015) combined projections of future wave climate with SLR projections, and fed this into a predictive storm erosion formula together with the Bruun rule. Ranasinghe et al. (2012) developed a probabilistic coastal recession model that uses a stochastic multi-variate sampling approach of storm parameters to model future storm events. They combined this with a predictive dune erosion model, while adding a trajectory of SLR over the years, in order to predict future coastal recession. This thus deviates from the Bruun rule by coupling the morphodynamics of storm erosion and longer term recession, which makes it physically more defendible. Callaghan et al. (2013) added extra complexity to the model by including a more sophisticated erosion model, although under large computational burden. Li et al. (2014) used a revised model to probabilistically assess dune erosion and recession for the Dutch coast. The added benefit of this approach over the Bruun rule is that is more physically defensible as it describes the combined morphodynamic processes of storm erosion and long term recession (Ranasinghe, 2016).

2.3. Coastal management and sea-level rise

2.3.1. Decision-making under uncertainty

Coastal managers are now assigned with the ever increasing difficult task of setting out policies under deep uncertainty associated with SLR projections. With deep uncertainty, one refers to situation when ”experts

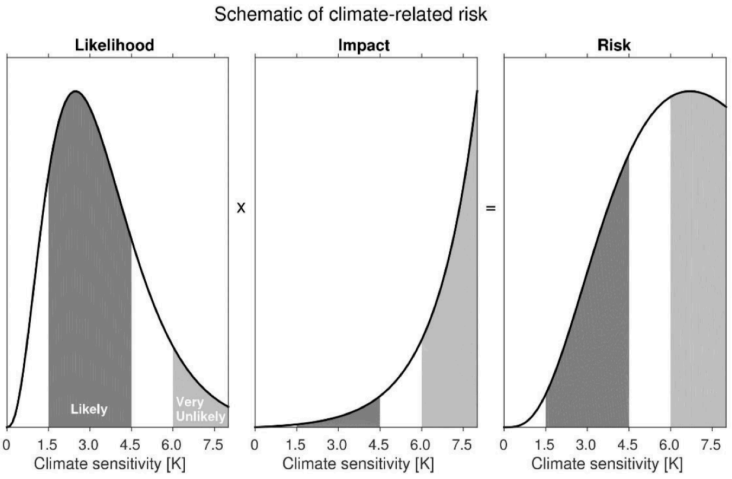

Figure 2.4: Risk management of low-probability (here named 'Very Unlikely') events and their impact that combined result in risk (likelihood x impact). The likely range is what is typically presented by the IPCC, whereas risk management is often about the tail of the risk distribution function (light grey part). Adopted from (Sutton, 2018, under review).

cannot agree upon or are not willing to provide probabilistic uncertainty ranges" (Lempert and Collins, 2007). Dealing with uncertainties in decision-making makes coastal management essentially a risk management issue (Oppenheimer and Alley, 2016). The low-probability but high-impact domain is often the key to risk management. Extremely costly outcomes with small but plausible probabilities may steer the mitigation alternatives and the perspective of the decision-maker (Kunreuther et al., 2013). This is illustrated by a hypothetical case for climate sensitivity in Figure 2.4, but this variable can in fact be replaced by any other climate variable such as SLR. The light grey part is here the low-probability part of the distribution function (likelihood), but if combined with a high-impact, has a high risk. This high risk part, or tail risk, is off interest for many decision-makers who want to eliminate this tail risk.

In general, coastal managers tend to be risk averse[1], which implies that they will not tolerate events with disproportionally large consequences and will prevent this from happening by investing more than the expected value of damage reduction. For this, a different risk appraisal method compared to the conventional cost-efficiency method may be preferred such minimax regret approach[2] As outlined by Hinkel et al. (2015), projections such as those provided by the IPCC are not designed for a risk-based coastal management approach. This is mainly attributed to the fact that the IPCC aims for scientific consensus without accounting for mechanisms that are poorly understood (Horton et al., 2014, Bakker et al., 2017). Because of their risk-averse attitude, coastal managers are not necessarily interested in estimates provided by the IPCC that they denote as a *likely range*. In terms of IPCC terminology, this means that it has a 66-100% probability range (and a 0-33% probability that it is actually outside this range). Instead, coastal managers demand information on the upper tail of the distribution. Therefore, probabilistic estimates of SLR including high-end scenarios or upper limits are more suitable sources of information for this purpose. Despite the significance of the high-end scenarios, they have been rarely applied into coastal impact studies.

Thus, confronted by this deep uncertainty, the preferred way to communicate SLR information depends on the decision-context. For instance, some argue that the current uncertainties faced cannot be captured into a single probabilistic density function (PDF) (Kunreuther et al., 2013). Hence, providing multiple plausible

[1] Risk-aversion is a term which originates from the classic decision theory. In general it means that a risk-averse person prefers certainty (e.g., receiving US$5) over uncertainty (e.g., 50% chance of receiving US$10, and 50% chance of receiving nothing). Example from Kind et al. (2017)

[2] Minimax regret approach aims at minimising the maximum possible costs that society might be faced with (Hof et al., 2010).

PDFs can help to provide insight into these uncertainties (Bakker et al., 2017).

2.3.2. Engineering approaches to sea-level rise

In general, adaptation to SLR can be loosely divided into three main strategies, following Klein et al. (2001):

- *Protect*: to reduce the risk of the event by decreasing its probability;
- *Retreat*: to reduce the risk of the event by limiting its potential effects;
- *Accommodate*: to increase society's ability to cope with the adverse effects of an event.

If talking about engineering measures, *Protect* often refers to traditional hard structural options (e.g dikes, levees, seawalls, dunes) or soft structural options (e.g. nourishments). For instance, the Netherlands proactively supplies sediments to the coastal zone in order to counterbalance coastal recession, with the 'Sand Engine' as iconic example (a 21.5 Mm^3 nourishment) (Stive et al., 2013). Measures falling in *Retreat* category include relocation of buildings and establishing setback lines. A setback line is a zoning policy that prohibits developing beyond a line set, which usually corresponds to an exceedance probability of the shoreline (e.g. 1/100 year). The distance of the setback line is a balance between risk and reward (Jongejan et al., 2011). Creating not enough buffer area will pose unacceptable risk to the community, while placing it too far inland implies greater (and valuable) land-use opportunities foregone. *Accommodate* measures include emergency planning, modification of land-use, and insurance.

The common approach to look at storm erosion under SLR, for instance, is to force a numerical model with design storm parameters (including SLR) and assess the impact. The shift towards evualuating SLR impact from a probabilistic perspective needs to be accompanied by an alternative approach to appraise different designs of the coastal measures. An approach based on a computationally intensive numerical model may not be satisfactory here, since a wide range of possibilities needs to be considered with slightly different parameter settings. Besides the necessity for handling stochastic input, deterministic coastal models convey a sense of absolute truth with little or no regard to endemic uncertainty (Cowell et al., 2006). Cowell et al. (2006) argues that this requires a shift in the coastal management culture to accept decision-making based on risk-management protocols. The development of probabilistic methods have recently gained momentum over the years, and risk-informed coastal decision-making is now adopted by some coastal managers (Ranasinghe, 2016).

2.3.3. A holistic view

To overcome the barriers highlighted and avoid maladaptation[3], a holistic view between the climate science community (sea-level information providers), coastal service provides (e.g. coastal engineers who are the users of the projections) and decision-makers is needed.

For the remaining, the focus in on probabilistic estimates of coastal erosion, both storm erosion and coastal recession. The rationale for looking at the implications of decision-making is thus derived from the concepts and viewpoints that are introduced above.

[3] Maladaptation refers to the adaptation of a system to a poorly understood problem. Short-term adaptation may results in an undesirable and unintended outcome on the long term, in the end reduce the overall vulnerability of the system (Magnan et al., 2016).

3 Case study: Sint Maarten

A case study is introduced for the island of Sint Maarten. For readability, only an introduction to the case study is provided here. The impact of SLR is discussed for this case study, albeit SLR projections are made for the whole Caribbean basin. For those interested into a more regional overview of recent work on climate change impact, past observations of SLR and an introduction to future SLR projections, a reference is made to appendix A.

3.1. Case study: Sint Maarten/ Saint Martin

Sint Maarten is a volcanic island located in the North Eastern Caribbean (Northern Lesser Antilles) (18.01°N, 63.03°W). The total island area (96 km^2) is divided into a Dutch part (37 km^2) and French part (Saint-Martin: 59 km^2). The island is inhabited by almost 80.000 people (2017) and its economy is primarily driven by the tourist industry with over 2 million tourists visiting the Dutch part of the island in 2017 (Department of Statistics, 2017). The island is part of the Small Island Developing States (SIDS), with recent Hurricane Irma (September 2017) painfully exposing the vulnerability of the island.

Past SLR in the Caribbean was slightly less than the global average, with a trend of 1.7 mm yr^{-1} found over the period 1993-2009 (Palanisamy et al., 2012, Torres and Tsimplis, 2013). Future SLR in the region may very well be above globally averaged SLR, in particular due to its location in the tropics that makes its sensitivity to mass loss from the both ice sheets. For instance, regional SLR projections for two tidal gauge stations are included in the most recent NOAA-projection (Sweet et al., 2017). From this, it can be observed that under an intermediate scenario of 1.0 m GMSL-rise, SLR will increase regionally by approximately 0.1 m on top of this for 2100. Under an extreme scenario of 2.5 m, this additional regional effect is in the order of 0.7 m for the same year.

In terms of hydrodynamics, the Sint Maarten has a mixed primarily diurnal tide (one high and low tide each day). The tidal range is microtidal with tidal ranges rarely exceeding 20 cm in height (Kjerfve, 1981). Analysis of wave hindcasting data (Dee et al., 2011) shows that wave climate exhibits a seasonality over the year with mean significant wave height (H_s) between 1.5 and 2.0 m, albeit larger values during the Northern Hemisphere winter. Throughout the year, mixed locally generated waves (wind-waves) and remotely generated waves (swell) approach the island predominantly from the open ocean side in the east/north-east. Seasonality in the wave climate is caused by different meteorological events. The island is located in the Atlantic Hurricane Belt with the North Atlantic hurricane season running from June to November. Hurricanes are being the strongest in the months of September and October (Misra et al., 2018) raising the water level along the coast (storm surge). Moreover, when intense mid-latitude storms pass over the warm currents such as the Gulf Stream during the

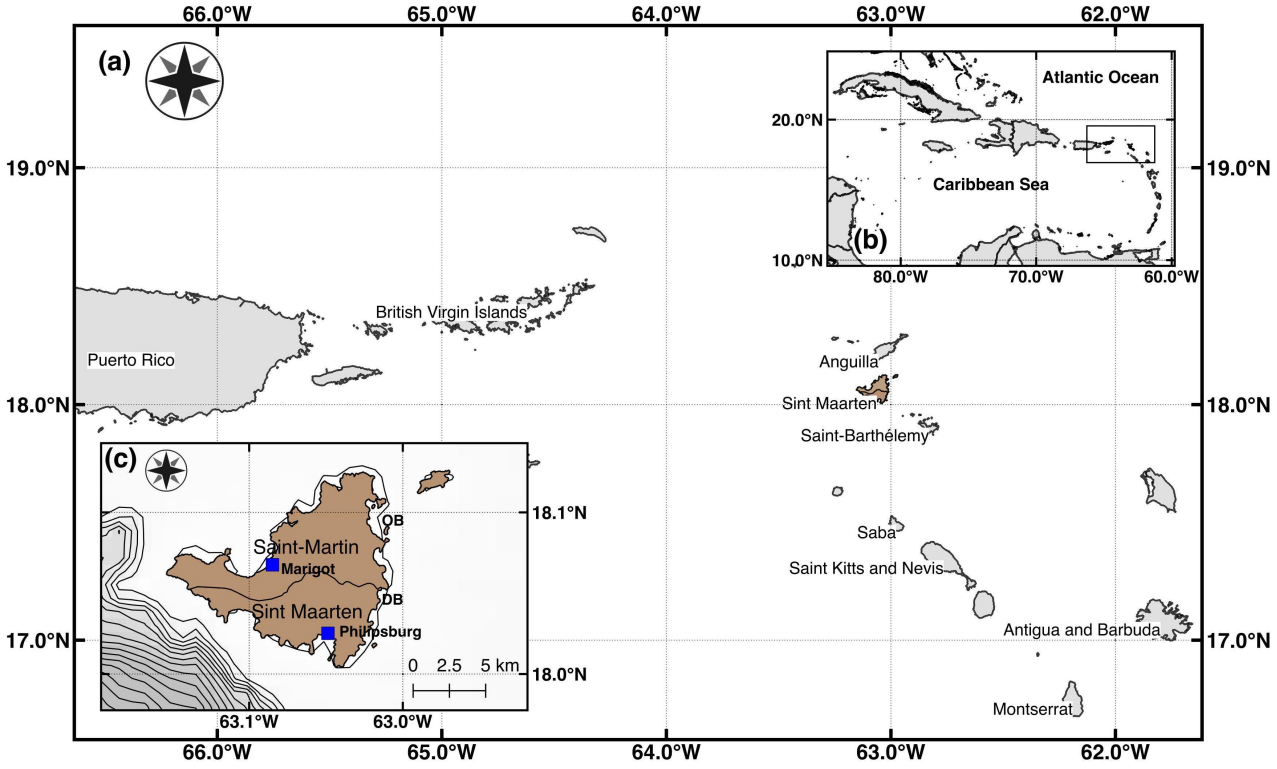

Figure 3.1: (a) Overview of the Northern Lesser Antilles with the island of Sint Maarten in brown. (b) The Caribbean Sea and island with the close up indicated by the black box. (c) The island of Sint Maarten/Saint Martin with the two beaches considered in the analysis, namely Dawn Beach (DB) and Orient Bay (OB). Depth contours have an interval of 50 m and are based on GEBCO. All administrative boundaries are from the 'Global Administrative Areas' database (GADM).

winter months, big storm waves are generated. These storm waves approach the Caribbean from the north and east as swell waves ($T > 8s$) (Jury, 2018).

The geomorphology of the coastline is primarily composed of cliffs and hills with numerous embayed and pocket beaches in between the rocky heads. The Anguilla Bank surrounding the island can be characterized by a narrow shelf in the south with the 100 m depth contour at 2 km offshore and a more wider, shallower, part on the east with the 30m depth contour at approximately 5 km.

Two beaches are considered for further analysis, namely Dawn Beach and Orient Bay. Dawn Beach (DB) and Orient Bay (OB) are enbayed areas, both facing the open ocean in the east thereby prone to most storm waves (see Figure 3.1c). In general, pocket or embayed areas are often constrained in their longshore sediment transport due to their limited directional window of incoming wave energy (e.g. Bowman et al., 2009). Hence, it can be expected that cross-shore changes induced by storm waves are the dominant causes of morphological change. The beaches are both steep, reflective, beaches without a complex dune structure. The beaches further have uniform morphology and lack offshore bars (Boon and Green, 1988). Wave shoal from deep water to the shoreline and often have a narrow surfzone, thus wave breaking close to the shore (Aagaard et al., 2013). Beaches prone to winter swells from the North Atlantic show an erosive tendency during the winter months and an accreting behaviour during the summer months when they experience lower wave energy (Cambers, 2005). Beach sediments have typical grain size diameter (D_{50}) of 0.22 - 0.85 mm (Boon and Green, 1988, Kohsiek et al., 1987).

4 Materials and method

In order to assess the impact of uncertainty in the contribution of AIS to SLR on future storm erosion and recession, a probabilistic framework is constructed that incorporates regional probabilistic SLR projections into a stochastic storm erosion model. This model is then applied to the two beaches on the island for two RCP-scenarios (RCP4.5 and RCP8.5). Moreover, the sensitivity of RSLR to additional model uncertainty in future CMIP5 estimates is assessed. In total, 12 cases are considered for both beaches. This additional model uncertainty is to showcase that arbitrary decisions made by the providers of SLR projections can influence the results in the end and therefore needs careful consideration.

The different building blocks are shown in the flow chart in Figure 4.1. First, RSLR projections are made for the area (I) (4.1). Then, multi-variate storm time-series have to be derived, which serves as a input for the stochastic model (II) (4.2.3). This is accompanied by setting a definition for a storm event that initiates morphological change at the beach (4.2.2). The multi-variate storm time series are then fit to a copula to constrain their dependency (III) (4.2.3). From this copula, future storms can be sampled, and SLR-trajectories are also sampled and added to the storm surges (4.2.4). This is fed into a storm erosion formula (IV) (4.2.5). Using the storm frequency, inter-arrival time and beach recovery, a future shoreline position can be sampled (4.2.6). At last, the results are analysed by means of extreme value statistics (V).

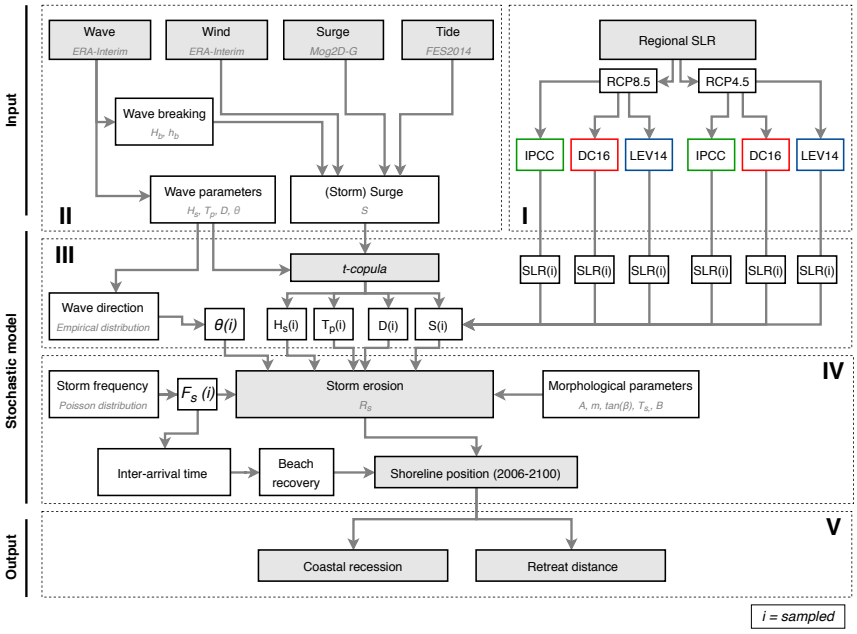

Figure 4.1: Flow diagram of the probabilistic coastal erosion model divided in the five building blocks. (I) Generating regional sea level rise projections for three cases of Antarctic dynamic mass loss, (II) Creating time series of storm parameters, (III) Fitting past storm time series to a copula that is used for sampling future storm time series, while adding SLR to it, (IV) Transform storm parameters into erosion values and shoreline position using the predictive formula and storm frequency, and storm recovery between storms, and (V) generating the output and doing extreme value statistics.

4.1. Sea-level rise projections

Starting point is the method of GMSL rise as presented in AR5 of the IPCC (Church et al., 2013) and extended by de Vries et al. (2014) and Le Bars et al. (2017). Mathematical details are captured in Appendix 4.2.

A rise in GMSL can be attributed to changes in mass loss from the Greenland ice sheet (GIS), AIS, glaciers and small ice caps (GIC) and land water (LW), and due to thermal expansion and salinity changes of the ocean (ocean steric). Both ice sheets are further subdivided into a component that represents dynamic mass loss (dynamic processes at the ice-ocean boundary) and surface mass balance (SMB) (changes in the mass balance, due to accumulation and ablation). Regionally, two other effects should be included; the local ocean dynamic changes due to changes in ocean circulation patterns and an inverse barometer effect (IB) effect due to atmospheric pressure loading.

These contributors are derived from mainly process-based models and transformed into mathematical relations, such that they can be incorporated in a probabilistic framework. In Church et al. (2013), all components, except GIS dynamics, LW and AIS dynamics, are dependent on global mean surface temperature (GMST) that thus acts as a steering variable. The advantage of using the modelling framework of Church et al. (2013) is that is preserves the dependency structure between contributors (via GMST), which is an important consideration when looking at the low-probability part of the distribution function (Le Bars, 2018, in review). The framework is presented in Figure 4.2, with all arrows starting at GMST indicating that it is dependent on that contribution.

4.1.1. GMST

Temperature anomalies are taken from the 'Coupled Model Intercomparison Project Phase 5' (CMIP5) models. Given imprecise knowledge on the shape of the distribution function, GMST is assumed to follow a normal distribution around its ensemble mean. All model estimates for all years are combined in a matrix $\mathbf{T}$. For every year, the mean $\overline{T}$ and standard deviation $\sigma(T)$ are calculated. Then, N_1 is a vector sampled from a standard normal distribution ($N_1 \sim \mathcal{N}(0,1)$) and a normal distribution is constructed for every subsequent year by:

$$T(t) = \overline{\mathbf{T}}(t) + \gamma\sigma(\mathbf{T}(t,.))N_1. \tag{4.1}$$

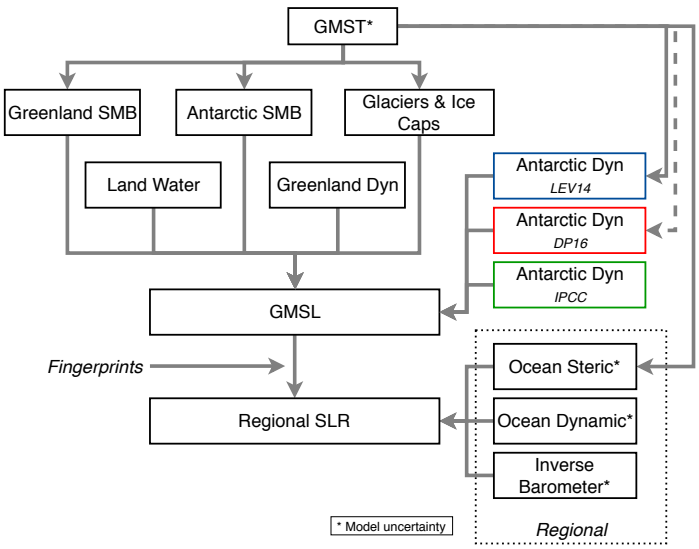

Figure 4.2: Overview of probabilistic SLR projections. Arrows indicate interdependencies. The contribution from cryosphere components and land water contribution are first derived for GMSL. Indicated by the arrows, most of them (except Land Water and Greenland DYN) are dependent on GMST. They are then scaled to RSLR using the fingerprint values and using Sint Maarten as area. The contribution from ocean steric, ocean dynamic and inverse barometer are taken regionally from CMIP5 models. Three cases of AIS dynamics are considered; as considered in the IPCC, which is independent of GMST (green, Church et al. (2013)), based on Levermann et al. (2014), which is dependent on GMST, and based on DeConto and Pollard (2016). The dashed line in the latter means that it can be made dependent on GMST as done by Le Bars et al. (2017). The * indicates that it is from CMIP5 models and thus changes when model uncertainty is added.

Following Church et al. (2013), the reference period is set to 1986-2005, and reference temperature distribution will be denoted by $\widetilde{T}_{1986-2005}$. In short:

$$\widetilde{T}_{1986-2005} = T(t) - \overline{T}_{1986-2005} \tag{4.2}$$

The γ in equation 4.1 is introduced to add an extra temperature uncertainty (standard is 1.0), as shown in (3).

4.1.2. Modifications compared to AR5

The contributions from the GIC, GIS, LW and Antarctic SMB are taken similar to Church et al. (2013). Three modifications are made, namely (1) substitution of the AIS dynamics with two other estimates, (2) regional correlation between the ocean steric component and GMST, and (3) including additional model uncertainty in the projections.

(1) Antarctic dynamics In AR5 of the IPCC, the AIS dynamics contribution is included by means of a uniform, scenario-independent, distribution function with median of 7 cm, with -1 cm to 16 cm as likely range (green line in Figure 4.3). These projections are based on the work of Little et al. (2013), who extrapolated observed growth rate of discharge in part of West Antarctica. They further quantified the uncertainty about future discharge from other drainage basins on the AIS.

For the second scenario, we replace the AIS dynamics with the projections provided in Levermann et al. (2014). In this work, an intercomparison of five numerical ice sheet models of Antarctica was performed. A probabilistic framework was constructed using so-called linear response theory to project ice discharge for varying basal melt (melt underneath the ice shelves due to an influx of warm ocean water) scenarios. A linear response curve between ice discharge and local subsurface ocean warming (factor of GMST) is assumed. The use of linear response theory implies that self-amplifying effects such as MICI and MISI are assumed not important. The probabilistic method has the advantage of having GMST as a driving force, which fits well in the overall SLR framework because it preserves the dependency with other components. For this research, only the combined results of three models that explicitly include the ice shelves are used, since the other two are overestimating the melt along the coastline (Levermann et al., 2014). The result for both RCPs is a skewed distribution function with the mode (most probable value) close to the median value of Church et al. (2013), but with increased probability of larger mass loss (blue line Figure 4.3).

The third scenario includes incorporating the numerical model results of DeConto and Pollard (2016), which are hitherto the highest reported projections of AIS contribution to GMSL from a numerical model. Their numerical model has apart from MISI feedback athe first parametrisation of hydrofracturing due to surface melting and ice-cliff structural failure, leading to the MICI feedback (Pollard et al., 2015). Moreover, DeConto and Pollard (2016) provided results for different paleo-climate calibration estimates of sea-level during the Last Interglacial (LIG) and Pliocene. To investigate the highest possible outcome, values from their model results for LIG 3.6-7.4 m, Pliocene 10-20 m are taken. The given median and standard deviation as reported are 58 and 26 cm for RCP4.5 and 114 and 36 cm for RCP8.5, respectively. In addition, the numerical model already takes the contribution from Antarctic SMB into account, so this is not added. These projections can be made temperature dependent as is done in Le Bars et al. (2017), which done when adding the additional model uncertainty to the projections (see (3)).

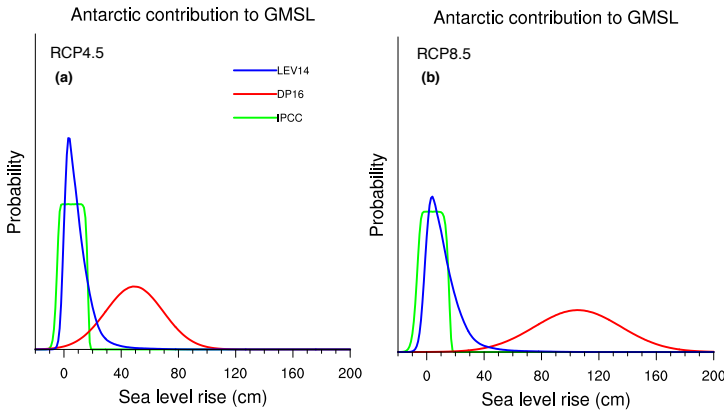

Figure 4.3: Contribution of mass loss from the AIS (dynamics and surface mass balance) to GMSL for the three cases considered. (a) for RCP4.5 and (b) for RCP8.5. PDFs are for 2100 compared to the 1986-2005 average.

(2) Correlation steric contribution and GMST The ocean steric component is taken from the latest ensemble of global climate models; Coupled Model Intercomparison Project Phase 5 (CMIP5) (Taylor et al., 2012). In AR5, the steric contribution to GMSL rise is assumed to be perfectly correlated with GMST ($\rho = 1.0$). However, for Sint Maarten, a correlation coefficient of 0.4 is found from the CMIP5 models. The low correlation of the local steric component can be well explained by the fact that steric effects are not only forced by GMST, but also depend on dynamical processes that are model dependent (Le Bars, 2018). Li et al. (2016) showed for instance that future local steric rise is composed of a strong thermosteric rise partly balanced by a moderate halosteric drop.

(3) Additional climate model uncertainty GMST, ocean steric, ocean dynamics and inverse barometer contributors are taken from the CMIP5 models (see * in Figure 4.2). Climate models, however, have common biases such as parametrisation of sub-grid physics and representation of the Atlantic meridional overturning circulation (AMOC) (Wang et al., 2014, Maraun et al., 2017). Therefore, the multi-model mean does not accurately represent the entire range of likely futures (Annan and Hargreaves, 2010). The IPCC has chosen to assign the 5-95 percentile range of climate model results a *likely range*. In IPCC typology, this means that it has a likelihood between 66 and 100% (instead of 90%). To account for this, a case is explored without additional model uncertainty, thus similar to Church et al. (2013) (hereafter referred to as $\gamma = 1.0$), and a case with additional model uncertainty (hereafter referred to as $\gamma = 1.64$). Kopp et al. (2014) and Le Bars et al. (2017) have included this temperature uncertainty previously. Assuming a normal distribution, the factor 1.64 is multiplied with the multi-model standard deviation in Equation 4.1 to rescale the uncertainty range from 66% to 90%. This thus widens the distribution function, and because other components are dependent on GMST, will also widens the range of these components.

Fingerprints To transform mass loss from global to regional estimates, globally averaged values are multiplied with their representative fingerprint, which are taken from Slangen et al. (2012, 2014). The regional fingerprints are presented in Figure 4.4. The Antarctica fingerprints have a uniform pattern over the basin, with an above global average value of 115-130% for both SMB and DYN (4.4c&f). The contribution from Greenland shows a north-south gradient (85-100%) over the area reaching globally averages values near Columbia and Panama (4.4b&e). The fingerprint of the GIS and AIS are independent of time. Glaciers and land water are time dependent and show little spatial differences, and nor to limited temporal variation. The LW fingerprint

remains unchanged over the years with values of 99-104% over the region (4.4a). GIC fingerprint values are 92-98% in 2006 reaching 98% in 2100 (4.4d).

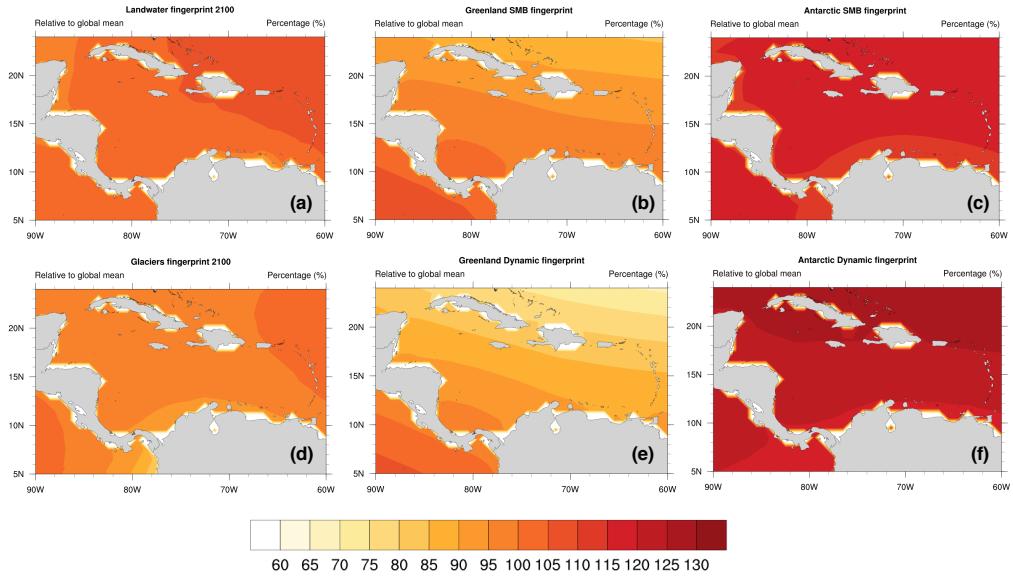

Figure 4.4: Regional fingerprints of the individual components for the Caribbean Sea. Values in percentages from the global average (100% indicates global average). (a) Land Water, (b) Greenland SMB, (c) Antarctic SMB, (d) Glaciers and small Ice Caps, (e) Greenland dynamics, (f) Antarctic dynamics. Based on Slangen et al. (2012).

4.1.3. Regional sea-level rise

In the end, all mass contributions are multiplied by their fingerpints and combined with the ocean steric and dynamics, and the IB component. RSLR is the constructed by sampling all components using a Monte Carlo sampling. A total of n = $5x10^5$ samples is used to construct the final PDFs of RSLR. Hereafter, the cases are referred to as IPCC, LEV14 and DP16 in line with their Antarctic dynamics distribution function. For context, in 2100 the steric sea-level rise and GIC are the dominant sources of RSLR under the IPCC case, while AIS and GIS follow thereafter. For LEV14, the PDF of RSLR will become skewed following the PDF of LEV14. Under DP16, AIS becomes by far the largest contribution to RSLR.

4.2. Probabilistic coastal erosion model

Projections of RSLR will added to the coastal erosion framework in box (III). First, the stochastic model needs to be set up. Realistic time series of storm can be synthetically realized by making use of the statistical characteristics of observed storm events. To simulate the SSTS using the stochastic model, the following procedure is followed: (1) data retrieval and storm definition, (2) fit marginal distribution functions to storm characteristics, (3) fit dependency structure between storm characteristics, and (4) simulate synthetic storm time series while adding sampled sea level rise trajectories.

4.2.1. Data retrieval

Storm parameters are here defined as a combination of wave and wind climate data (including significant wave height H_s, wave period T, wave direction θ; wind speed u_{10}) and storm surge S. Time series of storm parameters are derived for a 25 year period (1993-2017) with 6h temporal resolution. Mathematical details for

selected parts can be found in Appendix C.

H_s, T, θ and u_{10} are taken from the ERA-Interim reanalysis product (Dee et al., 2011). The product has been calibrated by others in the region (Appendini et al., 2014, Devis-Morales et al., 2017, Jury, 2018), and despite some discrepancies with the extremes, performs well. Data is extracted from an offshore location [18.125°N, 62.875°W] (OB) and [18.0°N, 62.875°W] (DB), where water depth is considered deep enough to assume linear (Airy) wave theory. Wave climate data outside the range of incident angles are truncated; only waves with directions 0-180°(DB) and 0-140°(OB) are considered. Wave period is transformed to peak wave period T_p by multiplying it by 1.1 under the assumption of a narrow spectrum. Furthermore, a time series of S (total water level (TWL) - mean water level (MWL)) is constructed. This is done by adding up the astronomical tide η_a (FES2014, Carrere et al., 2015), atmospheric wind and pressure set-up η_{sur} (Mog2D-G, Carrère and Lyard, 2003), extra wind set-up η_{wis} (balance shear stress and set-up) and a water level set-up due to wave energy dissipation η_{was} (Dean and Dalrymple, 2001). η_{was} needs information on breaking wave height H_b and depth h_b. To directly translate offshore wave conditions to breaking wave height, the predictive formula of Larson et al. (2010) is applied. This formula essentially governs the wave energy flux conservation combined with Snell's law, but in a predictive manner.

4.2.2. Storm definition

Storms are extracted from the 25 year time series that are created.

A storm is defined often as a water level elevation or offshore wave height criteria that, if surpassed, will result in morphological change at the beach. However, setting this threshold is somewhat arbitrary and region-specific; Callaghan et al. (2008) uses a offshore wave height of above 3.0 m for Australia, Li et al. (2014) uses 3.0 m plus a tidal anomaly of 0.5 m for the Netherlands, while Wahl et al. (2016) asserts a total water level anomaly of 1.2 m for the Gulf of Mexico. For Sint Maarten, wave set-up dominates the total water level (never less than 75-80%), and it is therefore hypothesized that offshore wave height can be used as a proxy for changes at the shoreline. Still, finding the threshold that initiates morphological change is difficult given that beach do not have a pronounced backdune and no storm erosion data is available. To bridge this gap, satellite derived shoreline (SDS) measurements from mid-2012 to early 2017 were obtained from Luijendijk et al. (2018). SDS are derived from satellite images that detect the shoreline using a shoreline detection algorithm. For the Sint Maarten beaches, recurrence interval of satellite measurements (images) are between 1 and 16 days for this period. From this, moments of shoreline erosion and accretion can be identified. An iterative approach is adopted by setting the wave height threshold, identify storms and compare the times that storms are identified with the moments that the shoreline position is eroding. For both beaches, a threshold is set to 1.9 m that explains most moments that the shoreline is eroding (or already in a state of erosion). This is indicated by the grey line in Figure 4.5 together with the corresponding values of H_s and S. Peaks of H_s and S largely coincide illustrating the dominance of H_s in creating peak surges. There is an existing seasonality in H_s (hence S) and the shoreline position, with higher winter waves (swell) eroding the shoreline alternated by general accretion during the summer waves (wind-waves). What could also be observed is the state dependent behaviour during the winter period. At the start of the season, a given wave height will erode the beach quickly, while under that same wave height at the end of the season, the beach accretes (see for instance the moments at the start and end of 2015/2016 winter season). Overall, wave height seems a good indicator of beach change and will henceforth be used.

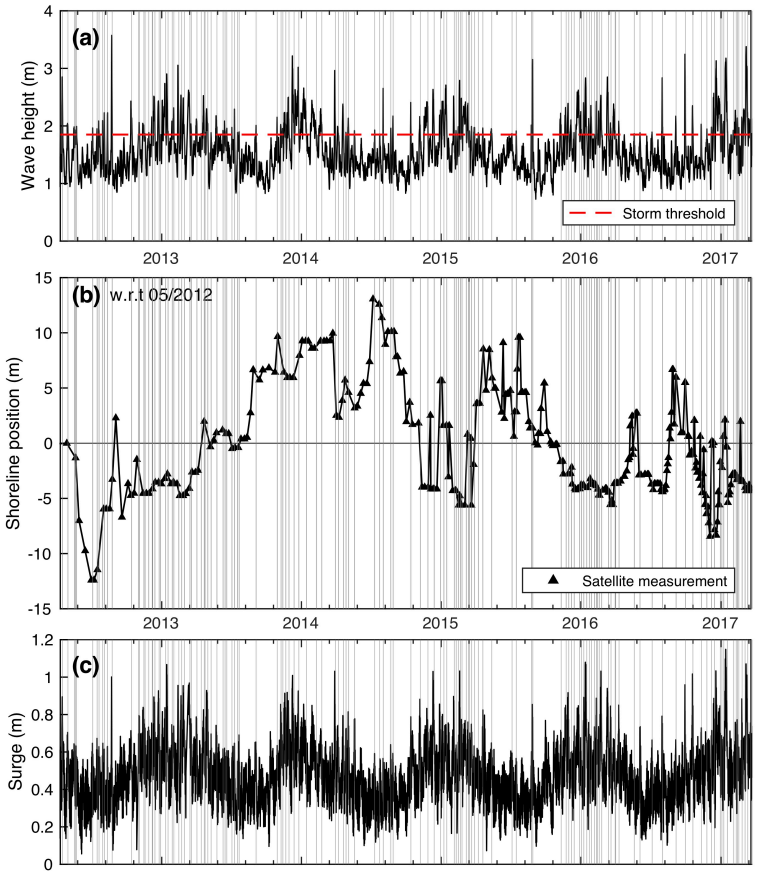

Figure 4.5: (a) Time series of offshore wave height (H_s). The red dashed line indicates the threshold of 1.9 m set to define a storm event. (b) Satellite derived shoreline (SDS) positions of Orient Bay with linear interpolation between SDS measurements (triangles). The shoreline position is relative to the position on March, 2012. (c) Time series of surge (S). The grey line in (a-c) indicate the onset of the storm events as identified by the threshold. Peaks in H_s largely coincide with peaks in S illustrating that wave set-up is the dominant source of peak water levels.

Storm events are then found by searching for H_s exceedances above the threshold while selecting the concordant T_p and θ of the peak wave height. To assure extracting independent storm events, a 24h time interval time is set that has to be exceeded before a new storm is counted, following Li et al. (2014). The storm duration (D) is the duration above the threshold. A small term is added by linear interpolating the first observation before and after passing the threshold (both begin and end storm). This step is essential to avoid working with discrete values for storm duration (steps of 6h). Otherwise, the ranks cannot be uniquely defined (Salvadori et al., 2014), which leads to problems with the copula in the next step (because copula works on unit scale). The S and H_s of a storm event is found by finding the maximum value over the storm duration.

Because of the seasonal cycle identified, storm are first split into summer storms (April-September) and winter storms (November-March). For the remaining, stationary storm conditions are assumed for the SSTS. A linear regression analysis (see appendix C.4) of the storm parameters suggest that the seasonal cycle is slightly amplified (positive trend in winter, negative trend in summer). However, climate models predict nor to limited change (small decline) in wave and surge conditions for the future (Hemer et al., 2013, Vousdoukas et al., 2018). Therefore it is decided not to extrapolate this trend.

We now have a database of storms with characteristics H_s, T_p, θ, D and S that serves as a input for the stochastic model.

4.2.3. Modelling marginal storm variables and dependency structure

It can be expected that the storm parameters covary with each other. To model interdependencies between storm parameters, a copula-based approach is suggested. Copulas are becoming increasingly popular in the

field of hydrology and coastal engineering for creating multi-variate extreme events (De Michele et al., 2007, Vandenberghe et al., 2010, Davies et al., 2017). Copulas are very flexible, as they are independent of the underlying marginal distribution functions of the variables, and useful when tail dependency is known to be present (de Waal and van Gelder, 2005). Because of the independence on the marginal distribution function, different marginal distribution functions of the underlying univariate variables can be combined. This implies that there is no restriction on choosing between different marginal distribution functions.

Marginal distribution functions are fitted to the parameters H_s, T_p, S and D for both seasons. The use of marginal distribution function is to allow drawing samples beyond the observed range of values. The decision which distribution to use is based on minimizing the Root Mean Square Error and by considering a distribution that best fits the tails. For H_s and D, a generalized Pareto distribution is found to be the best fit, whereas T_p and S are best represented using a generalized extreme value distribution. All fitted distribution functions pass the Chi-square goodness of fit test. Wave angle θ is fitted to its empirical distribution function. An empirical distribution function is used to only consider waves angles within the range of incident angles (see for range). The marginal distribution functions are shown in the boxes in Figure 4.6 in blue (winter) and red (summer). From here, it can be shown that summer storms have narrower approach angles (predominantly from 90 degrees) , shorter duration, lower median S but higher extremes, and have waves that are shorter in length (small period) compared to winter storms.

A cross-correlation analysis shows how parameters $H_s - S$ and $H_s - D$ have a strong correlation (ρ = 0.75-0.82), whereas $H_s - T_p$ has a weaker correlation (ρ = 0.10-0.33), as shown in coloured correlation coefficients in Figure 4.6 (blue: winter, red: summer). A separate copula is considered for the summer months and winter storms, because storm characteristics may stem from a different dependency structure. First, tail dependency between variables is checked by transforming the data back to standard normal scale (Joe, 2014). Their overall rank correlation (Spearman ρ_r) is compared to the correlation of the four quadrants, with higher semi-correlation being a indicator for tail dependency (Morales-Nápoles et al., 2017). For H-T, no tail dependency is found, whereas for H-D and H-S have a small lower and upper tail dependency. Moreover, a preferred

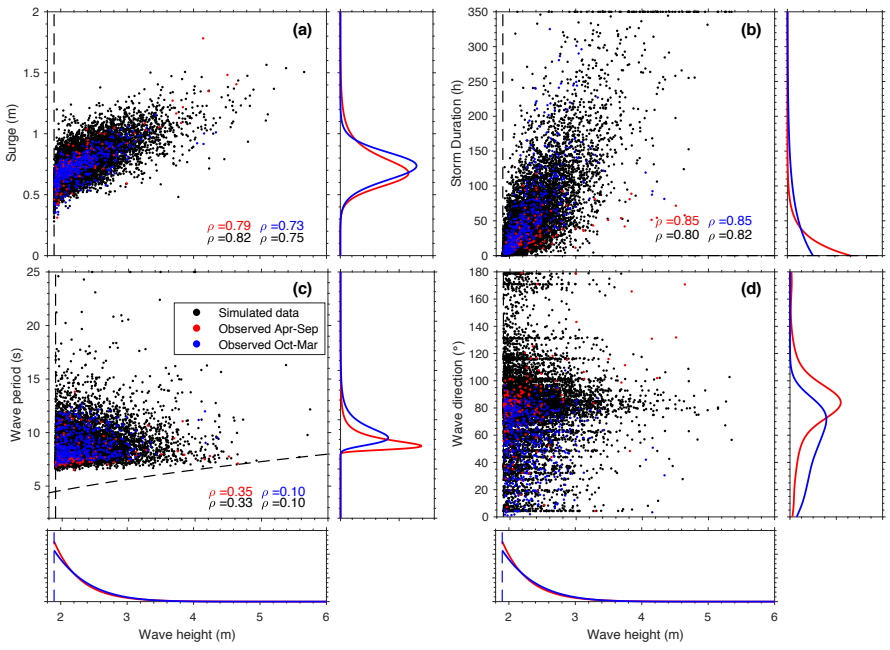

Figure 4.6: (a) Scatterplot of observed variables wave height and surge for both winter months (Oct-Mar, blue) and summer months (Apr-Sep, red). The black dots show a 10,000 random sample using the fitted t-copulas. In the boxes, the univariate PDFs. Spearman rank correlation of the seasonal observations (red and blue) are compared to those obtained from the sampled copula (black). (b) same as (a) but for wave height/storm duration. (c) same as (a) but for wave height/wave period. Black dashed line indicate the steepness limit set ($s = 0.06$). (d) Same as (a) but for wave height and wave direction. Instead of copula, sampled independently from the empirical cumulative distribution function of both (no correlation compared).

copula is chosen by performing a goodness-of-fit test based on *Cramèr-von Mises* $\mathcal{M}$ statistic between the empirical and parametric copula (Genest et al., 2009). After comparing both elliptical copulas (Gaussian and *t*) and Archimedean copulas (Frank, Gumbel, Clayton), it was decided to take the *t*-copula. This copula performs well and has the advantage of being elliptical, such that it can be extended to multiple dimensions easily, while for bivariate Archimedean copulas this is much more complicated and needs a sampling method such as Gibbs-sampling (Li et al., 2014). More details on copulas is provided in Appendix C.

Using this, a four-dimensional random sample can be generated and transformed back the original scale using the inverse of the marginal distribution functions defined. This is shown in Figure 4.6 for Dawn Beach, where 10,000 samples are generated (black) and visually compared to the observations (blue is copula winter, red is copula summer). Moreover, the rank correlation (ρ_r) of the observations is compared with the correlations presented by the copula (grey), which gives an overall good result. The wave direction is assumed to be independent of wave height and independently sampled from its empirical cumulative distribution function (ECDF).

To constrain the samples within a physically realistic extent, a few boundaries are set. First of all, observations show a maximum steepness of $s = 0.06$ between wave length (thus wave period) and wave height and larger steepnesses are not allowed (black line 4.6c). A maximum duration of D = 350 h is used in line with observations. Finally, just as Wahl et al. (2016), a maximum wave period is fixed at 25 s, to avoid sampling waves that are being classified as infragravity waves (Munk, 1949).

Before future storm time series can be generated, the storm frequency (F_S) must be determined. Over the 25 year period, 467 storms were identified in winter and 207 storms in summer, with yearly variability. To account for this, the number of storms should be treated in the same in the same stochastic manner. For every year in the record, the monthly number of storm occurrences was calculated. A Poisson distribution is fitted to the monthly data with parameter λ_P representing the average rate of occurrence. From this, a monthly sample can be taken to generate a yearly number of storms. The yearly number of storms is again Poisson distributed with $\lambda_{P\sum}$ simply being the sum of the monthly parameters. Within a month, storms are randomly assigned a time position while assuring that the 24h minimal inter-arrival time between storms is maintained.

4.2.4. Synthetic storm time series and SLR

Using the four dimensions copula, the ECDF of θ and the Poisson distribution of F_S, many long time series of future storm events can be sampled. Because SLR projections are made for the period 2006-2100, and since storms are assumed stationary, SSTS are also made for this time period and thus have a 95 year time span.

Now, SLR projections can be added to the SSTS. SLR will gradually increase over the years and adds up to the S that is sampled by the copula. For every SLR case, a random sample is drawn between 0 and 1, and a SLR-trajectory is constructed using the ECDF of SLR. For instance, assume 0.5 is drawn. Then for every year, the 50th percentile value of the ECDF is taken, leading to a 50th percentile SLR trajectory, and added to the S values sampled during that year. In this way, extreme values of S will increase in frequency over the years.

Subsequently, the SSTS enhanced by the SLR trajectory can be fed into an erosion model for the purpose of estimating retreat distances and long term recession.

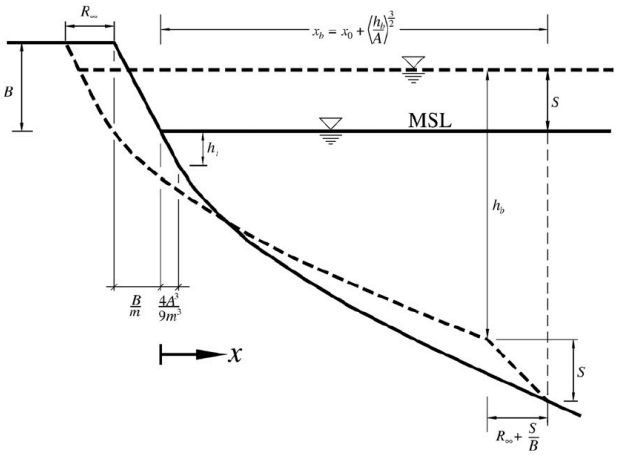

Figure 4.7: Storm erosion model according to Kriebel and Dean (1993). The retreat (R) as a results of increase in water level (S) is derived based on a sediment balance between the eroded sediment and deposited sediment offshore in between the berm height (B) and surf-zone width (x_b). The surf zone width is based on the equilibrium profile (Dean (1987)) given by parameters (A) and (m).

4.2.5. Storm erosion

Coastal morphological response to storm events and SLR is expressed by two parameters, the episodic shoreline retreat distance (R) and the long-term coastal recession (CR). To model episodic storm erosion, an analytical function described by Kriebel and Dean (1993) (hereinafter referred to as KD93) is used, which has been successfully applied in different coastal environments (Callaghan et al., 2008, Almeida et al., 2011, Mull and Ruggiero, 2014). The KD93 has no calibration parameter and is therefore applied using the recommended settings.

It essentially uses a convolution integral to represent the lagged and damped response of the beach towards an equilibrium retreat distance (R_∞), which it approaches under at an approximately exponential rate:

$$R(t) = \frac{R_\infty}{T_s} \int_0^t f(\tau) e^{-(t-\tau)/T_s} d\tau \tag{4.3}$$

with τ the time lag between the hydrodynamic and morphological response and T_s the representative time scale of exponential response. Sediment is eroded and moved offshore until a new equilibrium profile is established. In other words, if the forcing were held constant for an unlimited long duration, $R(t)$ approaches R_∞. KD93 find R_∞ to be a function of the hydrodynamic parameters storm surge (S) and depth of breaking waves (h_b), and the morphological parameters berm height (B), beach slope ($tan(\beta_b)$), and the surf-zone width (x_b), the latter being a function of the equilibrium profile parameters A and m. Details on solving the convolution integral and input parameters needed are described in Appendix C.

In short, the maximum retreat R_{max} is the retreat distance it can reach given the storm duration and is thus a fraction of the equilibrium retreat distance R_∞. The fraction is determined by the parameter β, which is the relative duration of the storm to the exponential response time scale T_s. Shorter duration storms reach smaller fractions, and the duration is thus equally important as the magnitude of the forcing. For instance, extreme but short term events (e.g. hurricanes) might reach lower R_{max} compared to a moderately extreme but persistent event (e.g. swell).

This formula can now be solved given the hydrodynamic from the SSTS and morphological input and R_{max} is estimated for every storm. Because the main focus of the work is to study the impact of SLR, morphological parameters are kept deterministic throughout the analysis.

4.2.6. Shoreline position

The rate of shoreline change is generally proportional to the wave energy and its antecedent position (Yates et al., 2009, Davidson et al., 2013). After a storm has eroded the beach, wave driven transport and aeolian processes will move sediment back to the beach and (partly) recover it before a new storm hits. With SLR, however, the magnitude of storm erosion will gradually increase and the beach does not have enough time to recover from extreme events (since extreme events are occurring more frequently). This drives a net sediment loss over the years, hence long-term recession CR of the coast.

To forecast the shoreline position, the shoreline movement in between the storm events needs to be quantified. For this, a representative recovery rate of the system is needed. An approach similar to Ranasinghe et al. (2012) and Li et al. (2014) is followed, but a deviation is made by introducing a simple state dependency. As was mentioned in section 4.2.2, the same wave height could erode a beach that is in a state of accretion, while it can accrete a beach that is already eroded. Something similar is thus expected for the storm events.

On the long-term, a shoreline oscillates around a given equilibrium position. Without additional forcing or sediment sinks or gains, this position is represented by the median value of the cumulative distribution function (CDF), and should ideally be zero. Everything above this line is then a 'state of accretion', whereas everything below this line is a 'state of erosion'. The state dependency is enforced as follows;

- If a shoreline is in a state of accretion (green color Figure 4.8) and a storm hits, the retreat distance will be simply be added to the shoreline, and will erode.
- If the shoreline is in a state of erosion (red color Figure 4.8), the position of the shoreline will influence the behaviour. When the shoreline position is closes to the equilibrium position than the magnitude retreat distance from the storm, the shoreline will erode towards this retreat distance. However, if the position of the shoreline is further away from equilibrium than the magnitude of the retreat distance, the position will first halt and then recover.

In general, it means that a larger storm is needed to erode an already eroded beach (Yates et al., 2009).

For the recovery periods in between storms, a linear recovery rate is introduced. This linear recovery rate can be interpreted as a representative, or weighted average, recovery rate over a long period of time that, on average, will stabilize the coast. To find a representative recovery rate, one iteratively searches for a recovery rate that stabilizes the coast (no net recession) under a 500 yr simulation time in absence of SLR (storm forcing

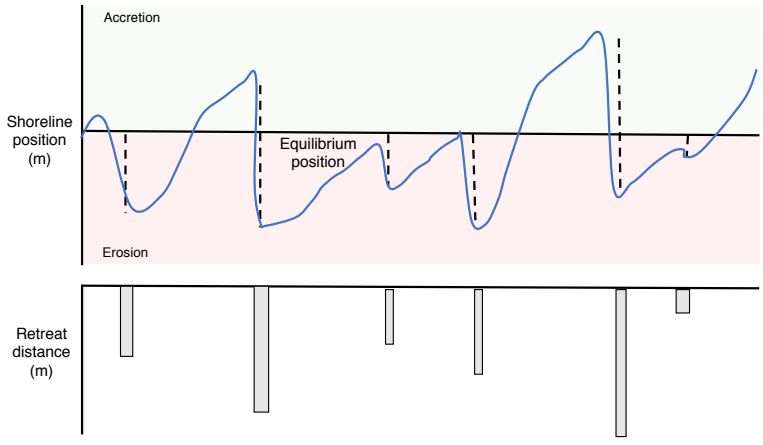

Figure 4.8: Schematic of the shoreline model as implemented for shoreline prediction. The blue line indicates the shoreline position over time. The retreat distance indicated by the grey bars (with the width of the bar the storm duration) are erosion events caused by storms. Different initial positions of the shoreline lead to different response, depending if being in a state of accretion (green) or state of erosion (red).

only). For Orient Bay, a representative recovery rate of 0.10 m day^{-1} is found, whereas for Dawn Beach, this recovery rate is 0.165 m day^{-1}. This is close to linear recovery rates mentioned in literature of 0.04-0.20 m day^{-1}, as summarized in Phillips et al. (2017).

4.3. Sampling and analysis

The above described methodology can be repeated multiple times. This is done by; (1) sample a SSTS together with a SLR pathway for 2006-2100, (2) calculate retreat distances due to storms, (3) forecast the shoreline behaviour using the recovery rate, (4) analyse the retreat distance and long-term recession over the 95 year period, (5) repeat 10,000 times to obtain probabilistic estimates for all 12 SLR cases.

For the episodic storm erosion, a generalized Pareto distribution is fitted to the data and the return periods are calculated over the 2006-2100 period. The average shoreline position in 2100 is used to obtain CR estimates for 2100 compared to 2006.

4.4. Validation shoreline mobility

To validate the variability of the shoreline (due to the storms), SDS data and the 500 yr model run are compared. First, the seasonal low frequency motion is removed. This seasonal motion arises due to the (random) sequence and magnitude of storms. A 1 year running mean (grey line) is first calculated and removed from the observations (red line) and modelled run (see Figure 4.9a). Both results are interpolated on a 1 day grid (because the SDS have non-equal time intervals between measurements). The resulting CDFs for Orient Bay are illustrated in Figure 4.9b. The standard deviation is a measure of the 'beach mobility' of the beach and is controlled by the morphodynamic state of the beach (Stive et al., 2002). A comparison is shown in Figure 4.9 for Orient Bay. The standard deviation of the detrended SDS is 3.3 m compared to a standard deviation of 3.5 m for 500 yr run, indicating that the beach mobility is resembled well.

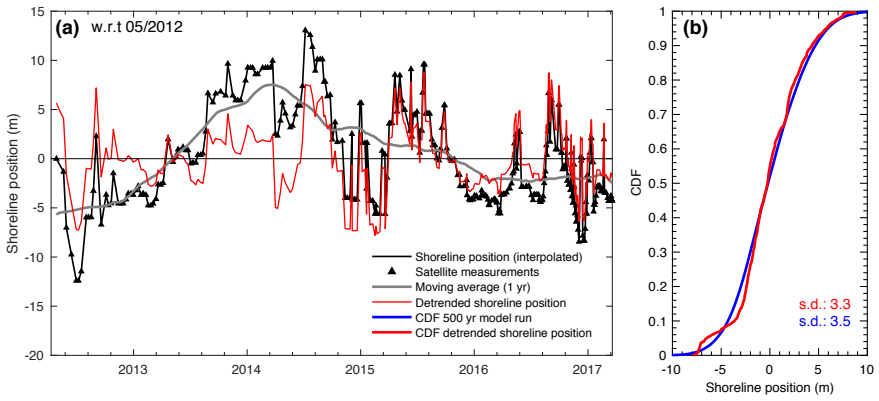

Figure 4.9: (a) Shoreline position based on Satellite derived shoreline (SDS) positions (black diamonds and solid line). The 1 year moving average (grey line) is removed from the SDS to obtain the detrended positions (red). (b) Cumulative distribution function (CDF) of the detrended shoreline positions. Red is based on detrended positions in (a) and blue based on a 500 year model run (also detrended). s.d. = standard deviation of shoreline positions.

5 Results: projections of sea-level rise and coastal erosion

5.1. Sea-level rise projections

Figure 5.1a-b&d-e depicts the 21st century RSLR projections for Sint Maarten given the two RCP-scenarios considered together with recent altimetry time series [1] and an ensemble of 3yr running averages of tide gauges in the region[2]. Results for 2100 compared to 1986-2005 are presented in Figure5.1c&f and also tabulated in Table 5.1. The regional scale factor illustrates how RSLR estimates relate to GMSL rise (RSLR/GMSL rise). Apart from median and 90% uncertainty bandwidth, a more upper range estimate of the 99th percentile is provided. DP16 and IPCC are nearly symmetrical (blue and red lines in Figure5.1c&f) with projections of respectively 200 ($\pm$40.2) cm and 73 ($\pm$15.8) cm for RCP8.5 and 108 ($\pm$27.4) cm and 54 ($\pm$12.2) cm for RCP4.5 ($\mu \pm \sigma$). The skewed total distribution function for the LEV14 has a median value of 80 cm and 95th percentile of 121 cm for RCP8.5 versus a 56 cm and 86 cm for RCP4.5. The heavy weighting of the AIS to total RSLR leads to estimates that are 6-18% higher than GMSL rise for the upper limit. Considering

[1] Obtained from https://www.aviso.altimetry.fr/en/home.html
[2] Obtained from www.psmsl.org

RCP8.5												
	Sea level rise (cm)						Regional factor					
	$\gamma = 1.0$			$\gamma = 1.64$			$\gamma = 1.0$			$\gamma = 1.64$		
Percentile	DP16	LEV14	IPCC	DP16T	LEV14	IPCC	DP16	LEV14	IPCC	DP16T	LEV14	IPCC
5.0	135	53	49	83	42	40	1.10	0.91	0.91	1.09	0.91	0.87
50.0	200	80	73	200	81	74	1.14	1.01	1.00	1.14	1.03	1.01
95.0	266	121	100	321	134	111	1.17	1.08	1.05	1.15	1.06	1.05
99.0	294	150	112	375	168	128	1.18	1.10	1.06	1.16	1.08	1.03
RCP4.5												
	Sea level rise (cm)						Regional factor					
	$\gamma = 1.0$			$\gamma = 1.64$			$\gamma = 1.0$			$\gamma = 1.64$		
Percentile	DP16	LEV14	IPCC	DP16T	LEV14	IPCC	DP16	LEV14	IPCC	DP16T	LEV14	IPCC
5.0	64	37	34	35	28	28	1.05	0.95	0.92	1.03	0.90	0.88
50.0	108	56	54	108	57	54	1.13	1.02	1.04	1.13	1.04	1.04
95.0	152	86	74	184	95	80	1.16	1.09	1.09	1.15	1.08	1.07
99.0	171	109	82	219	120	92	1.17	1.12	1.09	1.16	1.10	1.08

Table 5.1: Regional sea-level rise projections for Sint Maarten for 2100 compared to 2006 together with the regional scaling factor.

time evolution, the three cases do not deviate to a noticeable extent until 2045-2050, after which an onset of Antarctic mass ablation causes the projections to diverge (Figure5.1a&d). The inclusion of the additional model uncertainty (refer back to 4.1.1), does not affect the median much, but it does alter the total uncertainty of RSLR (Figure5.1b&e). The difference between the $\gamma = 1.0$ case and the $\gamma = 1.64$ is shown in Table 5.1 and Figure 5.1c&f (with dashed lines $\gamma = 1.64$). The regional factor will not change much (because it is scaled). Including this additional model uncertainty will increase the 5-95th percentile uncertainty with 107 (61) cm for DP16, 24 (18) cm for LEV14 and 20 (12) cm for IPCC given RCP8.5 (RCP4.5). It thus adds up to the elongation of the distribution width and the skewness, if any, intensifies.

The projections for other parts of the Caribbean basin are shown in table D.1 in appendix D, and do not differ distinctively from the Sint Maarten projections with maximum differences of 9 cm in the 99th percentile and 5 cm in the 50th percentile.

The rate of SLR over time shows an acceleration from the 3 mm yr^{-1} observed nowadays up to 5 mm yr^{-1} and 12 mm yr^{-1} for RCP4.5 and RCP8.5 at the end of the century for LEV14 and IPCC. The DP16 projection shows, however, a moderate decline relative to modern rates till 2040 followed by a rapid acceleration, reaching 21 mm yr^{-1} and 50 mm yr^{-1} for RCP4.5 and RCP8.5, respectively, at the end of the century. This value may surpass many vertical accretion rates of mangroves in the region (Parkinson et al., 1994, McKee, 2011, Woodroffe et al., 2016), and accretion rates of coral reefs (-0.26-4.00 mm yr^{-1}) on Sint Maarten (Perry et al., 2018) at the end of the century.

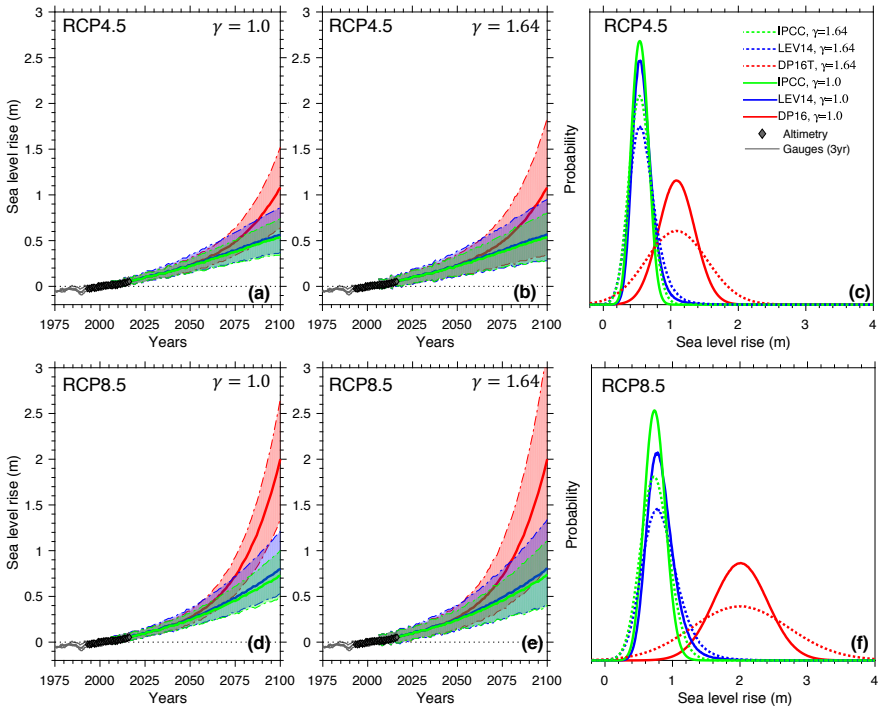

Figure 5.1: (a) Regional SLR projections from 2006 to 2100 for RCP4.5. Grey line indicate 3 year running average of tidal gauge stations and grey diamonds recent altimetry data for the Caribbean. (b) same as (a) but with additional model uncertainty ($\gamma = 1.64$). (c) PDFs of 2100 Regional SLR compared to 1986–2005 under RCP4.5 for both including (dashed lines) and excluding (solid lines) model uncertainty. (d-f) same as (a-c) but for RCP8.5.

5.2. Retreat distance

SLR contributes to the increased frequency of extreme water levels and thereby increased retreat of the shoreline due to the impact of storms. Future return periods over the years 2006-2100 are given in Figures 5.2a-d for $\gamma = 1.0$, whereas the $\gamma = 1.64$ results are displayed in Figure E.1 in Appendix E. For comparison, the black line in Figure 5.2a-d is the baseline case without SLR. The magnitude and uncertainty bandwidth are comparable with the SLR projections, with DP16 the highest number and largest uncertainty. Moreover, the uncertainty for RCP8.5 is larger than for RCP4.5.

For Orient Bay for example, the return period of a 1/100 year retreat event is 1.67 (2.4) times higher for DP16 and around 1.4 (1.5) times higher for LEV14 and IPCC compared to the baseline under RCP4.5 (RCP8.5). Figures 5.2e-f show the correlation between the SLR-value for a given year x and the 1/100 year retreat distance over the years (thus from 2006 to year x). The SLR value sampled determines the trajectory taken. If there is a low correlation, the SLR value sampled was apparently not a driving force for this 1/100 year erosion event (storm randomness dominates). Until 2060-2070, the correlation is still below 0.5 implying a moderate dependency. Thus the increase in surge will not alter the extreme value statistics much. For DP16 and LEV14, the correlation in 2100 is close to 0.8-0.9 meaning that SLR is steering the extreme erosion over the storm randomness. This also implies that SLR is almost linearly related to storm erosion. For Dawn Beach, this correlation is less pronounced, largely due to the more concave upward shape of extreme value distribution. A similar concave upward profile was found by Callaghan et al. (2013) for a beach in Australia when applying KD93. However, it is likely that a certain upper limit exists and that this shape might not physically correct.

The difference between the two beaches can also be explained more physically. Dawn Beach has a steeper beach slope and foreshore slope, therefore higher wave set-up and wave breaking closer to the shore. According to Kriebel and Dean (1993), this yields a more reactive beach in terms of morphological response. This makes

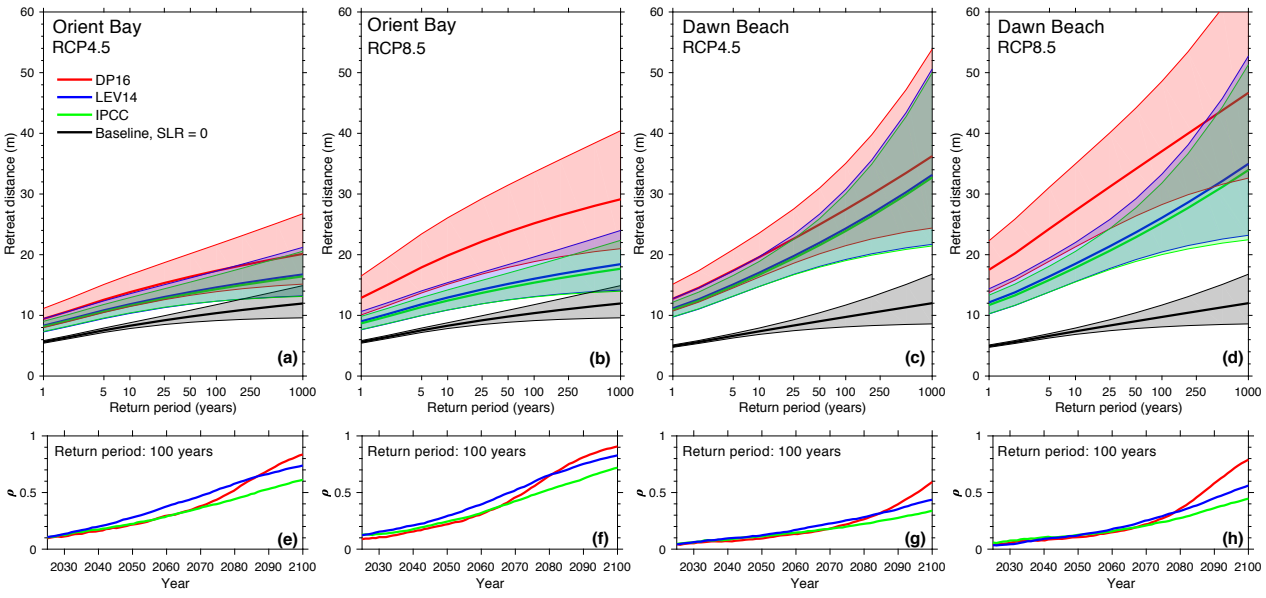

Figure 5.2: (a) Return periods of retreat distance due to storm events over the period 2006-2100 for Orient Bay under RCP4.5. Solid line is the median value, whereas the shaded area represent the 90% uncertainty bandwidth. The black line is the baseline case for a situation without SLR. (b) same as (a) but under RCP8.5. (c-d) same as (a-b) but for Orient Bay. (e) Correlation between sample year x SLR and the calculated 1/100 year retreat distance over 2006-year x for Orient Bay under RCP4.5. (f) same as (e) but under RCP8.5. (g-h) same as (e-f) but for Dawn Beach. All figures are without considering additional model uncertainty ($\gamma = 1.0$).

it less sensitive to an increase in storm surge and more sensitive to the other parameters influencing the storm erosion.

Note that the term return period adopted here is different from the conventional definition of return period. We define return period as the average rate of occurrence of an event integrated over a given time span, here from 2006 till 2100. For instance, the 1/100 year event will happen once in a 100 year period from 2006-2100. The 1/50 year will thus happen approximately twice over this period. However, because SLR is a non-stationary process, the occurrence of extreme return periods will happen more likely close to 2100 than 2006.

5.3. Recession

Finally, the structural erosion, or recession for 2100 is summarized in Figure 5.3. First of all, Dawn Beach will experience larger recession, in line with the larger retreat distances, influenced by the morphological character of the beach. Median recession values (black dot and diamond upper panel) range from 6-22 m for Dawn Beach and 5-16 m for Orient Bay (lower range IPCC, upper range DP16). However, the 1% exceedence probability (thin line upper panel) range from 11-46 m for Dawn Beach and 9-38 m for Orient Bay. The 1% coastal recession value of the IPCC for Orient Bay needs to be, on average, 1.75 (2.67) times higher in case of DP16 and 1.14 (1.21) times higher for LEV14 to have the same amount of safety for RCP4.5 (RCP8.5). The additional model uncertainty will hardly affect the median, but does broaden the PDF of the recession, similar to the PDFs of SLR. For instance, the 1% exceedance probability for Orient Bay is now 2.12 (3.43) times higher for DP16 and 1.16 (1.24) time higher for LEV14 compared to the IPCC for RCP4.5 (RCP8.5).

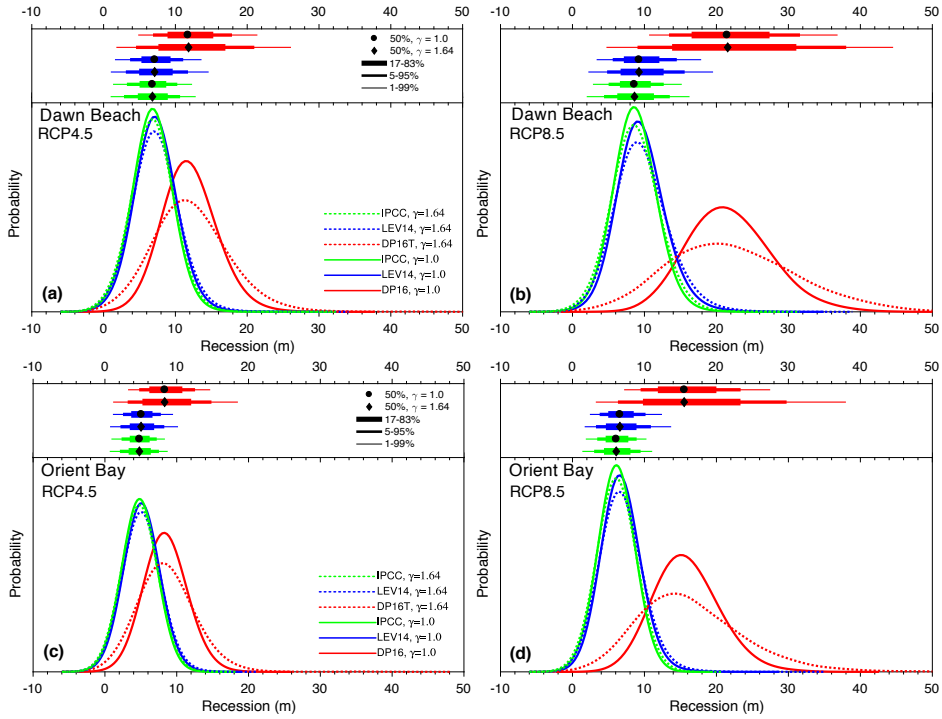

Figure 5.3: (a) PDFs of 2100 recession value compared to 2006 for Dawn Beach under RCP4.5. Include both including (dashed) and excluding (solid) model uncertainty. In the top panel, the 50th percentile is shown together with the 66%, 90% and 98% uncertainty range. (b) same as (a) but under RCP8.5. (c-d) same as (a-b) but for Orient Bay.

6

Results: implications for decision-making

6.1. Retreat distance

The main objective was to quantify the sensitivity of future erosion estimates to different formulations of the AIS dynamics into SLR projections. Stated otherwise, what is the difference when adopting the IPCC case compared to the other cases?

For the retreat distance this is done by considering the estimates of the IPCC for every return period and search the corresponding return period for the other two cases (e.g. the median 1/100 yr erosion event has a value of 30 m for IPCC. 30m corresponds to a median 1/x yr return period for case y). The result of this is made visible in Figure 6.1. The dashed black line indicate perfect alignment between the two (no difference) with larger deviation indicating larger difference. For example, a 1/100 yr erosion event for IPCC at Orient Bay (vertical black line) equals a 1/80 (1/50) event for LEV14 (solid blue line) and a 1/15 (1/1.5) event for DP16 (solid red line) for RCP4.5 (RCP8.5). Therefore, this event will occur 1.25-40 times as frequent over the same time span. For Dawn Beach, this effect is slightly less with 1/90 (1/80) for LEV14 and 1/35 (1/6)

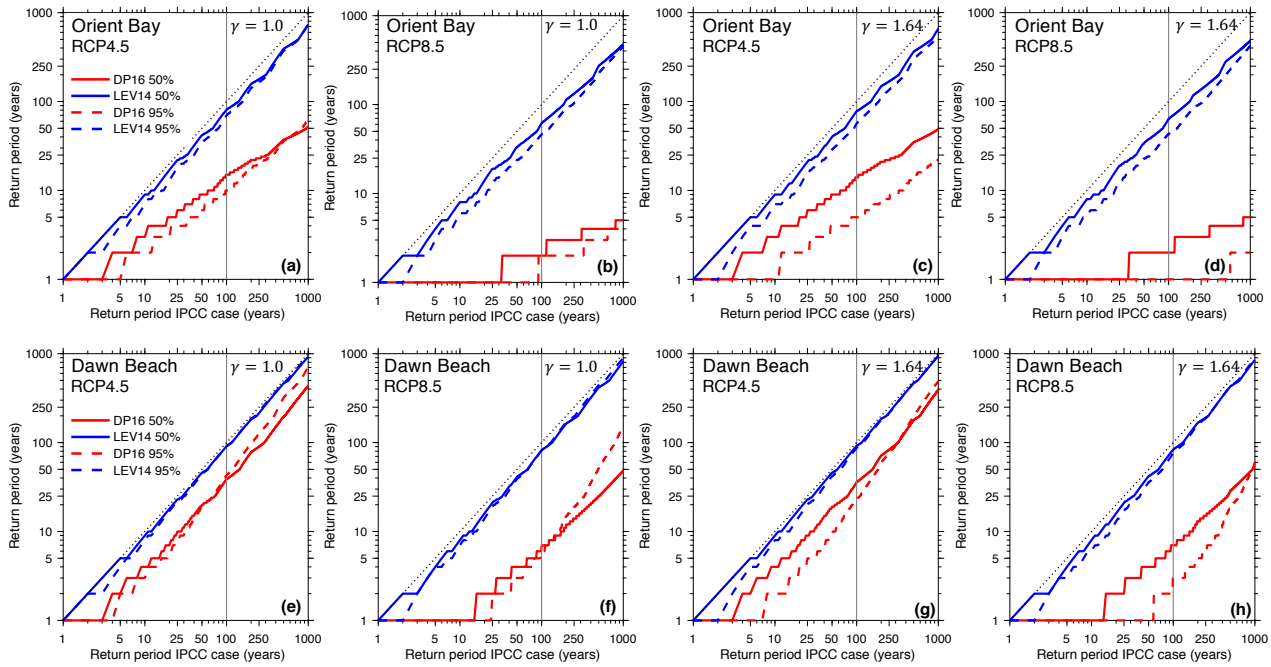

Figure 6.1: (a) Comparison between return periods of retreat distance from storm events under the IPCC scenario and the DP16 (red) and LEV14 (blue) scenario. The dashed black line indicate perfect agreement (no difference) with larger deviation from this line indicating a larger relative underestimation. For Orient Bay under RCP4.5 without additional model uncertainty ($\gamma = 1.0$). (b) same as (a) but for RCP8.5. (c-d) same as (a-b) but with additional model uncertainty ($\gamma = 1.64$). (e-h) same as (a-d) but for Dawn Beach.

for DP16 given scenario RCP4.5 (RCP8.5). For larger return periods, underestimation is generally larger and under the RCP8.5, the results divergence even more.

Those who want to build in additional safety and adopt the 95% value are even more likely (relatively speaking) to underestimate the risk in most cases. This is again due to difference in uncertainty bandwidth in SLR that propagates to the storm erosion estimates. For this, the 1/100 year event for Orient Bay under the IPCC scenario may even occur 1.54 (2.22) times as frequent under LEV14 and 10 (67) times as frequent for DP16 for RCP4.5 (RCP8.5). This is visualized using the dashed blue and red lines in figure 6.1a-b&e-f, which are typically more downward compared to the median values, except for some high return period for Dawn Beach. For clarity, for the 95th percentile curve, a comparison is made between the IPCC 95th percentile value of LEV14 and DP16 95th percentile values (e.g. the 95th percentile 1/100 yr erosion event has a value of 30 m for IPCC. 30m corresponds to a 95th percentile 1/x yr return period for case y). Adding the additional model uncertainty ($\gamma = 1.64$) further fortifies this effect for the 95th percentile, as shown in Figures 6.1c-d&g-h. This is due to the larger uncertainty in the SLR projections for LEV14 and DP16 compared to the IPCC, hence also wider uncertainty for the erosion estimates. Thus, the decision whether or not to include this mainly affects actors who have a strong risk-averse appetite.

6.2. Recession

The same relative plots for the recession in 2100 compared to 2006 can be made, but now expressed in terms of exceedance probability. This is done in Figure 6.2 for the cases of including (dashed) and excluding (solid) model uncertainty. Again, larger deviations from the perfect alignment (dashed black line) indicate larger differences (but now above this line). Large deviations are found when AIS uncertainty is not included, and in particular the lower exceedance probabilities show wide divergence. For instance, the 1% exceedance probability in 2100 has a 2-4.5% exceedance probability for a skewed distribution function and a 37-88% exceedance probability under a high-end scenario of the AIS. This means that risk-averse coastal managers, who are adopting low-probabilities, are prone to misconception about their level of safety. Overall, underestimating the contribution of the AIS may lead to unacceptable situations in terms of risk faced by the coastal communities.

Besides the safety issue, a given recession value under the IPCC case will occur some years earlier for the LEV14 and DP16 case. A mitigation measure to counterbalance recession, such as a nourishment, is often

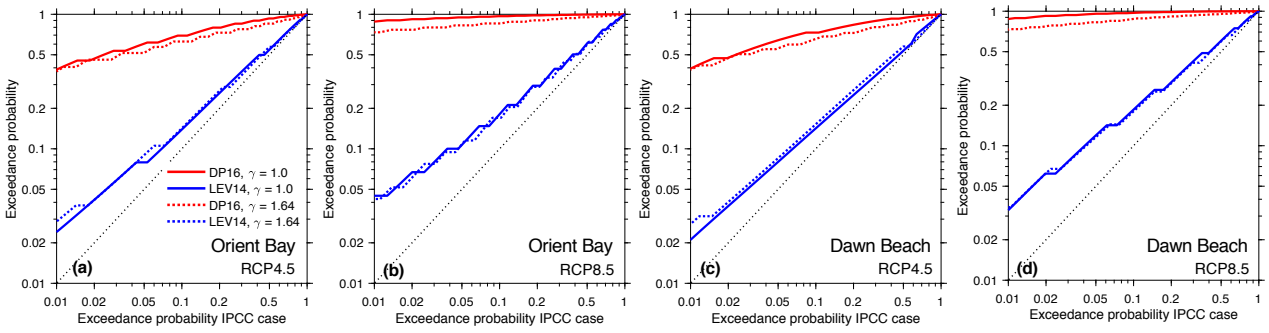

Figure 6.2: a) Comparison between exceedance probabilities of recession values in 2100 compared to 2006 under the IPCC scenario and the DP16 (red) and LEV14 (blue) scenario. The dashed black line indicate perfect agreement (no difference) with larger deviation from this line indicating a larger relative underestimation. For Orient Bay under RCP4.5 with (dashed) and without model uncertainty (solid). (b) same as (a) but under RCP8.5. (c-d) same as (a-b) but for Dawn Beach.

designed based on cost-optimization of periodic supplements of sediment (Lazarus et al., 2011). The cost-efficiency of such a design can be altered by the accelerated pace of SLR-induced recession. The question is now; how much earlier will a given exceedance probability in 2100 under the IPCC case occur for the two other scenarios?

The recession values under the IPCC case in 2100 are calculated for limited number of exceedance probabilities and the corresponding years are found where the recession value is reached for the LEV14 and DP16 case. This is displayed in Figure 6.3. For DP16, the same exceedance probabilities for the IPCC case will be reached 20-25 years earlier, almost independent of the exceedance probability adopted. For LEV14 on the contrary, there is a dependency on the exceedance probability adopted, and the acceleration in terms of years is between 2-15 years. Lower exceedance probabilities in general have a larger acceleration in terms of years, again important for the risk-averse coastal manager. Given that SLR projections do not deviate from each other until 2060, this acceleration is considered large and will happen quickly, posing large uncertainty for the cost-efficiency of measures.

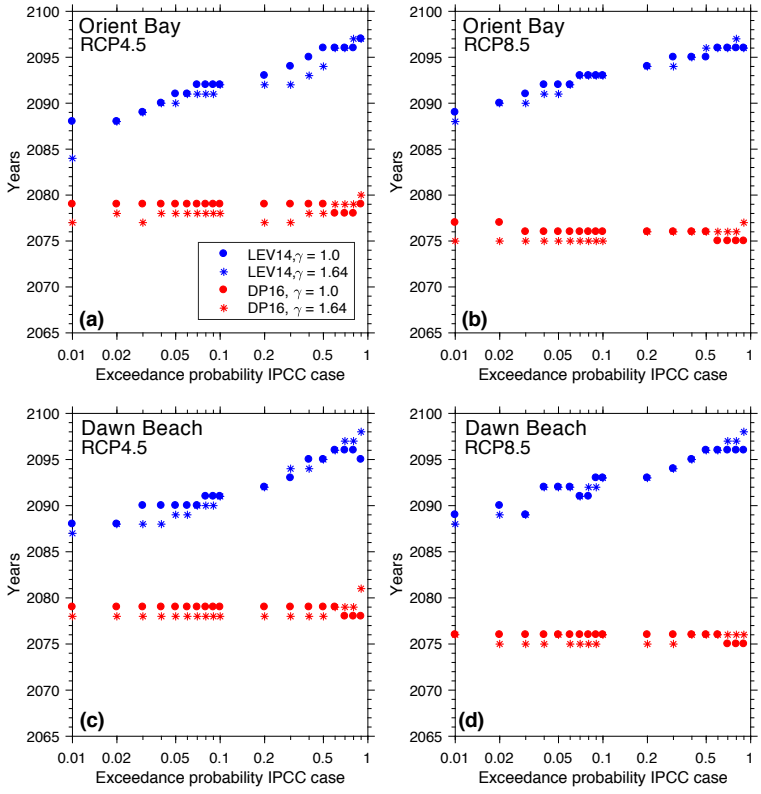

Figure 6.3: (a) Comparison of years that corresponds to the recession values found under the IPCC case in 2100. Dots indicate the exceedance probabilities that are used. Result is for Orient Bay given RCP4.5. (b) same as (a) but given RCP8.5. (c-d) same as (a-b) but for Dawn Beach.

6.3. Uncertainty analysis

Although the aim was to primarily quantify the SLR uncertainty, it is interesting to take it one step further and look how the climate uncertainty (SLR+model uncertainty) relates to the morphological uncertainty that can be expected. The erosion model considered up till now uses the narrow assumption of invariant cross-shore profile (thus deterministic). Real cross-shore profiles are however very dynamic. Therefore, a sensitivity analysis is performed based on variance decomposition of the 1/100 year retreat distance over 2006-2100. The morphological parameters are now assumed to be probabilistic as well, modelled by a triangular distribution

function with the peak at the deterministic value presented in the method. The beach slope $tan(\beta)$, foreshore slope $tan(\beta_{fs})$ and berm height (B) are assumed to have a upper/lower limit of 10%, whereas the equilibrium profile parameter A and b have an upper/lower limit of 5% (to prevent very larger variations for large depths). In reality, these morphological parameters are coupled (dependent), but this assessment is purely for illustrative purposes, and therefore independence is assumed.

The following procedure is followed: first calculate the 90% uncertainty bandwidth of the 1/100 year return period including SLR uncertainty, climate model uncertainty and morphological uncertainty. Then, perform additional runs by replacing one of the components with its expected value (make it deterministic) and assess how this reduces the total uncertainty. For model uncertainty, a run with and without are subtracted. The remaining uncertainty after replacing the three components is the uncertainty caused by the sampling method of the storms (future storm uncertainty). By comparing, one can get an idea about the relatively importance of these four components to the overall uncertainty in the model. Results are shown in Figure 6.4 for all SLR cases. The morphological uncertainty is very dominant, indicating that the model is sensitive to different parameters settings. Stated otherwise, if morphological variability is to be expected, it should be included. The climate uncertainty (SLR+model) has only a marginal role before 2070, but increases towards the end of the century. Especially for DP16, it accounts for 40% (60%) of the total uncertainty in 2100 for RCP4.5 (RCP8.5). This illustrates that using a deterministic value of SLR, one considerable underestimates the total uncertainty in the model results.

A next step would be to assign probabilities to the RCP-scenarios and AIS dynamics case in order to include the six frames in one figure. There is however no general consensus about the likelihood of RCPs and the likelihood of AIS dynamics. A method could be to make them equally like, as done in Le Cozannet et al. (2015), thus use a discrete uniform distribution. This is however, not further explored.

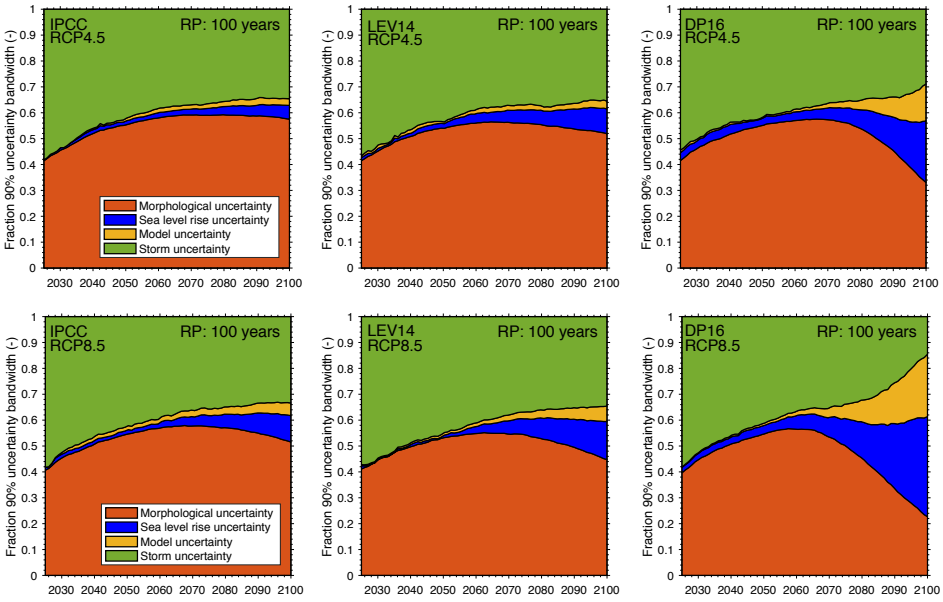

Figure 6.4: Plots showing the fraction of the 90% uncertainty of the 1/100 year retreat distance over the 2006-2100 period. Plot show different cases of AIS included in the SLR projections and different climate scenarios. The width of the area shows the importance in the total uncertainty.

7 Discussion and way forward

7.1. Discussion

To allow the integration of SLR and erosion within a probabilistic framework, several assumption and caveats are inherent to the method. In general, the field of coastal engineering is at the interface of climate science (boundary conditions) and coastal science (physical basis). One can argue that the uncertainties accumulate at the scale (temporal and spatial) where the coastal engineer is active (see Figure 7.1). For instance, assessing climate impact at a local scale is challenging, since climate models have resolutions of 100-200 km. In coastal science, the physics behind sediment transport on very small scales are (largely) understood, but skillful predictions of sediment transport on engineering time and spatial scales remain troublesome. Therefore, uncertainties arise from both 'top-down' as well as 'bottom-up'.

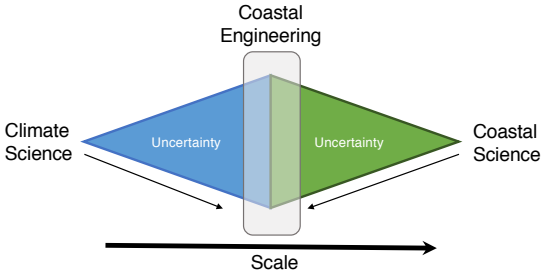

Figure 7.1: Schematic of the position of coastal engineering on the interface of climate science and coastal science, with the spatial scale from left to right.

The SLR projections used are considered state-of-the-art, nonetheless have large uncertainties associated with them. As was already introduced in the main part, climate models have common biases, which affects the reliability of climate model output. Known difficulties are the misrepresentation of physical processes on sub-grid scale such as eddies (Sérazin et al., 2016), representation of the AMOC (Maraun et al., 2017) and intermodel differences in ocean heat uptake efficiency (Kuhlbrodt and Gregory, 2012). A new climate model database (CMIP6) is will launch in the upcoming years that will replace the CMIP5 models used now. For the SLR projections, we do no include vertical land movement of the island, since data on this is not available. Moreover, RCP2.6 and RCP6.0 are not considered. This is because RCP6.0 is comparable to RCP4.5, and RCP2.6 gives similar results of AIS dynamics in Church et al. (2013), Levermann et al. (2014) and DeConto and Pollard (2016), because rapid mass loss is not yet initiated. Concerning the sea-level fingerprints, the prediction of redistribution of mass is fairly robust. The uncertainty here stems from the approximation that the ice sheet is losing mass uniformly. Larour et al. (2017) shows how different coastal areas are sensitive to different drainage locations on both ice sheets. Updating other components due to scientific advances is not considered. This potentially includes new research into glaciers contribution (Huss and Hock, 2015), regionally variable mass loss from Greenland SMB (Meyssignac et al., 2016), new estimates of precipitation

increase over the AIS (Palerme et al., 2017), and newly established AIS mass balance (IMBIE team, 2018). By far the largest uncertainties remain in predicting the response of the AIS over decadal to centennial time scales. Ice sheet models have only recently come to a point where they can reproduce observed ice sheet changes and move towards making refined future projections (Pattyn, 2018). However, so far no numerical model study has reported values as high as DeConto and Pollard (2016) and an >1.0 meter AIS contribution is still debated (Schlegel et al., 2018, under review).

As was showcased with the different AIS cases and the inclusion/exclusion of additional model uncertainty, making SLR involves making non-trivial design choices. Users are unaware of such choices. Since it influences the results, hence the decision-making, transparency of such non-trivial choices is essential.

Furthermore, it is assumed that SLR will rise at an annual uniform rate. This approach does not consider other nonstationarities in sea-levels or wave climate, which may be present in coastal areas (Wahl and Plant, 2015, Davies et al., 2017, Melet et al., 2018). This variability is often linked to larger scale atmospheric dynamics. For example, a negative correlation is found between the monthly Niño3.4-index and mean and maximum monthly wave height (ρ = -0.33 for mean, ρ = -0.37 for max), indicating that interannual variability in storm forcing is present (see appendix C.4). Moreover, trends in offshore storm parameters are not considered here, which may change future hydrodynamic conditions. (Vousdoukas et al., 2018). Such longer term modulations can affect the erosion hazard. For instance, changes or variability in incoming wave direction can initiate shoreline rotation on pocket beaches and embayed areas (Bowman et al., 2009, Ranasinghe, 2016). This may al be incorporated into a more advanced statistical model that better includes nonstationary conditions (Davies et al., 2017). In this study, boundary conditions are provided by globally-covering model with a spatial resolution of ~75 km. Therefore, extreme waves and surges due to for instance hurricanes are not well resolved.

Although the KD93 formula has shown to be accurate, it should be used as a first-order predictor. For instance, it does not solve the means by which sediment is transported, only the development of the cross-shore profile over time. The most important assumptions in formula are that an equilibrium profile exists and the morphological response is exponential. Also the assumption made that the cross-shore profile will react similarly over the years is subject to discussion. The coastal response to a given storm can be quite different on a year 2100 coastal profile that has already adjusted to 1m of SLR (Ranasinghe, 2016). The application here is on a beach which little expected alongshore current and approximately shore normal waves. Hence little alongshore sediment movement is expected. If known, other sources of the sediment budget may be added, such as aeolian transport and overwash during storm, sinks to tidal basins, or sand sources due to nourishments (Rosati et al., 2013, Dean and Houston, 2016). Also, insight into seasonal and interannual variability of the shoreline is needed and can be added. For instance, using a 2 year running average, a small oscillating motion can be identified in the satellite derived shoreline position.

Moreover, setting the threshold needs further investigation. Using the satellite measurements, not all eroding moments of the beach were associated with identified storms. This can have several reasons. The accuracy of the SDS are on average around 1-30 m, depending satellite mission, cloud cover and wave presence (Hagenaars et al., 2018). Also, because the recurrence interval of SDS measurements is 1-16 days and storm events have a duration of hours-days, small storm erosion events might already be recovered. Also, the recovery rate of the beach is derived using an iterative process, whereas it could be measured in reality. In our case, varying the recovery rate by 25% changes the median values of the 2100 recession by $\pm$2.2m for Orient Bay

and $\pm$3m for Dawn Beach, which is considerable given the results. In reality, the recovery rate is also coupled wave energy. Developing a process-based, yet simple model of dune/beach recovery is desirable for long term coastal evolution modelling (Ranasinghe et al., 2012). Finally, compared to the 'Bruun Rule', the estimates here are much smaller. For a first order estimate, the Bruun Rule estimates recession values of 50-100 times SLR. This would yield 27-108 m for RCP8.5 and 35.6-200 m for RCP4.5 given the median SLR projections. However, results here only find median values ranging from 6-22 m for Dawn Beach and 5-16 m for Orient Bay. Large overestimations were also found by Ranasinghe et al. (2012) for an application in Australia.

7.2. The way forward

This bring us to the way forward. To overcome uncertainties and steer the debate, climate and coastal research communities should not be isolated from each other, but should work in synergy to better align SLR information to coastal adaptation decisions. This should start by admitting that SLR uncertainty exists and may be larger than any of the morphological uncertainties that receives much more attention in the coastal research community. Future research should focus on integrating and propagating the uncertainties into systematic way. This includes adding morphological uncertainties of the parameters and the natural variability of the shoreline on time scale from years to decades to the model. Development of reduced complexity models to enable probabilistic input can be used to bridge this gap. Alternatively, innovative modelling approaches can be considered to model the SLR response in complex geomorphological settings, such as using a Bayesian Network (Lentz et al., 2016), advanced statistical methods (Toimil et al., 2017) or other surrogate models.

More importantly, efforts should be made to derive an authoritative projection of SLR specifically designed for coastal management purposes to guide the use of upper quantile estimates. Proposing different scenarios, as is done in this work, already provides insight into the deep uncertainties and a tool for decision support. Others suggest that possible futures cannot be objectively described by a single well-defined PDF (Kunreuther et al., 2013), promoting the use of other methods such as extra-probability methods (Le Cozannet et al., 2017) or expect elicitation (Bamber and Aspinall, 2013, Horton et al., 2014, Oppenheimer et al., 2016). More formalized methods to asses deep uncertainties and construct robust decision-making pathways could assist this development (Haasnoot et al., 2013, Sriver et al., 2018). Although we have focused primarily on the hazard component, risk management is a balance between risk and reward and the economic consequences of SLR-induced erosion needs to be coupled to this framework (Jongejan et al., 2016). This includes the evaluation of potential engineering solutions, such as nourishments as done by Hinkel et al. (2013). Until now, engineering strategies to mitigate extreme SLR are lacking in literature, although insight in their suitability is desired. Considering the uncertainty posed, emphasis on flexibility in the design is required, which paves the way for measures that have a certain adaptive ability such as large scale nourishments (Stive et al., 2013) or nature-based solutions (Temmerman et al., 2013). At last, our approach could be easily extended to regional or global coverage (see Section 7.3). This could help identify the most vulnerable areas, quantify global consequences of SLR and assist global adaptation efforts.

7.3. Upscaling and reproducibility

The methodology described here is applied to only one case study, but can be easily extended to any other area or upscaled. For this, one can distinguish between essential data input to perform an analysis, and additional

data which may help to improve the accuracy of the analysis.

In terms of SLR projections, any area of interest can now be described accordingly, whereas upscaling to larger areas is straightforward. Note that local processes, such as land subsidence or tectonic movements need to be considered if known to be substantial. In terms of hydrodynamic input, all data is obtained from open data sources covering the globe. Validation with wave buoy data is highly advisable in areas where hurricanes are known to occur. Moreover, sheltering effects of small islands are not considered in the open ocean areas. Non-tidal residuals can also be obtained from tide gauge, although care should be taken when tide gauges are located in sheltered area, since they do not capture (or dampen) the contribution of wave set-up and swash (Melet et al., 2018). It should always be checked if offshore wave height can be used as a proxy for shoreline change. In some areas, extreme surge levels are the dominant sources of beach change (Kriebel and Dean, 1993). Also, in areas where the nearshore bathymetry is irregularly spaced, or when refraction and diffraction processes are important, a predictive formula for wave breaking as used here may not adequate. Upscaling this approach should be accompanied by an assumption for a general storm threshold (e.g. percentage of maximum wave height).

The required input of morphological data is dependent on the type of erosion formula. For the KD93 formula, only data on the equilibrium profile parameters (A and m) and the beach slope ($tan(\beta)$) are needed. For many predictive wave set-up/swash formulas, the beach slope is the only data needed (Stockdon et al., 2006). m is often close to 2/3, whereas A can be related to the fall velocity (hence sediment diameter) (Dean, 1977). Other analytical formulas exist, such as those by Larson et al. (2004) or van Rijn (2009) and these may be more adequate if a dune system is present, although calibration data is needed. Profile measurements to determine these parameters are advised. Moreover, if working on a more data-rich environment and more computational power is available (cluster), Callaghan et al. (2013) advises to replace the analytical formula with a semi-empirical model, such as *SBEACH*. This will however increase the computational time with a factor ~40.

Further, it is advised to check the erosion estimates with data on shoreline positions. This can be taken from in-situ measurements or satellite derived shoreline positions (Luijendijk et al., 2018). The shoreline data (if long enough) can also be useful for determining the seasonal and interannual variability and trends. Directly linked to this is knowing the larger sediment budget. Therefore, application to an open sandy coastline is generally harder.

In summary, a first order magnitude model can be readily obtained using parameters available in many areas, including data-scarce environments. Assuming that the local coastal setting does not have a difficult geometry (e.g. no barrier islands) and other terms in the overall sediment budget are not too dominant, an analytical storm erosion model is practical and defensible. However, to fully validate the model, additional data is a necessity. To illustrate, running the stochastic model for six SLR scenarios on a standard 8GB ram PC takes around 2.5 days under a sample size 10,000 synthetic storm time series of 95 years duration. This makes it very cost-efficient and easily extendible to larger scale areas if working on a cluster.

8

Conclusions

The aim of this research was to quantify how SLR evolves under different scenarios of mass loss from the Antarctic Ice Sheet in the Caribbean area and how this affects future erosion risk for a case study for Sint Maarten. A methodology was described that incorporates plausible future trajectories of SLR with SSTS that were derived based on the observed multi-variate storm parameters and their interdependency. 10,000 potential future combinations are sampled and fed into an erosion model to predict the shoreline from 2006-2100. The probability range of future storm erosion impact and long-term recession could be estimated from this. Three different case of SLR are considered; one estimate consistent with the latest IPCC report, one estimating a skewed distribution function of AIS mass loss, and a high-end scenario of mass loss that includes positive feedback processes. These scenarios were compared and contrasted, and the implications for strategies to manage coastal evaluated.

RSLR projections for Sint Maarten are found particularly sensitive to increased mass loss from the AIS that weight heavily to the total RSLR. Median projections are range from 54-108 cm (73-200 cm) for RCP4.5 (RCP8.5) under IPCC-DP16. Considering additional model uncertainty, due to known common biases in climate models, further increases the uncertainty bandwidth. Before 2070, SLR has only a moderate effect on the enhanced episodic erosion from storms, because amplified storm surges by SLR are not a dominating over other storm parameters. However, after 2070, the SLR projections will drive storm erosion events and results diverge for different scenarios of SLR. The median 1/100 year event of retreat distance from storm impact over 2006-2100 is estimated to be 1.4-2.4 times higher than the baseline scenario without SLR. Long term recession due to the inability to recover between storm events, that are getting gradually more extremer due to SLR, will drive a median net erosion of 5-22 m. In general, including rapid ice sheet dynamics results in significant larger erosion risk. A 1/100 year retreat distance by considering the IPCC projections corresponds to a 1/80 (1/50) event for inclusion of skewness and a 1/15 (1/1.5) event for a high-end scenario of AIS loss for RCP4.5 (RCP8.5). In terms of long-term recession, the 1% exceedance probability given the IPCC case compares to a 2-4.5% exceedance probability for the skewed scenario and a 37-88% exceedance probability for the high-end scenario. Besides, similar recession values will occur years earlier under high-end scenario. In general, it is found that risk-averse coastal managers, favouring low exceedance probabilities (and large return periods), will underestimate the relatively risk more if AIS dynamics are not included appropriately.

In conclusion, precluding AIS uncertainty from SLR projections that feed coastal impact assessments may lead to ill-informed decisions to SLR adaptation, alters the cost-efficiency of mitigation measures and potentially leads to intolerable risk faced. Supporting coastal managers with information about deep uncertainty in SLR projections is found imperative to avoid maladaptation to erosion risk.

Bibliography

Aagaard, T., B. Greenwood, and M. Hughes (2013, sep). Sediment transport on dissipative, intermediate and reflective beaches. *Earth-Science Reviews 124*, 32–50.

Almeida, L. P., O. Ferreira, and R. Taborda (2011). Geoprocessing tool to model beach erosion due to storms: application to Faro beach (Portugal). *Journal Of Coastal Research 64*, 1830–1834.

Alvera-Azcárate, A., A. Barth, and R. H. Weisberg (2009, mar). The Surface Circulation of the Caribbean Sea and the Gulf of Mexico as Inferred from Satellite Altimetry. *Journal of Physical Oceanography 39*(3), 640–657.

Anderson, T. R., C. H. Fletcher, M. M. Barbee, L. N. Frazer, and B. M. Romine (2015). Doubling of coastal erosion under rising sea level by mid-century in Hawaii. *Natural Hazards 78*(1), 75–103.

Annan, J. and J. Hargreaves (2010). Reliability of the cmip3 ensemble. *Geophysical Research Letters 37*(L02703), 1–5.

Appendini, C., A. Torres-Freyermuth, P. Salles, J. Lopen-Gonzalez, and E. Mendoza (2014). Wave climate and trends for the gulf of mexico: a 30-yr wave hindcast. *American Meteoreological Society 27*, 1619 –1633.

Bachmann, R. (2011). The caribbean plate and the question of its formation. Technical report, Institute of Geology, University of Mining and Technology Freiberg, Department of Tectonophysics.

Bakker, A., T. Wong, K. L. Ruckert, and K. Keller (2017). Sea-level projections representing the deeply uncertain contribution of the west antarctic ice sheet. *Scientific Reports 7*(3880), 1–7.

Bakker, A. M., D. Louchard, and K. Keller (2017). Sources and implications of deep uncertainties surrounding sea-level projections. *Climatic Change 140*(3-4), 339–347.

Bamber, J. and W. Aspinall (2013). An expert judgement assessment of future sea level rise from the ice sheets. *Nature Climate Change 3*, 424–428.

Baron, H., P. Ruggiero, N. Wood, E. Harris, J. Alla, P. Komar, and P. Corcoran (2015). Incorporating climate change and morphological uncertainty into coastal change hazard assessments. *Natural Hazards 75*, 2081–2102.

Battjes, J. (1974). Surf similarity. In *Proceedings 14th International Conference on Coastal Engineering*, pp. 466–480.

Boon, J. and M. O. Green (1988). Caribbean beach-face slopes and beach equilibrium profiles. *Journal of Coastal Engineering 120*, 1618–1630.

Bowman, D., J. Guillen, L. Lopez, and V. Pellegrino (2009). Planview geometry and morphological characteristics of pocket beaches on the catalan coast (spain). *Geomorphology 108*(3-4), 191–199.

Brunnabend, S., H. Dijkstra, M. Kliphuis, H. Bal, F. Seinstra, B. van Werkhoven, J. Massen, and M. van Meersbergen (2017). Changes in extreme regional sea level under global warming. *Ocean Science 13*, 47–60.

Bruun, P. (1954). Coast erosion and the development of beach profiles', beach erosion board technical memorandum. Technical report, U.S. Army Engineer Waterways Experiment Station. Vicksburg, MS.

Bruun, P. (1962). Sea level rise as a cause of shore erosion. *Journal of Waterway, Port and Coastal and Ocean Engineering, American Society of Civil Engineers 88*, 117–130.

Buchanan, M., M. Oppenheimer, and R. Kopp (2017). Amplification of flood frequencies with local sea level rise and emerging flood regimes. *Environmental Research Letters 12*(064009), 1–7.

Callaghan, D., P. Nielson, A. Short, and R. Ranasinghe (2008). Statistical simulation of wave climate and extreme beach erosion. *Coastal Engineering 55*, 375–390.

Callaghan, D. P., R. Ranasinghe, and D. Roelvink (2013). Probabilistic estimation of storm erosion using analytical, semi-empirical, and process based storm erosion models. *Coastal Engineering 82*, 64–75.

Cambers, G. (2005). *Encyclopedia of Coastal Science*, Chapter Caribbean Islands, Coastal Ecology and Geomorphology. Springer Netherlands.

Carrère, L. and F. Lyard (2003). Modeling the barotropic response of the global ocean to atmospheric wind and pressure forcing - Comparisons with observations. *Geophysical Research Letters 30*(6), 1997–2000.

Carrere, L., F. Lyard, M. Cancet, and A. Guillot (2015). FES 2014, a new tidal model on the global ocean with enhanced accuracy in shallow seas and in the Arctic region. *EGU General Assembly Conference Abstracts 17*, 5481.

Carson, M., A. Kohl, D. Stammer, A. Slangen, C. Katsman, R. van de Wal, J. Church, and N. White (2016). Coastal sea level changes, observed and projected during the 20th and 21st century. *Climatic Change 134*, 269–281.

Carton, J. A. and Y. Chao (1999, apr). Caribbean Sea eddies inferred from TOPEX/POSEIDON altimetry and a 1/6° Atlantic Ocean model simulation. *Journal of Geophysical Research: Oceans 104*(C4), 7743–7752.

Chen, X., X. Zhang, J. Church, C. Watson, M. King, D. Monselesan, B. Legresy, and C. Harig (2017). The increasing rate of global mean sea-level rise during 1993–2014. *Nature Climate Change 7*, 492–495.

Church, J., P. Clark, A. Cazenave, J. Gregory, S. Jevrejeva, A. Levermann, M. Merrifield, G. Milne, R. Nerem, P. Nunn, A. Payne, W. Pfeffer, D. Stammer, and A. Unnikrishan (2013). Sea level change. in: Climate change 2013: The physical science basis. contribution of working group i

to the fifth assessment report of the intergovernmental panel on climate change. Technical report, Cambridge University Press, Cambridge, United Kingdom and New York, NY, USA.

Cooper, J. and O. Pilkey (2004). Sea-level rise and shoreline retreat: time to abandon the bruun rule. *Global and Planetary change 43*, 157–171.

Cowell, P. J., B. G. Thom, R. A. Jones, C. H. Everts, and D. Simanovic (2006). Management of Uncertainty in Predicting Climate-Change Impacts on Beaches. *Journal of Coastal Research 221*, 232–245.

Dangendorf, S., M. Marcos, G. Woppelmann, C. Conrad, T. Frederikse, and R. Riva (2017). Reassessment of 20th century global mean sea level rise. *PNAS 114*(23), 5946–5951.

Davidson, M. A., K. D. Splinter, and I. L. Turner (2013). A simple equilibrium model for predicting shoreline change. *Coastal Engineering 73*, 191–202.

Davies, G., D. P. Callaghan, U. Gravios, W. Jiang, D. Hanslow, S. Nichol, and T. Baldock (2017). Improved treatment of non-stationary conditions and uncertainties in probabilistic models of storm wave climate. *Coastal Engineering 127*(June), 1–19.

De Michele, C., G. Salvadori, G. Passoni, and R. Vezzoli (2007). A multivariate model of sea storms using copulas. *Coastal Engineering 54*(10), 734–751.

de Vries, H., C. Katsman, and S. Drijfhout (2014). Constructing scenarios of regional sea level change using global temperature pathways. *Environmental Research Letters 9*(115007), 1–8.

de Vries, H. and R. van de Wal (2015). How to interpret expert judgment assessments of 21st century sea-level rise. *Climatic Change 130*(2), 87–100.

de Waal, D. and P. van Gelder (2005). Modelling of extreme wave heights and periods through copulas. *Extremes 8*, 345–356.

de Winter, R., T. Reerink, A. Slangen, H. Vires, T. Edwards, and R. van de Wal (2017). Impact of asymmetric uncertainties in ice sheet dynamics on regional sea level projections. *Natural Hazards and Eart System Sciences 17*, 2125–2141.

Dean, R. (1977). Equilibrium beach profiles: U.s. antlantic and gulf coast. ocean engineering tech. rpt. no. 12. Technical report, Department of Civil Engineering and College of Marine Studies, University of Delaware.

Dean, R. (1987). Coastal sediment processes: Toward engineering solutions. In *Specialty Conference on Coastal Sediment 87*.

Dean, R. and R. Dalrymple (2001). *Coastal processes with engineering applications*. Cambridge: Cambridge University Press.

Dean, R. and J. Houston (2016). Determining shoreline response to sea level rise. *Coastal Engineering 114*, 1–8.

DeConto, R. M. and D. Pollard (2016, mar). Contribution of Antarctica to past and future sea-level rise. *Nature 531*(7596), 591–597.

Dee, D., S. Uppala, A. Simmonds, P. Berrisford, P. Poli, S. Kobayashi, U. Andrae, and et al. (2011). The era-interim reanalysis: configuration and performance of the data assimilation system. *Quarterly journal of the Royal Meteorological Society 137*, 553–597.

Department of Statistics (2017). Statistical yearbook 2017. Technical report, Department of Statistics, Sint Maarten.

Devis-Morales, A., R. Montoya-Sanchez, G. Bernal, and A. Osorio (2017). Assessment of extreme wind and waves in the colombian caribbeansea for offshore applications. *Applied Ocean Research 69*, 10–26.

Dieng, H. B., A. Cazenave, B. Meyssignac, and M. Ablain (2017). New estimate of the current rate of sea level rise from a sea level budget approach. *Geophysical Research Letters 44*(8), 3744–3751.

Favier, L., G. Durand, S. L. Cornford, G. H. Gudmundsson, O. Gagliardini, F. Gillet-Chaulet, T. Zwinger, A. J. Payne, and A. M. Le Brocq (2014, feb). Retreat of Pine Island Glacier controlled by marine ice-sheet instability. *Nature Climate Change 4*(2), 117–121.

Fettweis, X., B. Franco, M. Tedesco, J. van Angelen, J. Lenaerts, M. R. van den Broeke, and H. Gallee (2013). Estimating the greenland ice sheet surface mass balance contribution to future sea level rise using the regional atmospheric climate model mar. *The Cryosphere 7*, 469–489.

Fish, M., I. M. Cote, J. Gill, A. Jones, S. Renshoff, and A. Watkinson (2005). Predicting the impact of sea-level rise on caribbean sea turtle nesting habitat. *Conservation Biology 19*(2), 482–491.

FitzGerald, D., M. Fenster, and B. A. andI.V. Buynevich (2008). Coastal impacts due to sea-level rise. *Annual Review of Earth and Planetary Sciences 36*, 601–647.

Fuller, R. W., T. E. Wong, and K. Keller (2017). Probabilistic inversion of expert assessments to inform projections about Antarctic ice sheet responses. *PLoS ONE 12*(12), 6–9.

Genest, C., B. Rémillard, and D. Beaudoin (2009). Goodness-of-fit tests for copulas: A review and a power study. *Insurance: Mathematics and Economics 44*(2), 199–213.

Giesen, R. and J. Oerlemans (2013). Climate-model induced differences in the 21st century global and regional glaciers contributions to sea-level rise. *Climate Dynamics 41*(11-12), 3283–3300.

Golledge, N., D. Kowalewski, T. Naish, R. Levy, C. Fogwill, and E. Gasson (2015). The multi-millennial antarctic commitment to future sea-level rise. *Nature 526*, 421–439.

Gregory, J. and P. Huybrechts (2006). Ice-sheet contributions to future sea-level change. *Philosophical Transactions of the Royal Society 364*, 1709–1731.

Haasnoot, M., J. H. Kwakkel, W. E. Walker, and J. ter Maat (2013, apr). Dynamic adaptive policy pathways: A method for crafting robust decisions for a deeply uncertain world. *Global Environmental Change 23*(2), 485–498.

Hagenaars, G., S. de Vries, A. P. Luijendijk, W. P. de Boer, and A. J. Reniers (2018). On the accuracy of automated shoreline detection derived from satellite imagery: A case study of the sand motor mega-scale nourishment. *Coastal Engineering 133*(June 2017), 113–125.

Hallegatte, S., C. Green, R. J. Nicholls, and J. Corfee-Morlot (2013, aug). Future flood losses in major coastal cities. *Nature Climate Change 3*(9), 802–806.

Hanson, H., S. Aarninkhof, M. Capobianco, J. A. Jiménez, M. Larson, R. J. Nicholls, N. G. Plant, H. N. Southgate, H. J. Steetzel, M. J. F. Stive, and H. J. de Vriend (2003). Modelling of Coastal Evolution on Yearly to Decadal Time Scales. *Journal of Coastal Research 19*(4), 790.

Hay, C., E. Morrow, R. Kopp, and J. Mitrovica (2015). Probabilistic reanalysis of twentieth-century sea-level rise. *Nature 517*, 481–494.

Hemer, M., Y. Fan, N. Mori, A. Semedo, and X. Wang (2013). Projected changes in wave climate from a multi-model ensemble. *Nature Climate Change 3*, 471–476.

Hinkel, J., C. Jaeger, R. Nicholls, J. Lowe, O. Renn, and S. Reijun (2015). Sea-level rise scenarios and coastal risk management. *Nature Climate Change 5*, 188–191.

Hinkel, J., R. Nicholls, R. Tol, Z. Wang, J. Hamilton, G. Boot, A. Vafeidis, L. McFadden, A. Ganopolski, and R. Klein (2013). A global analysis of erosion of sandy beaches and sea level rise: an application of diva. *Global and Planetary Change 111*, 150–158.

Hof, A. F., D. P. van Vuuren, and M. G. den Elzen (2010, nov). A quantitative minimax regret approach to climate change: Does discounting still matter? *Ecological Economics 70*(1), 43–51.

Horton, B. P., S. Rahmstorf, S. E. Engelhart, and A. C. Kemp (2014, jan). Expert assessment of sea-level rise by AD 2100 and AD 2300. *Quaternary Science Reviews 84*, 1–6.

Hsu, C. and I. Velicogna (2017). Detection of sea level fingerprints derived from grace gravity data. *Environmental Research Letters 44*, 8953—8961.

Hu, A. and S. C. Bates (2018). Internal climate variability and projected future regional steric and dynamic sea level rise /704/106/829/2737 /639/766 /139 article. *Nature Communications 9*(1), 1–11.

Huss, M. and R. Hock (2015). A new model for global glacier change and sea-level rise. *Frontiers in Earth's Sciences 3*(54), 1–22.

IMBIE team (2018, jun). Mass balance of the Antarctic Ice Sheet from 1992 to 2017. *Nature 558*(7709), 219–222.

Jackson, L. and S. Jevrejeva (2016). A probabilistic approach to 21st century regional sea-level projections using rcp and high-end scenarios. *Global and Planetary Changes 146*, 179–189.

Jevrejeva, S., A. Grinsted, and J. Moore (2014). Upper limit for sea level projections by 2100. *Environmental Research Letters 9*(104008), 1–9.

Jevrejeva, S., L. Jackson, R. Riva, A. Grinsted, and J. Moore (2016). Coastal sea level rise with warming above 2 °c. *PNAS 113*(47), 13342 –13347.

Joe, H. (2014). *Dependence Modeling with Copulas*. London: CRC Press Taylor and Francis Group.

Jongejan, R., R. Ranasinghe, D. Wainwright, D. Callaghan, and J. Reyns (2016). Drawing the line on coastline recession risk. *Ocean and Coastal Management 122*, 87–94.

Jongejan, R. B., R. Ranasinghe, J. K. Vrijling, and D. Callaghan (2011, jan). A risk-informed approach to coastal zone management. *Australian Journal of Civil Engineering 9*(1), 47–60.

Jouanno, J. and J. Sheinbaum (2013). Heat Balance and Eddies in the Caribbean Upwelling System. *Journal of Physical Oceanography 43*(5), 1004–1014.

Joughin, I., B. E. Smith, and B. Medley (2014, may). Marine Ice Sheet Collapse Potentially Under Way for the Thwaites Glacier Basin, West Antarctica. *Science 344*(6185), 735–738.

Jury, M. (2018). Characteristics and meteorology of atlantic swells reaching the caribbean. *Journal of Coastal Research 34*(2), 400–412.

Karmalkar, A., M. Taylor, J. Campbell, T. Stephenson, M. N. nd A. Centella, A. Benzanilla, and J. Carlery (2013). A review of observed and projected changes in climate for the islands in the caribbean. *Atmosfera 26*, 283–309.

Khan, N., E. Ashe, B. Horton, A. Dutton, R. Kopp, G. Brocard, S. Engelhart, D. Hill, W. Peltier, C. Vane, and F. Scatena (2017). Drivers of holocene sea level change in the caribbean. *Quaternary Science Reviews 107*, 119–131.

Kind, J., W. Wouter Botzen, and J. C. Aerts (2017, mar). Accounting for risk aversion, income distribution and social welfare in cost-benefit analysis for flood risk management. *Wiley Interdisciplinary Reviews: Climate Change 8*(2), e446.

Kjerfve, B. (1981). Tides of the caribbean. *Journal of Geophysical Research 86*(C5), 4243–4247.

Klein, R. J. T., R. J. Nicholls, S. Ragoonaden, M. Capobianco, J. Aston, and E. N. Buckley (2001). Technological options for adaptation to climate change in coastal zones. *Journal of Coastal Research 17*(3), 531–543.

Kohsiek, L., C. Hulsbergen, and J. Terwindt (1987). Beach erosion along the west coast of aruba, netherlands antilles. *Journal of Coastal Research 3*(1), 37 –53.

Kopp, R., R. DeConto, D. Bader, C. Hay, R. Horton, S. Kulp, M. Oppenheimer, and D. Pollard (2017). Evolving understanding of antarctic ice-sheet physics and ambiguity in probabilistic sea-level projections. *Earth's Future 5*, 1–17.

Kopp, R., C. Hay, C. Little, and J. Mitrovica (2015). Geographic variability of sea-level change. *Current Climate Change Reports 1*, 192–204.

Kopp, R., R. Horton, C. Little, J. Mitrovica, M. Oppenheimer, D. Rasmussen, B. Strauss, and C. Tebaldi (2014). Probabilistic 21st and 22nd century sea-level projections at a global network of tide-gauge sites. *Earth's Future 2*, 383–406.

Kriebel, D. and R. Dean (1993). Convolution method for time-dependent beach-profile response. *Journal of Waterway, Port, Coastal and Ocean Engineering 119*(2), 204–226.

Kuhlbrodt, T. and J. M. Gregory (2012, sep). Ocean heat uptake and its consequences for the magnitude of sea level rise and climate change. *Geophysical Research Letters 39*(18), 1–6.

Kunreuther, H., G. Heal, M. Allen, O. Edenhofer, C. B. Field, and G. Yohe (2013). Risk management and climate change. *Nature Climate Change 3*(5), 447–450.

Large, W. G. and S. Pond (1981). Open Ocean Momentum Flux Measurements in Moderate to Strong Winds. *Journal of Physical Oceanography 11*(3),

324–336.

Larour, E., E. R. Ivins, and S. Adhikari (2017). Should coastal planners have concern over where land ice is melting? *Science Advances 3*(11), 1–9.

Larson, M., L. Erikson, and H. Hanson (2004). An analytical model to predict dune erosion due to wave impact. *Coastal Engineering 51*, 675–696.

Larson, M., L. Hoan, and H. Hanson (2010). Direct formula to compute wave height and angle at incipient breaking. *JOURNAL OF WATERWAY, PORT, COASTAL, AND OCEAN ENGINEERING 136*(2), 119–122.

Larson, M. and N. Kraus (1989). Sbeach: Numerical model to simulate storm-induced beach change. Technical report, U.S. Army Corps of Engineers Technical Report, CERC.

Lazarus, E. D., D. E. McNamara, M. D. Smith, S. Gopalakrishnan, and A. B. Murray (2011). Emergent behavior in a coupled economic and coastline model for beach nourishment. *Nonlinear Processes in Geophysics 18*(6), 989–999.

Le Bars, D. (2018). Uncertainty in sea level rise projections due to the dependence between contributors. *Earth's Future under review*.

Le Bars, D., S. Drijfhout, and H. de Vries (2017). A high-end sea level rise probabilitic projection including rapid antarctic ice sheet mass loss. *Environmental Research Letters 12*(044013), 1–10.

Le Cozannet, G., J. Manceau, and J. Rohmer (2017). Bounding probabilistic sea-level projections within the framework of the possibility theory. *Environmental Research Letters 12*(014012), 1–11.

Le Cozannet, G., J. Rohmer, A. Cazenave, D. Idier, R. van de Wal, R. de Winter, R. Pedreros, Y. Balouin, C. Vinchon, and C. Oliveros (2015, nov). Evaluating uncertainties of future marine flooding occurrence as sea-level rises. *Environmental Modelling & Software 73*, 44–56.

Lempert, R. J. and M. T. Collins (2007). Managing the risk of uncertain threshold responses: Comparison of robust, optimum, and precautionary approaches. *Risk Analysis 27*(4), 1009–1026.

Lenaerts, J., M. Vizcaino, J. Fyke, L. van Kampenhout, and M. R. van de Broeke (2016). Present□day and future antarctic ice sheet climate and surface mass balance in the community earth system model. *Climate Dynamics 47*, 1367–1381.

Lentz, E. E., E. R. Thieler, N. G. Plant, S. R. Stippa, R. M. Horton, and D. B. Gesch (2016). Evaluation of dynamic coastal response to sea-level rise modifies inundation likelihood. *Nature Climate Change 6*(7), 696–700.

Levermann, A., P. Clark, B. Marzeion, G. Milne, D. Pollard, V. Radic, and A. Robinson (2013). The multimillennial sea-level commitment of global warming. *PNAS 110*(34), 13745–13750.

Levermann, A., R. Winkelmann, S. Nowicki, J. Fastook, K. Frieler, R. Greve, H. Helmer, M. Martin, M. Meinshausen, M. Mengel, A. Payne, D. Pollard, T. Sato, R. Timmermann, W. Wang, and R. Bindschadler (2014). Projecting antarctic ice discharge using response functions from searise ice-sheet models. *Earth System Dynamics 5*, 271–293.

Li, F., P. van Gelder, R. Ranasinghe, D. Callaghan, and R. Jongejan (2014, apr). Probabilistic modelling of extreme storms along the Dutch coast. *Coastal Engineering 86*, 1–13.

Li, F., P. van Gelder, J. Vrijling, D. Callaghan, R. Jongejan, and R. Ranasinghe (2014, aug). Probabilistic estimation of coastal dune erosion and recession by statistical simulation of storm events. *Applied Ocean Research 47*, 53–62.

Li, J., W. Tan, M. Chen, J. Zuo, and Y. Yang (2016). The regional patterns of the global dynamic and steric sea level variation in twenty-first century projections. *Global and Planetary Change 146*, 133–139.

Ligtenberg, S., W. van de Berg, M. van den Broeke, J. Rae, and E. van Meijgaard (2013). Future surface mass balance of the antarctic ice sheet and its influence on sea level change, simulated by a regional atmospheric climate model. *Climate Dynamics 41*, 867–884.

Little, C., N. Urban, and M. Oppenheimer (2013). Probabilistic framework for assessing the ice sheet contribution to sea level change. *PNAS 110*(9), 3264–3269.

Losada, I., B. Reguero, F. Mendez, S. Castanedo, A. Abascal, and R. Minguez (2013). Long-term changes in sea-level components in latin america and the caribbean. *Global and Planetary Change 104*, 34–50.

Luijendijk, A., G. Hagenaars, R. Ranasinghe, F. Baart, G. Donchyts, and S. Aarninkhof (2018). The state of the world's beaches. *Scientific Reports 8*(6641), 1–11.

Magnan, A. K., E. L. Schipper, M. Burkett, S. Bharwani, I. Burton, S. Eriksen, F. Gemenne, J. Schaar, and G. Ziervogel (2016). Addressing the risk of maladaptation to climate change. *Wiley Interdisciplinary Reviews: Climate Change 7*(5), 646–665.

Maraun, D., T. G. Shepherd, M. Widmann, G. Zappa, D. Walton, J. M. Gutiérrez, S. Hagemann, I. Richter, P. M. Soares, A. Hall, and L. O. Mearns (2017). Towards process-informed bias correction of climate change simulations. *Nature Climate Change 7*(11), 764–773.

Marzeion, B., A. Jarosch, and M. Hofer (2012). Past and future sea-level change from the surface mass balance of glaciers. *The Cryosphere 6*, 1295–1322.

McGranahan, G., D. Balk, and B. Anderson (2007). The rising tide: assessing the risks of climate change and human settlements in low elevation coastal zones. *Environment and Urbanization 19*(1), 17–37.

McKee, K. (2011). Biophysical controls on accretion and elevation change in caribbean mangrove ecosystems. *Estuarine, Coastal and Shelf Science 4*, 475–483.

Melet, A., B. Meyssignac, R. Almar, and G. L. Cozannet (2018). Under-estimated wave contribution to coastal sea-level rise. *Nature Climate Change 8*, 234–239.

Mengel, M., A. Levermann, K. Frieler, A. Robinson, B. Marzeion, and R. Winkelmann (2016). Future sea level rise constrained by observations and long-term commitment. *Proceedings of the National Academy of Sciences 113*(10), 2597–2602.

Mengel, M., A. Nauels, J. Rogelj, and C. Schleussnes (2018). Committed sea-level rise under the paris agreement and the legacy of delayed mitigation

action. *Nature Communications 9*(601), 1–10.

Meyssignac, B., X. Fettweis, R. Chevrier, and G. Spada (2016). Regional sea level changes for the twentieth and the twenty-first centuries induced by the regional variability in greenland ice sheet surface mass loss. *Climate Dynamics 30*, 2011–2029.

Miller, J. and R. Dean (2004). A simple new shoreline change model. *Coastal Engineering 51*, 531–556.

Milne, G. and M. Peros (2013). Data-model comparison of holocene sea-level change in the circum-caribbean region. *Global and Planetary Change 107*, 119–131.

Mimura, N., R. M. L. Nurse, J. Agard, L. Briguglio, P. Lefale, R. Payet, and G. Sem (2007). Small islands. Technical report, Climate Change 2007: Impacts, Adaptation and Vulnerability. Contribution of Working Group II to the Fourth Assessment Report of the Intergovernmental Panel on Climate Change, Cambridge University Press, Cambridge, UK.

Misra, A., Z. Vojinovic, B. Ramakrishnan, A. Luijendijk, and R. Ranasinghe (2018, jan). Shallow water bathymetry mapping using Support Vector Machine (SVM) technique and multispectral imagery. *International Journal of Remote Sensing 00*(00), 1–20.

Mitrovica, J., N. Gomez, E. Morrow, C. Hay, K. Latychev, and M. Tamisiea (2011). On the robustness of predictions of sea level fingerprints. *Geophysical Journal International 187*, 729–742.

Morales-Nápoles, O., D. Paprotny, D. Worm, L. Abspoel-Bukman, and W. Courage (2017). Characterization of Precipitation through Copulas and Expert Judgement for Risk Assessment of Infrastructure. *3*, 1–13.

Mueller, N. and C. Meindl (2017). Vulnerability of caribbean island cemeteries to sea level rise and storm surge. *Coastal Management 45*(4), 277–292.

Mull, J. and P. Ruggiero (2014). Estimating storm-induced dune erosion and overtopping along u.s. west coast beaches. *Journal of Coastal Research 30*(6), 1173–1187.

Munk, W. H. (1949). Surf beats. *Transaction American Geophysical Union 30*(6).

Nerem, R., B. Beckley, J. Fasullo, B. Hamlington, D. Masters, and G. Mitchum (2018). Climate-change–driven accelerated sea-level rise detected in the altimeter era. *PNAS Latest Articles*, 1–4.

Nicholls, R. and A. Cazenave (2010). Sea-level rise and its impact on the coastal zone. *Science 328*, 1517–1520.

Oerlemans, J. and J. Fortuin (1992). Sensitivity of glaciers and small ice caps to greenhouse warming. *Science 258*, 115–116.

Oppenheimer, M. and R. Alley (2016). How high will the seas rise? *Science 354*(6318), 1375–1376.

Oppenheimer, M., C. M. Little, and R. M. Cooke (2016). Expert judgement and uncertainty quantification for climate change. *Nature Climate Change 6*(5), 445–451.

Palanisamy, H., M.Becker, B. Meyssignac, O. Henry, and A. Cazenave (2012). Regional sea level change and variability in the caribbean sea since 1950. *Journal of Geodetic Science 2*(2), 125–133.

Palerme, C., C. Genthon, C. Claud, J. Kay, N. Wood, and T. L'Ecuyer (2017). Evaluation of current and projected antarctic precipitation in cmip5 models. *Climate Dynamics 48*, 225–239.

Parkinson, R., R. DeLaune, and J. White (1994). Holocene sea-level rise and the fate of mangrove forests within the wider caribbean region. *Journal of Coastal Research 10*(4), 1077–1086.

Pattyn, F. (2018, dec). The paradigm shift in Antarctic ice sheet modelling. *Nature Communications 9*(1), 2728.

Pelling, M. and J. I. Uitto (2001). Small island developing states: Natural disaster vulnerability and global change. *3*(2), 49–62.

Peltier, W. (2000). Earth physics and global glacial isostasy: From paleo-geodesy to space geodesy. In *International Association of Geodesy Symposia; Gravity, Geoid and Geodynamics*.

Perry, C. T., L. Alvarez-Filip, N. A. J. Graham, P. J. Mumby, S. K. Wilson, P. S. Kench, D. P. Manzello, K. M. Morgan, A. B. A. Slangen, D. P. Thomson, F. Januchowski-Hartley, S. G. Smithers, R. S. Steneck, R. Carlton, E. N. Edinger, I. C. Enochs, N. Estrada-Saldívar, M. D. E. Haywood, G. Kolodziej, G. N. Murphy, E. Pérez-Cervantes, A. Suchley, L. Valentino, R. Boenish, M. Wilson, and C. Macdonald (2018, jun). Loss of coral reef growth capacity to track future increases in sea level. *Nature 558*(7710), 396–400.

Phillips, M. S., M. D. Harley, I. L. Turner, K. D. Splinter, and R. J. Cox (2017). Shoreline recovery on wave-dominated sandy coastlines: the role of sandbar morphodynamics and nearshore wave parameters. *Marine Geology 385*, 146–159.

Pollard, D., R. M. DeConto, and R. B. Alley (2015). Potential Antarctic Ice Sheet retreat driven by hydrofracturing and ice cliff failure. *Earth and Planetary Science Letters 412*, 112–121.

Quartly, G., J. Legeais, M. Ablain, L.Zawadzki, J. Fernandes, S. Rudenko, L. Carrere, and et al. (2017). A new phase in the production of quality-controlled sea level data. *Earth System Science Data 9*, 557 –572.

Radic, V., A. Bliss, A. Beedlow, R. Hock, E. Miles, and J. Cogley (2014). Regional and global projections of twenty-first century glacier mass changes in response to climate scenarios from global climate models. *Climate Dynamics 42*, 37–58.

Rahmstorf, S. (2007). Projecting twenty-first century regional sea-level changes. *Science 315*, 368–372.

Ranasinghe, R. (2016). Assessing climate change impacts on open sandy coasts: A review. *Earth-Science Reviews 160*, 320–332.

Ranasinghe, R., D. Callaghan, and M. Stive (2012). Estimating coastal recession due to sea level rise: beyond the bruun rule. *Climatic Change 110*, 561–574.

Ranasinghe, R. and M. J. F. Stive (2009, dec). Rising seas and retreating coastlines. *Climatic Change 97*(3-4), 465–468.

Reguero, B., I. Losada, P. Diaz-Simal, F. Mendez, and M. Beck (2015). Effects of climate change on exposure to coastal flooding in latin america and the caribbean. *PLoS ONE 10*(7), 1–19.

Reguero, B., F. Mendez, and I. Losada (2013). Variability of multivariate wave climate in latin america and the caribbean. *Global and Planetary Change 100*, 70–84.

Rignot, E. J. (1998, jul). Fast Recession of a West Antarctic Glacier. *Science 281*(5376), 549–551.

Ritz, C., T. Edwards, G. Durand, A. Payne, V. Peyaud, and H. R.C.A (2015). Potential sea-level rise from antarctic ice-sheet instability constrained by observations. *Nature 528*, 115–129.

Robinet, A., B. Castelle, D. Idier, G. Le Cozannet, M. Déqué, and E. Charles (2016). Statistical modeling of interannual shoreline change driven by North Atlantic climate variability spanning 2000–2014 in the Bay of Biscay. *Geo-Marine Letters 36*(6), 479–490.

Roelvink, D., A. Reniers, A. van Dongeren, J. van Thiel de Vries, R. McCall, and J. Lescinki (2009). Modelling storm impacts on beaches, dunes and barrier islands. *Coastal Engineering 56*, 1133–1152.

Rosati, J., R. Dean, and T. Walton (2013). The modified bruun rule extended for landward transport. *Marine Geology 340*, 71–81.

Salvadori, G., G. Tomasicchio, and F. D'Alessandro (2014, jun). Practical guidelines for multivariate analysis and design in coastal and off-shore engineering. *Coastal Engineering 88*, 1–14.

Santamaria-Gomez, A., M. Gravelle, S. Dangendorf, M. Marcos, G. Spada, and G. Woppelmann (2017). Uncertainty of the 20th century sea-level rise due to vertical land motion errors. *Earth and Planetary Science Letters 473*, 24 –32.

Schlegel, N.-j., H. Seroussi, M. P. Schodlok, E. Y. Larour, C. Boening, D. Limonadi, M. M. Watkins, M. Morlighem, and M. R. V. D. Broeke (2018, jun). Exploration of Antarctic Ice Sheet 100-year contribution to sea level rise and associated model uncertainties using the ISSM framework. *The Cryosphere Discussions* (June), 1–36.

Scott, D., M. C. Simpson, and R. Sim (2012). The vulnerability of caribbean coastal tourism to scenarios of climate change related sea level rise. *Journal of Sustainable Tourism 20*(6), 883–898.

Scott, T., G. Masselink, T. O'Hare, A. Saulter, T. Poate, P. Russell, M. Davidson, and D. Conley (2016). The extreme 2013/2014 winter storms: Beach recovery along the southwest coast of England. *Marine Geology 382*, 224–241.

Semedo, A., K. SušElj, A. Rutgersson, and A. Sterl (2011). A global view on the wind sea and swell climate and variability from ERA-40. *Journal of Climate 24*(5), 1461–1479.

Sérazin, G., B. Meyssignac, T. Penduff, L. Terray, B. Barnier, and J. M. Molines (2016). Quantifying uncertainties on regional sea level change induced by multidecadal intrinsic oceanic variability. *Geophysical Research Letters 43*(15), 8151–8159.

Simpson, M., D. Scott, M. Harrison, R. Sim, N. Silver, E. O'Keeffe, S. Harrison, M. Taylor, G. Lizcano, M. Rutty, H. Stager, J. Oldham, M. Wilson, M. New, J. Clarke, O. Day, N. Fields, J. Georges, R. Waithe, and P. McSharry (2010). Quantification and magnitude of losses and damages resulting from the impacts of climate change: Modelling the transformational impacts and costs of sea level rise in the caribbean (full document. Technical report, United Nations Development Programme (UNDP), Barbados, West Indies.

Slangen, A., M. Carson, C. Katsman, R. van der Wal, A. Kohl, L. Vermeersen, and D.Stammer (2014). Projecting twenty-first century regional sea-level changes. *Climatic Change 124*(1-2), 317–332.

Slangen, A., J. Church, C. Agosta, X. Fettweis, B. Marzeion, and K. Richter (2016). Anthropogenic forcing dominates global mean sea-level rise since 1970. *Nature Climate Change 6*, 701–708.

Slangen, A. and R. van der Wal (2011). Anthropogenic forcing dominates global mean sea-level rise since 1970. *Cryosphere 5*, 673–686.

Slangen, A. B. A., C. A. Katsman, R. S. W. van de Wal, L. L. A. Vermeersen, and R. E. M. Riva (2012, mar). Towards regional projections of twenty-first century sea-level change based on IPCC SRES scenarios. *Climate Dynamics 38*(5-6), 1191–1209.

Splinter, K. D., I. L. Turner, M. A. Davidson, P. Barnard, B. Castelle, and J. Oltman-Shay (2014). A generalized equilibrium model for predicting daily to inter-annual shoreline response A generalized equilibrium model for predicting daily to inter-annual shoreline response. *Journal of Geophysical Research: Earth Surface 119*, 1936–1958.

Sriver, R. L., R. J. Lempert, P. Wikman-Svahn, and K. Keller (2018, feb). Characterizing uncertain sea-level rise projections to support investment decisions. *PLOS ONE 13*(2), e0190641.

Stive, M. J., S. G. Aarninkhof, L. Hamm, H. Hanson, M. Larson, K. M. Wijnberg, R. J. Nicholls, and M. Capobianco (2002, dec). Variability of shore and shoreline evolution. *Coastal Engineering 47*(2), 211–235.

Stive, M. J., M. A. de Schipper, A. P. Luijendijk, S. G. Aarninkhof, C. van Gelder-Maas, J. S. van Thiel de Vries, S. de Vries, M. Henriquez, S. Marx, and R. Ranasinghe (2013). A New Alternative to Saving Our Beaches from Sea-Level Rise: The Sand Engine. *Journal of Coastal Research 290*(5), 1001–1008.

Stive, M. J. F. (2004, May). How important is global warming for coastal erosion? *Climatic Change 64*(1), 27–39.

Stockdon, H., R. Holman, P. Howd, and A. Sallenger (2006). Empirical parameterization of set-up, swash, and run-up. *Coastal Engineering 53*, 573–588.

Sutton, R. T. (2018). Ideas: a simple proposal to improve the contribution of IPCC WG1 to the assessment and communication of climate change risks. *Earth System Dynamics Discussions* (June), 1–3.

Sweet, W., R. Kopp, C. Weaver, J. Obeysekera, R. Horton, E. Thieler, and C.Zervas (2017). Global and regional sea level rise scenarios for the united states. Technical report, NOAA, U.S. Department of Commerce.

Tebaldi, C., B. H. Strauss, and C. E. Zervas (2012). Modelling sea level rise impacts on storm surges along US coasts. *Environmental Research Letters 7*(1).

Temmerman, S., P. Meire, T. J. Bouma, P. M. J. Herman, T. Ysebaert, and H. J. De Vriend (2013, dec). Ecosystem-based coastal defence in the face

of global change. *Nature 504*(7478), 79–83.

Toimil, A., I. J. Losada, P. Camus, and P. Díaz-Simal (2017, oct). Managing coastal erosion under climate change at the regional scale. *Coastal Engineering 128*(July), 106–122.

Torres, R. and M. Tsimplis (2011). Tides and long□term modulations in the caribbean sea. *Journal of Geophysical Research 116*(C10022), 1–18.

Torres, R. and M. Tsimplis (2013). Sea-level trends and interannual variability in the caribbean sea. *Journal of Geophysical Research: Oceans 118*, 2934–2947.

Trenberth, K. (2005, jun). CLIMATE: Uncertainty in Hurricanes and Global Warming. *Science 308*(5729), 1753–1754.

United Nations (2017). World population prospects: The 2017 revision. Technical report, United Nations, Department of Economic and Social Affairs, Population Division.

Vafeidis, A. T., R. J. Nicholls, L. McFadden, R. S. J. Tol, J. Hinkel, T. Spencer, P. S. Grashoff, G. Boot, and R. J. T. Klein (2008). A New Global Coastal Database for Impact and Vulnerability Analysis to Sea-Level Rise. *Journal of Coastal Research 244*, 917–924.

van den Broeke, M., J. Bamber, J. Ettema, E. Rignot, E. Schrama, W. van de Berg, E. van Meijgaard, I. Velicogna, and B. Wouters (2009). Partitioning recent greenland mass loss. *Science 326*, 984–986.

van den Broeke, M., J. Box, X. Fettweis, E. Hanna, B. Noel, M. Tedesco, D. van As, W. van de Berg, and L. van Kampenhout (2017). Greenland ice sheet surface mass loss: Recent developments in observation and modeling. *Current Climate Changen Response 3*, 345–356.

van Rijn, L. C. (2009, apr). Prediction of dune erosion due to storms. *Coastal Engineering 56*(4), 441–457.

van Vuuren, D., J. Edmonds, M. Kainuma, K. Riahi, A. Thomson, K. Hibbard, G. Hurtt, T. Kram, V. Krey, J. Lamarque, T. Masui, M. Meinshausen, N. Nakicenovic, S. Smith, and S. Rose (2011). The representative concentration pathways: an overview. *Climatic Change 109*, 5–31.

Vandenberghe, S., N. E. Verhoest, and B. De Baets (2010). Fitting bivariate copulas to the dependence structure between storm characteristics: A detailed analysis,basedon 105 year 10 min rainfall. *Water Resources Research 46*(1), 1–17.

Vermeer, M. and S. Rahmstorf (2009). Global sea level linked to global temperature. *PNAS 106*(51), 21527–21532.

Vitousek, S., P. Barnard, C. Fletcher, N. Frazer, L. Erikson, and C. Storlazzi (2017). Doubling of coastal flooding frequency within decades due to sea-level rise. *Scientific Reports 7*(1399), 1–9.

Vousdoukas, M. I., L. Mentaschi, E. Voukouvalas, M. Verlaan, S. Jevrejeva, L. P. Jackson, and L. Feyen (2018). Global probabilistic projections of extreme sea levels show intensification of coastal flood hazard. *Nature Communications 9*(1), 2360.

Wada, Y., L. van Beek, F. Sperna-Weiland, B. Chao, Y. Wu, and M. Bierkens (2012). Past and future contribution of global groundwater depletion to sea-level rise. *Geophysical Research Letters 39*(L09402), 1–6.

Wahl, T., N. Plant, and J. Long (2016). Probabilistic assessment of erosion and flooding risk in the northern gulf of mexico. *Journal of Geophysical Research: Oceans 121*, 3029–3042.

Wahl, T. and N. G. Plant (2015, apr). Changes in erosion and flooding risk due to long-term and cyclic oceanographic trends. *Geophysical Research Letters 42*(8), 2943–2950.

Wang, C., L. Zhang, S. K. Lee, L. Wu, and C. R. Mechoso (2014). A global perspective on CMIP5 climate model biases. *Nature Climate Change 4*(3), 201–205.

Wong, T., A. Bakker, and K. Keller (2017). Impacts of antarctic fast dynamics on sea-level projections and coastal flood defense. *Climatic Change 144*, 347–364.

Woodroffe, C., K. Rogers, K. McKee, C. Lovelock, I. Mendelssohn, and N. Saintilan (2016). Mangrove sedimentation and response to relative sea-level rise. *Annual Review of Marine Science 8*, 243–266.

Wright, L. and A. Short (1984). Morphodynamic variability of surf zones and beaches: a synthesis. *Marine Geology 56*, 93–118.

Yates, M., G. L. Cozannet, and N. Lenotre (2011). Quantifying errors in long-term erosion and inundation hazard assessments. *Journal of Coastal Research, Special Issue 64 64*, 260–264.

Yates, M. L., R. T. Guza, and W. C. O'Reilly (2009). Equilibrium shoreline response: Observations and modeling. *Journal of Geophysical Research: Oceans 114*(9), 1–16.

List of Figures

List of Tables

A

The Caribbean: a regional perspective

A.1. Climate change impact

The Caribbean Islands have been formed by tectonic movement of the Caribbean plate, which has created a diverse system of island arcs (Bachmann, 2011). Nowadays the Caribbean Island States consist of 30 territories (see Figure 3.1a), both sovereign and dependent territories, inhabited by around 43 million people in 2015 (United Nations, 2017), and part of the SIDS. The SIDS can be characterized by their insularity and remoteness, environmental factors, limited disaster mitigation capability, and demographic and economic structure (Pelling and Uitto, 2001, Karmalkar et al., 2013). For the Caribbean Islands, more than 50% of the population lives within 1.5 km of the shore (Mimura et al., 2007), and in 2011 14% of the total GDP was generated by tourism (Scott et al., 2012).

A growing body of literature has assessed the potential climate change impact for the Caribbean. For example, vertical accretion of Caribbean coral reefs is controlled by SLR and projections indicate how SLR may surpass accretion rates of 0.46-4.87 mm yr^{-1} (Perry et al., 2018). Also, mangroves species, abundant in the Caribbean, have a critical submergence rate for which substrate can no longer follow SLR. Although Caribbean mangroves have persisted SLR during the past 7,000–8,000 years (Woodroffe et al., 2016), some have hypothesized that a 8 mm yr^{-1} SLR may cause widespread mangrove drowning (Parkinson et al., 1994). In terms of socio-economic impact, 1 meter of SLR may displace over 110,000 people in the Caribbean and especially the vital tourism industry is found vulnerable with 49% of all coastal resort properties within a 50 meter erosion setback (Scott et al., 2012). In addition, retreat of coastlines may directly affect turtle nesting spots and historical and culturally important places (Fish et al., 2005, Mueller and Meindl, 2017).

A.2. Past sea-level rise research

Earlier work have made region-wide estimates of SLR in the Caribbean over the 20th century and early 21st century. From tidal gauge stations, a trend of ~2 mm yr^{-1} from 1950-2008 was found over the Caribbean Sea, consistent with the global average (Palanisamy et al., 2012). Moreover, from a reconstruction based on a combination of satellite altimetry, tidal gauges and ocean circulation models, a basin-wide SLR trend of 1.7 ± 0.6 mm yr^{-1} was reported for 1993-2009 (Palanisamy et al., 2012). However, trends deviate regionally up to 4-5 mm yr^{-1} along the south Caribbean islands. A similar approach by Torres and Tsimplis (2013) reported a basin-wide value of 1.7 ± 1.3 mm yr^{-1} over the altimetry era.

Using the most recently available altimetry product by Quartly et al. (2017) for the period 1993-2015 (Figure A.1a), the regional pattern of SLR is made visible including the uncertainty (Figure A.1a&A.1b). A larger trend is detected in the lower basin and a lower trend in the middle of the basin. The contribution of GIC and GIC in the region is lower than the global average (Slangen et al., 2014). These two contributions have dominated land ice loss over the altimetry era (Dieng et al., 2017), which could partly explain the lower than global average value in the region.

Moreover, on time scales of decades, factors such as interannual and interdecadel variability and ocean dynamics play a role. In fact, interannual sea-level variability accounts for 34% of the total variability in the region (Torres and Tsimplis, 2013). For instance, El Niño is known to influence low frequency variability in sea-levels in the region (Losada

et al., 2013, Palanisamy et al., 2012). Others have showed how sea-level variability is attributed to low frequency motion of tidal constituents that amplify tidal ranges on decadal time scales (Torres and Tsimplis, 2011), and eddies and meanders in the mean flow (both locally and remotely generated) (Carton and Chao, 1999, Alvera-Azcárate et al., 2009). Moreover, Torres and Tsimplis (2013) founds evidence that the Caribbean current has slowed down by 20% from 1993-2010. Because the current is directed from east to west (implying a north-south sea-surface gradient with lower values in the south), slowing down of the current may relax the sea-surface gradient and cause, respectively, larger SLR in the south and a sea level drop in the north (as observed). The largest factor that determines the spatial variability can be attributed to the steric variability, dominated by thermosteric increase (Torres and Tsimplis, 2013), and changes in wind stresses that drive coastal upwelling north of the South American continent (Jouanno and Sheinbaum, 2013). Because of a decrease in wind stress, this vertical upwelling has slowed down causing higher local steric trends in the southern part of the basin in line with satellite observations.

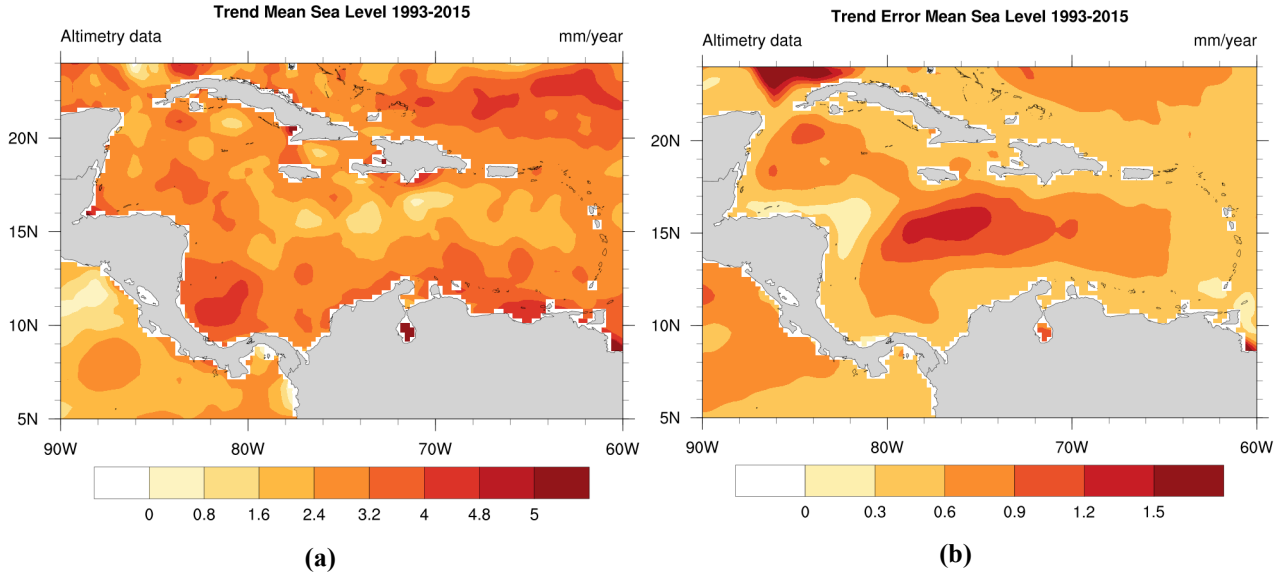

Figure A.1: Regional mean sea level trend over the years 1993-2015 expressed in mm/year. Right indicates the 90% error in the sea level trend, also in mm/year. Data courtesy: Climate Change Initiative, European Space Agency, product: SLA-v2 (Quartly et al., 2017).

A.3. Future sea-level rise

Until now, no region-specific SLR projections have been made. A few tidal stations in the Caribbean (U.S. Virgin Islands) are included in the most recent NOAA-projection (Sweet et al., 2017). Under an intermediate scenario of 1.0 m GMSLR, SLR will increase regionally by approximately 0.1 m for 2100, whereas under an extreme scenario of 2.5 m (globally), this additional regional effect is in the order of 0.7 m for the same year. The non-linear regional amplification in the NOAA-projections can be explained by the large sensitivity to mass loss from the AIS. Several remarks can be made concerning these projections. The Caribbean is only partially included and needs further investigations that cover the entire area. Moreover, although an extreme scenario is included in the projections, they do not yet include extreme scenarios of rapid ablation of the AIS as described by for example DeConto and Pollard (2016).

In summary, observed SLR rates in the Caribbean show slightly lower to comparable rates with globally-average observations. For future projections, an above global average SLR is to be expected, primarily due to sensitivity to mass loss from the AIS. Finally, nonstationarities in sea-level in the region at shorter time scales up to 40 years (Torres and Tsimplis, 2013) may be important at some coastal sites.

B

Sea-level rise projections

In the appendix, the method for deriving the SLR projection is considered. This is an extension to chapter 4.1. The contribution to SLR is given by a parameter X_i with i the contribution. All numbers presented are relative to the 1986-2005 average values, to be consistent with Church et al. (2013).

B.1. Cryosphere components and Land water

B.1.1. Glaciers and Ice Caps

Glaciers and Ice Caps (GIC) comprise the mountain glaciers and smaller ice caps that contribute to SLR. These glaciers are fed by precipitation and despite the small fraction of total ice, their fast response time makes it an important contribution to SLR on decadal to centurial time scales (Oerlemans and Fortuin, 1992).

This contribution is computed in the same way as Church et al. (2013). It excludes Antarctic glaciers that are included directly in the Antarctic contribution but includes Greenland glaciers. Four global glacier models are used (Giesen and Oerlemans, 2013, Marzeion et al., 2012, Radic et al., 2014, Slangen and van der Wal, 2011). We first need to fit the time series of cumulated contribution to $fI(t)^p$, with $I(t)$ the time integral of GMST from year 2006 to t. The integrated temperature needs to be used here because the cumulated sea level contribution depends on past temperatures. The fitting parameters f and p obtained for each model are shown in Table B.1. This method allows to apply these four models for any temperature pathway. In particular for the RCP scenarios:

$$I(t) = \int_{2006}^{t} T_{1986-2005} dt', \tag{B.1}$$

$$X_{gic}(t) = x^0_{gic} + \frac{10}{4} N_2 \sum_{i=1}^{4} f_i I(t)^{p_i} \tag{B.2}$$

where X_{gic} is a random variable representing the sea level change in cm and i is an index looping over the four sets of parameters from the glacier models. The factor 10 is used to convert from mm to cm. The spread of the four model estimates around the mean is about 20%. This uncertainty is included with the random variable N_2 that follows the distribution $\mathcal{N}(1, 0.2^2)$. The variable N_2 is independent from N_1 (see main text), which means that glacier modelling uncertainties are not correlated with temperature. The random variable X_{gic} is still partially correlated with temperature because $T_{1986-2005}$ is used to compute I. An additional constant ($x^0_{gic} = 0.95$ cm) is added to include the change from

Global Glacier Model	f (mm K^{-1} yr^{-1})	p (-)
Giesen and Oerlemans (2013)	3.02	0.733
Marzeion et al. (2012)	4.96	0.685
Radic et al. (2014)	5.45	0.676
Slangen and van der Wal (2011)	3.44	0.742

Table B.1: Four global glacier models used including the fitting parameters used.

1996 to 2005.

B.1.2. Greenland Surface Mass Balance

The Greenland SMB currently dominates the mass loss from the Greenland Ice Sheet (GIS) and early 21st century mass loss (2002-2011) was over six-fold that of the preceding decade (van den Broeke et al., 2017). A parametrization between temperature and mass loss ($\dot{X}_{Gsmb}$) is used to simulate the retreat of the whole ice sheet following Fettweis et al. (2013), and can be though of as a balance between mass gained from precipitation and loss from meltwater run-off.

$$\dot{X}_{Gsmb}(t) = \frac{10^{-10}}{\rho_w A_{oc}} \left(71.5 T_{1980-1999}(t) + 20.4 T^2_{1980-1999}(t) + 2.8 T^3_{1980-1999}(t)\right), \tag{B.3}$$

where the factor 10^{-10} is used to convert GT to kg and m to cm, $\rho_w = 1 \times 10^3\,\mathrm{kg\,m^{-3}}$ is the water density and $A_{oc} = 3.6704 \times 10^{14}\,\mathrm{m^2}$ is the ocean surface area. This equation is then integrated in time:

$$X_{Gsmb}(t) = x^0_{Gsmb} + U_1 L \int_{2006}^{t} \dot{X}_{Gsmb}(t')dt' \tag{B.4}$$

where x^0_{Gsmb} is the observed contribution between 1996 and 2005. To represent the difference between regional models, an additional uncertainty is added, L. L is a random variable sampled from the lognormal distribution $\mathrm{e}^{\mathcal{N}(0,0.4^2)}$. A positive feedback between SMB and surface topography is also added. As the ice sheet loses mass its altitude decreases and the temperature at its surface increases, leading to increased melt. This is included with U_1 that is a random variable following the uniform probability distribution between 1 and 1.15.

B.1.3. Antarctic Surface Mass Balance

The AIS is the largest reservoir of frozen fresh water on Earth (Ligtenberg et al., 2013). For a first order estimate, the SMB is exclusively driven by changes in precipitation over the ice sheet and is assumed to follow a linear relation with temperature increase (Lenaerts et al., 2016). The hydrological cycle is expected to intensify leading to snowfall-rich winters on the one hand, and warmer, melt rich, summers on the other hand. Results provided by Gregory and Huybrechts (2006) estimate a 5.1 $\pm$1.5% increase in precipitation per degree of warming. Surface run-off is omitted in this estimate, as mass gain will dominate strongly over projected run-off losses in a warmer climate due to strong refreezing effects (Ligtenberg et al., 2013). The ratio of warming in Antarctica compared to GMST was taken to be 1.1 $\pm$ 0.2. The Antarctic SMB contribution to sea-level is then computed as:

$$X_{Asmb}(t) = -x^{ref}_{Asmb} N_3 N_4 T_{1986-2005}(t), \tag{B.5}$$

with x^{ref}_{Asmb} the accumulation during the reference period taken to be $1923\,\mathrm{Gt\,yr^{-1}}$, N_3 and N_4 uncertainties following respectively $\mathcal{N}(5.1, 1.5^2)$ and $\mathcal{N}(1.1, 0.2^2)$. A minus sign is added because this accumulation of water on Antarctica brings sea-level down.

B.1.4. Land water changes

Land water changes are based on projections of future dam constructions and depletion of groundwater from human activities. The 5 to 95% quantiles for 2100 are -1 and 9 cm (Wada et al., 2012). The time evolution is done with a second order polynomial starting from present observed rate estimates of 0.26 - 0.49 mm $\mathrm{yr^{-1}}$ (5-95% range). A lower (upper) time series is constructed that start at the lower (upper) initial rate and end at the lower (upper) final estimate. These time series are called x^{lower}_{grw} and x^{upper}_{grw}. A central estimate (x^{cen}_{grw}) is obtained as the mean of the two. The final distribution is then computed as:

$$X_{grw}(t) = x^{cen}_{grw}(t) + \sigma_{grw}(t) N_5 \tag{B.6}$$

where N_5 is sampled from $\mathcal{N}(0,1)$ and with

$$\sigma_{grw}(t) = \left(\frac{x_{grw}^{upper}(t) - x_{grw}^{lower}(t)}{\alpha_{95} - \alpha_{05}} \right) \tag{B.7}$$

and α_q is the quantile function for a normal distribution. The land water contribution is taken independent of temperature and emission scenario.

B.1.5. Greenland Ice Sheet Dynamics

Greenland dynamic estimates were derived from modelled future responses of four major outlet glaciers on the ice sheet (Jakobshavn, Helheim, Kangerlussuaq, and Petermann), and further extended to all glaciers. Based on an expert assessment of the literature, the range of the Greenland ice sheet dynamical processes contribution for 2100 is 1.4 to 6.3 cm for all scenarios, except RCP8.5 for which it is 2 to 8.5 cm. The mass loss rate at the beginning of the projection is taken as half of the observed rate from 2005 to 2010 (half of 0.46-0.80 mm yr^{-1}), the other half being accounted for in the SMB (van den Broeke et al., 2009). A maximum (minimum) time series is then built starting in 2006 from the maximum (minimum) estimate of recent mass loss and ending in 2100 at the maximum (minimum) of the range for 2100 and assuming second order in time. These maximum and minimum time series are called x_{Gdyn}^{max} and x_{Gdyn}^{min} respectively. An additional 0.15 cm is added for the contribution before 2006 (x_{Gdyn}^{0}). The distribution is then taken as uniform between the maximum and minimum time series as follows:

$$X_{Gdyn}(t) = x_{Gdyn}^{0} + \left[U_2 x_{Gdyn}^{max}(t) + (1 - U_2)\, x_{Gdyn}^{min}(t) \right] \tag{B.8}$$

where U_2 follows a uniform probability distribution between 0 and 1, $U_2 \sim \mathcal{U}(0,1)$.

B.1.6. Antarctic dynamics

As mentioned, three different sources are used for the three scenarios of Antarctic dynamics; based on the IPCC (Church et al., 2013), based on Levermann et al. (2014) and based on DeConto and Pollard (2016).

IPCC The IPCC estimates the contribution to be -0.02 - 0.185 m in 2100 with equal probability (uniform distribution U_3). Because a small part of the accumulation of the SMB drains to the glaciers and contributes to increased dynamic loss, an uniform distribution, $U_4 \sim \mathcal{U}(0, 0.35)$, is add to account for this (i.e. on average 17.5% of the surface mass gain drains to the ocean). This is therefore indicated with a negative sign to avoid double counting. Again, a uniform distribution was used to account for the uncertainty, so the contribution reads:

$$X_{Adyn}^{IPCC}(t) = \left[U_3 X_{Adyn}^{max}(t) + (1 - U_3) X_{Adyn}^{min}(t) \right] - U_4 X_{Asmb}(t) \tag{B.9}$$

Similar to the Greenland dynamics, a second order polynomial is constructed that starts at the recent observed rates of mass loss. The starting point here is at 0.21-0.61 mm yr^{-1}. Moreover, the contribution is independent of RCP scenario.

LEV14 In the Levermann et al. (2014) case, the Antarctic dynamics is modelled using response functions from three ice sheet models that have a representation of ice shelves. This is because the other overestimate the melt along the ice shelves (Levermann et al., 2014). These models are the Pennsylvania State University 3-D ice sheet model (PenState-3D), the Parallel Ice Sheet Model (PISM) and the SImulation COde for POLythermal Ice Sheets (SICOPOLIS). The linear response curve of the AIS contribution for every year is written as a function of the response function R and the basal melt Δb along the coastline:

$$X_{Adyn}^{LEV2014} = \int_{1950}^{t} \Delta b(\tau) R_i(t - \tau) d\tau \tag{B.10}$$

Δb is linked to GMST by replacing it by a random variable U_5 that represent the possible basal melt rate reported in literature, given by $U_5 \sim \mathcal{U}(7, 16)[myr^{-1}K^{-1}]$. This term is then multiplied by the GMST and a factor α_m representing the conversion from GMST to ocean warming in front of the coastline. This value is for every sample randomly taken from one of the CMIP5 models. Together it reads:

$$X_{Adyn}^{LEV2014} = \int_{1950}^{t} U_5 \alpha_m T(\tau) R_i(t-\tau) d\tau \tag{B.11}$$

In the original paper, a case with and without a time delay τ was considered. For simplicity here, only the case without time delay is used, although the results do not differ much (Levermann et al., 2014).

DP16 The numerical model by DeConto and Pollard (2016) includes both SMB and ice sheet dynamics. In their high-end estimate, the expected values for the Antarctic contribution in 2100 relative to 2000 are 58 cm and 114 cm, with standard deviations 28 cm and 36 cm, respectively, for the RCP4.5 and RCP8.5 scenarios. The standard deviations stated above represent the uncertainty in three important parameters of an ice flow model: ocean melting under the ice shelves, hydrofracturing due to surface melting and horizontal wastage due to ice-cliff structural failure. A PDF can then be constructed for the Antarctic contribution to SLR at year t:

$$X_{DP16}^{Sce}(t) = x_{DP16}^{Sce}(t) + \sigma_{DP16}^{Sce}(t) N_6 \tag{B.12}$$

with x_{DP16} the expected value, σ_{DP16} the standard deviation and N_6 randomly chosen from a standard normal distribution ($\mathcal{N}(0, 1)$). Sce is the climate scenario that can either be the RCP4.5 or the RCP8.5 scenario. The reference period from DeConto and Pollard (2016) is slightly different from the one used by the IPCC AR5, but mass loss in Antarctica from 1996 to 2005 is very small (0.25 cm, Church et al. (2013)), and this is not taken into account. A fifth order polynomial is constructed over the years.

For the DP16T case, the Antarctic ice sheet mass loss is linearly related to GMST for a given emission scenario, assuming the following relationship:

$$X_{DP16T}^{Sce}(t) = X_{DP16}^{Sce}(t) + \delta \sigma(\mathbf{T}^{Sce}(t, .)) N_1 \tag{B.13}$$

$$\delta = \frac{x_{DP16}^{RCP8.5}(t) - x_{DP16}^{RCP4.5}(t)}{\overline{\mathbf{T}}^{RCP8.5}(t) - \overline{\mathbf{T}}^{RCP4.5}(t)}. \tag{B.14}$$

N_1 and comes from Equation 4.1, with the $\overline{\mathbf{T}}$ and $\sigma(\mathbf{T}^{Sce}(t, .))$ the mean and standard deviation of GMST. For complete consistency with DeConto and Pollard (2016), the mean temperature used to compute δ should come from their climate model, GENESIS v3 Global Climate Model. However this model it not part of CMIP5, therefore we have taken the ensemble mean of the CMIP5 models instead.

B.2. Global steric expansion

Steric expansion is the ocean expansion or contraction due to temperature or salinity changes. Global mean steric expansion is computed from the climate models in the same way as Church et al. (2013). From each model and at all time t, global mean steric expansion is stored in a matrix $\mathbf{X}_{st}$. The distribution is computed in the same way as for GMST:

$$X_{st}(t) = \overline{\mathbf{X}}_{st}(t) + \gamma \sigma(\mathbf{X}_{st}(t, .)) N_{1,corr}. \tag{B.15}$$

The random variable $N_{1,corr}$ is derived from the random variable N_1 in Eq.4.1, indicating that global mean surface temperature and steric expansion are assumed partly correlated. We found a correlation of 0.4, on average, for Sint Maarten from the climate models. Therefore, $N_{1,corr}$ is sampled from:

$$N_{1,corr} = \rho N_1 + N_I\sqrt{1-\rho^2}, \tag{B.16}$$

where N_I is an independent random variable with distribution $\mathcal{N}(0,1)$ and ρ is the correlation coefficient, in this case 0.4.

B.2.1. Ocean dynamics

Changes in the ocean circulation (wind and ocean currents) influence the sea-level regionally (ocean dynamics). In the Caribbean, the ocean dynamics will change due to a further reduction of the Caribbean Current (Brunnabend et al., 2017), and due to a weakening of the AMOC, less heat is pulled from the South Atlantic to the North Atlantic, leading to changes in dynamic sea-level (Hu and Bates, 2018). The ocean dynamic component is taken regionally from the climate models in the same way as Church et al. (2013) and similar to the steric component and GMST. Changes in ocean dynamics are derived regionally from CMIP5 models by averaging over an area [14-21°N, 61-67°W].

$$X_{dyn}(t) = \overline{\mathbf{X}}_{dyn}(t) + \gamma\sigma(\mathbf{X}_{dyn}(t,.))N_7. \tag{B.17}$$

B.2.2. Inverse Barometer

The IB effect is static response of the oceans to atmospheric pressure loading, with a increase in pressure locally resulting in a minor drop in sea level. The inverse barometer is taken locally for Sint Maarten.

$$X_{ib}(t) = \overline{\mathbf{X}}_{ib}(t) + \gamma\sigma(\mathbf{X}_{ib}(t,.))N_8. \tag{B.18}$$

B.3. Total

All components are added to calculate regional sea level rise. The Cryosphere components and Land water components are multiplied with their fingerprint value $F(\lambda,\phi)$:

$$\begin{aligned} X_{total} = X_{st} + X_{dyn} + X_{ib} + F(\lambda,\phi)X_{grw} + F(\lambda,\phi)X_{gic} + F(\lambda,\phi)X_{Asmb} \\ +F(\lambda,\phi)X_{Gsmb} + F(\lambda,\phi)X_{Gdyn} + F(\lambda,\phi)X^i_{Adyn} \end{aligned} \tag{B.19}$$

with i one of the three cases of Antarctic ice sheet dynamics.

B.4. Vertical land movement

Vertical land movement is a complex concept in this area. Tectonic movements have the potential to create abrupt vertical shifts (Milne and Peros, 2013), and local uplift rates are mentioned by Khan et al. (2017) such as 30m/Ma (million yr) in northern Puerto Rico, 25-60 m/Ma in the Cayman Islands and 26-54 m/Ma in Curacao. Previous studies have accounted differently for vertical land movement. For example, Simpson et al. (2010) used a rate of 3.1 mm/year for all areas without substantiation The study of Reguero et al. (2015) used a global model of isostatic adjustment from Peltier (2000) for the region. Nowadays, GPS tracking, for example by JPL (https://sideshow.jpl.nasa.gov/post/series.html), make it possible to obtain data on movement. Here, a comparison is made between NOAA vertical land movement estimates (Sweet et al., 2017), JPL, and Santamaria-Gomez et al. (2017). No consistency between sources is found at the overlapping sites. Further, GIA is almost negliglible in the region with the Peltier (2000) ice model only finding values of -0.2 (fall) - +0.3 (uplift) mm yr^{-1}. Therefore, no extra vertical land movement is used here.

C

Probabilistic erosion model

C.1. Storm surge

The storm surge S is defined as the water level elevation above mean water level and is composed of:

$$S = \eta_a + \eta_{sur} + \eta_{wis} + \eta_{was} \tag{C.1}$$

with η_a the atmospheric tide, η_{sur} the atmospheric surge, η_{wis} the wind-induced set-up, and η_{was} the wave-induced set-up. η_a and η_{sur} are discussed in the main text.

Wind set-up η_{wis} is added to account for an extra wind set-up over the shelf that is too narrow to be resolved in the global model that calculates η_{sur}. Wind set-up is given by a simple equilibrium balance:

$$\rho g h \frac{d\eta_{wis}}{dx} = \tau_{wind} \tag{C.2}$$

with τ_{wind} the wind shear stress, h the shelf depth, x the shelf distance, ρ is density of water $1025\,\mathrm{kg\,m^{-3}}$ and g the gravitational constant $9.81\,\mathrm{m\,s^{-2}}$. The Anguilla Bank in the east has a almost uniform shelf depth of 30 m and approximate width of 30 km (from the shoreline). The wind shear stress is found by:

$$\tau = C_d \rho_{air} u_{10}^2 \tag{C.3}$$

with ρ_{air} the density of air $1.22\,\mathrm{kg\,m^{-3}}$, u_{10} the wind speed at 10m and C_d the drag coefficient. C_d is dependent on wind speed and for this the formula by Large and Pond (1981) is adopted:

$$C_d = 1.2 \cdot 10^{-3} \qquad for \quad 4 < u_{10} < 11\,\mathrm{m\,s^{-1}} \tag{C.4}$$

$$C_d = 10^{-3}(0.49 + 0.065 u_{10}) \qquad for \quad 11 < u_{10} < 25\,\mathrm{m\,s^{-1}} \tag{C.5}$$

Wave set-up η_{wis} is calculated by applying the formula presented in by Dean and Dalrymple (2001):

$$\eta_{was} = \frac{40 - 3\gamma_b^2}{128} \gamma_b H_b \tag{C.6}$$

with H_b being the depth at breaking and γ_b the breaker index. This formula solves the set-up due to a transfer of wave momentum from the breaking waves to the water column on a sloping shoreface. For H_b the empirical breaking wave predictor proposed by Larson et al. (2010) is picked. Both the wave height and wave direction at breaking (indicated by subscript b) are functions of the deep water values (indicated by subscript 0) following:

$$H_b = \lambda_b C^2 / g \tag{C.7}$$

$$\alpha_b = asin(sin(\alpha_0)\sqrt{\lambda_b}) \tag{C.8}$$

The value λ_b is empirically derived via:

$$\lambda_b = \Delta(cos(\alpha_0)/\theta)^{2/5}) \tag{C.9}$$

where,

$$\theta = \left(\frac{C_0}{\sqrt{gH_0}}\right)^4 \left(\frac{C_0}{C_{g,0}}\gamma_b^2\right) \tag{C.10}$$

$$\Delta = 1 + 0.1649\xi + 0.5948\xi^2 - 1.6787\xi^3 + 2.8573\xi^4 \tag{C.11}$$

$$\xi = (cos(\alpha_0)/\theta_0)^{2/5} sin(\theta_0^2) \tag{C.12}$$

C_0 is the deep water wave celerity $C_0 = 1.56T_p$ and $C_{g,0}$ the deep water group celerity, $C_{g,0} = C/2$.
γ_b is given by the solution proposed by Battjes (1974) for steep beaches:

$$\gamma_b = 1.062 + 0.137log(\varepsilon_0) \tag{C.13}$$

with ε_0 the surf similarity parameter $(tan(\alpha_{fs})/(H_0/L_0))$ in deep water. α_{fs} is the bottom slope of the foreshore, which is taken for both beaches from Boon and Green (1988). L_0 is the wave length in deep water, which is given by linear wave theory $((gT_p^2)/(2\pi))$.

C.2. Copula

A copula can be defined as a joint distribution function on unit scale [0 1]. To scale a variable from the original scale to the copula scale, a kernel estimator of the cumulative distribution function can be used.

The transformed variables, for instance X_i and X_j, can be fitted to any copula with joint distribution function:

$$F_{X_i,X_j}(X_i, X_j) = \mathbf{C}_\theta[F_{X_i}(X_i), F_{X_j}(X_j)] \tag{C.14}$$

with C the copula function and θ the fitting parameter(s) (depends on copula family).

Goodness-of-fit The goodness-of-fit test that we applied is described by Genest et al. (2009) and is based on the *Cramèr-von Mises* $\mathcal{M}$ statistic between the empirical and parametric copula. Consider a sample with length n, $\mathcal{M}$ can be calculated from:

$$\mathcal{M}_n(\mathbf{u}) = n \sum_{|u|} (\mathcal{C}_{\hat{\theta}}(\mathbf{u}) - \mathcal{B}(\mathbf{u}))^2, \quad \mathbf{u} \in [0\ 1]^2 \tag{C.15}$$

with $\mathcal{C}_{\hat{\theta}}$ the parametric copula and $\mathcal{B}(\mathbf{u}) = \frac{1}{n}\sum_{i=1}^{n} \mathbf{1}(U_i \leq \mathbf{u})$ the empirical copula. Lower values of $\mathcal{M}$ indicate a better fit.

***t*-copula** For the SSTS, the *t*-copula is chosen. This copula is part of the family of copulas known as the elliptical copula. It is given by:

$$\mathbf{C}(u) = t_{v,\sum}\left(t_v^{-1}(u_1), \dots, t_v^{-1}(u_n)\right) \tag{C.16}$$

with $\sum$ the fitted $4x4$ correlation matrix between the storm characteristics and t_v the student-t distribution with v degrees of freedom. The *t*-copula has both an upper and lower tail dependency.

C.3. Erosion formula: Kriebel and Dean 1993

We solve the convolution integral similar to the method described in Kriebel and Dean (1993). To do this, a few calculation steps are performed. First of all, the storm forcing, i.e. storm surge and duration, are assumed to follow an

approximate sin-squared function $f(t) = sin^2(\sigma t)$ over its duration D, with $\sigma = \pi/D$. The convolution integral then reads:

$$R(t) = \frac{R_\infty}{T_s}\int_0^t sin^2\sigma(\tau)e^{-(t-\tau)/T_s}d\tau \tag{C.17}$$

This solution can be solved as a function of β, which reads:

$$\beta = 2\pi\frac{T_s}{D} \tag{C.18}$$

with T_s the representative erosion time scale of the exponential function. This β determines the morphological response of the beach relative to the hydrodynamics, and a large β results in a relatively large time lag. Moreover, larger β implies that the storm duration is relatively short compared to the representative erosion time scale. Thus, during the storm, only a small fraction of the potential erosion R_∞ is reached. We find β, by first finding T_s for a storm. This is given by:

$$T_s = 320\frac{H_b^{3/2}}{g^{1/2}A^3}\left(1 + \frac{h_b}{B} + \frac{mx_b}{h_b}\right)^{-1} \tag{C.19}$$

with h_b and H_b found again with the formula of Larson et al. (2010), A the parameter of the equilibrium profile and B the berm height. x_b is the surfzone width and is solved based on the equilibrium profile shape of the cross-shore profile:

$$x_b = x_0 + (\frac{h_b}{A})^{1/m} \tag{C.20}$$

$$x_0 = \frac{4A^3}{27tan(\beta_b)^3} \tag{C.21}$$

where m is the power of the equilibrium profile shape as proposed by Dean (1977):

$$h = Ax^m \tag{C.22}$$

with h the water depth and x the cross-shore distance. Morphological parameters A, m and $\tan(\beta_b)$ are taken from Boon and Green (1988) for the two beaches considered (A: 0.246/0.135; m: 0.61/0.77; $tan(\beta_b)$: 0.16/0.09; Dawn Beach/Orient Bay), while the B is estimated from satellite images in combination with the known $tan(\beta_b)$. This can then be used to solve to

$$R_\infty = \frac{S\left(x_b - (\frac{h_b}{tan(\beta_b)})\right)}{B + h_b - \frac{S}{2}} \tag{C.23}$$

By definition, the morphological response is also following a sinusoidal shape, but lagged and damped (theory convolution). The time of maximum erosion, t_m, provides the peak retreat distance of the beach during a storm. The corresponding R_{max} is found by:

$$R_{max} = R_\infty\frac{1}{2}(1 - cos(2\frac{\pi}{D}t_m)) \tag{C.24}$$

with t_m iteratively solved via:

$$exp\left(-\frac{2\pi t_m}{\beta D}\right) = cos(2\frac{\pi}{D}) - \frac{1}{\beta}sin(2\frac{\pi}{D}t_m) \tag{C.25}$$

C.4. Trend analysis storm parameters

The methodology described for deriving representative future storm events includes the assumption of having stationary conditions. Similar to water level variation, the wave climate may be prone to trends and interannual to multidecadel variability. In general, surface gravity waves consist of locally generated wind waves and remotely generated swell, where the latter component may not be directly linked to the local atmospheric changes (Semedo et al., 2011). Therefore, it is important to better understand the mechanisms of climate variability in the wave field and to justify the decision made to assume stationary conditions.

For the purpose here, the trends of the parameters η_{da}, H_s, T_p, u_{10} and S are assessed. This is done in terms of median values as well as the 90th percentile value for the the annual, winter (Nov-Apr) and summer (May-Oct) time series.

C.4.1. Results trend analysis

First, all parameters show a considerable variability over the years. For example, the $H_{s,50}$ has a 2.5% variability ($\frac{\sigma}{\mu}$) over the years, and $H_{s,90}$ a 3.3%. Altogether, the S has a 3.3% and 2.6% variability for the 50th and 90th percentiles. For these two parameters, the extremer values have a larger variability (also due to decreased sample size), both in winter and summer, with nearly equal variability for both seasons. In terms of absolute values the interannual variability (difference min and max) is up to 15 cm for H_s and 5 cm for S. Using a Fast Fourier Transform (FFT), no low frequency cycles could be identified apart from the a yearly and six monthly cycle (that represents the seasonality cycle).

The trends are shown in Figure C.1 with the annual (black), summer (red) and winter (blue) trends separated. Most trends are considered small, only in the order of a few mm/year for the H_s, η_{DA} and S. Changes in T_p and u_{10} are negligible. Interestingly, the η_{DA} has positive trends for both the winter and summer season, thereby contribution to the overall annual trend. H_s and S has a downward trend in summer, whereas is shows an upward trend in winter, compensating each other in the annual trend (both median and extremer values). However, since the largest storms occur in winter, this trend contributes to larger erosion potential in the future if it continues unhindered (not part of any multidecadal cycle). A similar analysis was done by Wahl and Plant (2015) for the Gulf of Mexico who found a contrasting pattern for H_s; upward trend in summer, downward trend in winter. Also, the overall trends are up to a magnitude higher in their work. In addition, the H_s trend found here is similar to the trends reported by Reguero et al. (2013).

Overall, the seasonal cycle of the wave height and total water levels seems to have slightly intensified over the years.

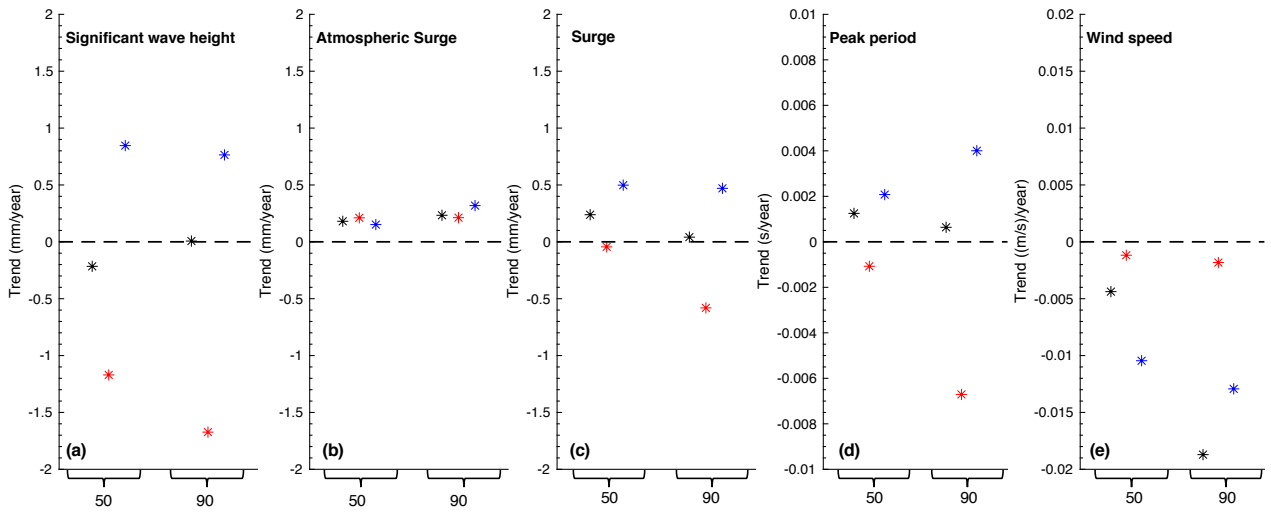

Figure C.1: Trends in storm parameters for annual (black), summer (red) and winter (blue) periods, for (a) H_s, (b) η_{DA}, (c) S, (d) T_p, (e) u_{10}. All trends are given for both the 50-percentile and 90-percentile

Still, the trends are almost negligible for all parameters, thus the assumption of stationary conditions is justified.

Moreover, the wave and wind climate can be influenced by large scale atmospheric circulation patterns (Semedo et al., 2011). Among the climate indices, the Nino3.4, TSA, NTA and NAO have a influence on the sea-surface height variability, with the latter also important for changes in the Atlantic Ocean from where most of the swell waves are originated. Annual and seasonal correlation coefficient are calculated from the monthly mean $H_{s,50}$ and $H_{s,90}$, with the monthly climate indices from http://www.esrl.noaa.gov/psd/data/climateindices/list/. No correlation was found except for the Nino3.4 index that has a negative correlation with the 50th percentile (90th percentile) waves, namely -0.33(-0.37) annually, -0.43(-0.34) during winter and -0.16(-0.36) during summer. The reason for this is outside the scope of this work, but a potential reason could be the interaction of El-Nino and hurricane activity over the Atlantic Ocean (e.g. Trenberth, 2005).

D

Results sea-level rise projections

D.1. Results other regions

RSLR projections are also made for other parts of the Caribbean Basin. Four areas are chosen based on criteria that they show similar rates of SLR from 1993-2015 (see figure A.1), have similar fingerprints values and a similar future ocean dynamics. Ocean dynamics are taken from the four boxes defined. Local fingerprints are taken from four 'points of interest' located inside the boxes.

The four areas are shown in figure D.1 and do coincide to a large extent with the different island groups in the Caribbean, henceforth indexed by their Roman number: (I) South Caribbean Sea [N 9-14°, W 73-83°], (II) Leeward Antilles [N 10-14°, W 61-73°], (III) Windward Islands [N 14-21°, W 61-67°], and (IV) Greater Antilles [N 14-22°, W 67-83°]. More specifically, points of interest for (II) and (III) coincide with the Dutch oversea islands of Curacao and Sint Maarten, while point of interest (I) is strategically chosen to concur with city of Colon, the northern exit of the Panama canal. In the table, the SLR-projections for the other three areas are provided. Results are comparable in great lines, with maximum differences of 9 cm in the 99 percentile and 5 cm in the 50 percentile.

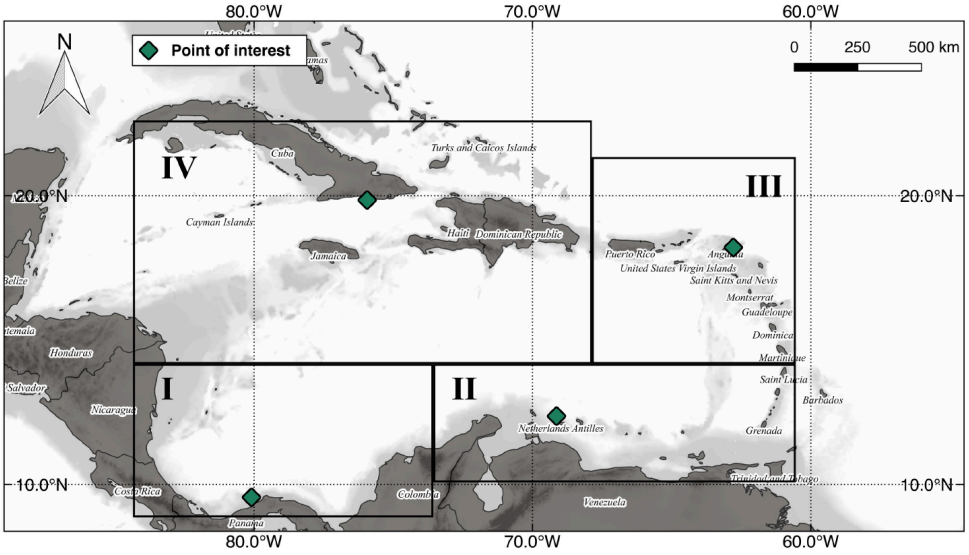

Figure D.1: Four area defined for sea level rise projections: I: South Caribbean Sea, II: Leeward Antilles, III: Windward Islands, and IV: Greater Antilles.

Area I									
RCP8.5	Regional			Global			Regional factor		
Percentile	DP16	LEV14	IPCC	DP16	LEV14	IPCC	DP16	LEV14	IPCC
5.0	136	56	52	123	57	54	1.11	0.98	0.96
50.0	200	85	78	175	79	73	1.14	1.08	1.07
95.0	265	126	106	228	113	95	1.16	1.12	1.12
99.0	292	154	119	250	136	106	1.17	1.13	1.12
RCP4.5									
5.0	66	38	36	61	39	37	1.08	0.97	0.97
50.0	109	59	56	96	55	52	1.14	1.07	1.08
95.0	152	89	77	132	79	69	1.15	1.13	1.12
99.0	170	111	85	146	97	75	1.16	1.14	1.13
Area II									
RCP8.5	Regional			Global			Regional factor		
Percentile	DP16	LEV14	IPCC	DP16	LEV14	IPCC	DP16	LEV14	IPCC
5.0	134	54	51	123	57	54	1.09	0.95	0.94
50.0	198	82	76	175	79	73	1.13	1.04	1.04
95.0	262	123	103	228	113	95	1.15	1.09	1.08
99.0	289	152	116	250	136	106	1.16	1.12	1.09
RCP4.5									
5.0	64	37	35	61	39	37	1.05	0.95	0.95
50.0	107	57	55	96	55	52	1.11	1.04	1.06
95.0	150	87	75	132	79	69	1.14	1.10	1.09
99.0	168	108	83	146	97	75	1.15	1.11	1.11
Area IV									
RCP8.5	Regional			Global			Regional factor		
Percentile	DP16	LEV14	IPCC	DP16	LEV14	IPCC	DP16	LEV14	IPCC
5.0	135	53	49	123	57	54	1.10	0.93	0.91
50.0	200	81	74	175	79	73	1.14	1.03	1.01
95.0	266	122	101	228	112	95	1.17	1.09	1.06
99.0	294	151	113	250	136	106	1.18	1.11	1.07
RCP4.5									
5.0	64	37	35	61	39	37	1.05	0.95	0.95
50.0	108	57	54	96	55	52	1.13	1.04	1.04
95.0	152	87	74	132	79	69	1.15	1.10	1.07
99.0	171	109	82	146	97	75	1.17	1.12	1.09

Table D.1: Results regional SLR projections for 2100 compared to 1986-2005 for areas I, II and IV. All results are shown for $\gamma = 1.0$

D.2. Contributions

To look at the individual contributors into more detail, the median and 90% bandwidth of the contributors are shown for Sint Maarten under both RCP-scenarios. One can clearly see that the Antarctic dynamics are the dominant source of SLR in case of DP16. In the IPCC and LEV14 cases, the uncertainty bandwidth is large but the expected value equally important as other sources such as Gsmb, Gdyn and GIS. The ocean steric contribution is the largest contribution in case of IPCC and LEV14 and second largest in case of DP16. The ocean dynamics has a median value close to zero, hence only adds up to the uncertainty bandwidth.

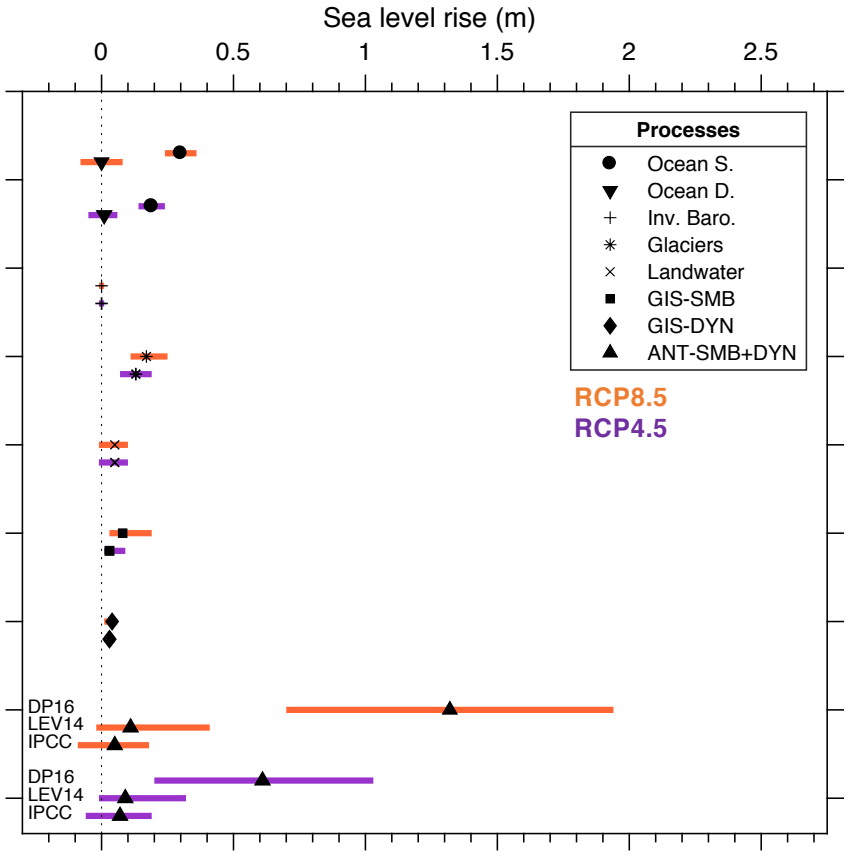

Contribution of the individual SLR components to the 2100 RSLR compared to 1986-2005. All results are shown for γ = 1.0

D.3. Comparison previous studies

To place the results into perspective, a comparison is made between findings of some earlier work, namely the regional projections (global coverage) made by Kopp et al. (2017), Slangen et al. (2014) and de Winter et al. (2017), who have all integrated different model assumptions (henceforth called K17, S14, dW2017). The percentiles in these studies are matched for complete comparison in Table D.2 ($\gamma = 1.0$). Primarily, differences among studies are due to different model design choices. K17 uses expert elicitation projections provided by Bamber and Aspinall (2013) (though scaled to IPCC likely range) and DeConto and Pollard (2016), S14 and dW17 both use the IPCC projections, while the latter study also incorporates the projections proposed by Ritz et al. (2015) and de Vries and van de Wal (2015). These projections are both skewed with slightly different median value, explaining the largest fraction of the model divergences. For example, Ritz et al. (2015) reports 11.9 - 29.6 cm, Levermann et al. (2014) 9 - 46 cm, while Bamber and Aspinall (2013) states 29 - 84 cm for the 50-95 percentile under RCP8.5 in 2100. Still, differences in AIS do not cover the entire field of discrepancies between the studies, implying that other model assumptions remain relevant. Surprisingly, while the S14 results are

in close compliance with our IPCC case, the model by dW2017 shows some alternation with lower median but higher upper ranges. These differences potentially arise from the method of combining different PDFs of individual contributors and the correlation structure between it. In their model set-up, they assume independence, while a correlation between contributors exists as was briefly discussed. Moreover, they state that increasing the correlation would lead to a smaller uncertainty. This is, however, from basic probability theory not feasible as the covariance between two variables always adds up to the total variance of the sum of the two ($+2COV(XY)$). Moreover, the K17 projections fall in between the median values for the two extremer scenarios of DP16 and LEV14 for RCP8.5, but surpass the models results for higher percentiles. This can, besides the AIS-contribution, be explained by the fact that they used different fingerprints (both WAIS and EAIS), slightly more CMIP5 models and further already include this factor γ = 1.64 for model uncertainty. For example, their DP16 90% range is 183 cm for RCP8.5 and 130 cm for RCP4.5, while our range is only 131 cm and 68 cm, respectively. If compared with the $\gamma = 1.64$ results in the table 5.1, a better compliance is found, although the DP16T case even exceeds the 95th percentile by 50 cm. At last, since the Bamber and Aspinall (2013) analysis is scenario-independent, its contribution for the RCP4.5 scenario will be relatively more, thereby almost doubling the 99th percentile compared to the IPCC case.

RCP8.5									
	Model simulations			Kopp et al. (2017)		Slangen et al. (2014)	de Winter et al. (2017)		
Percentile	DP16	LEV14	IPCC	DP16	BA13	-	IPCC	Ritz2015	VW2015
5	135	53	49	87	30	50			
50	200	80	74	156	76	72	67	72	86
95	266	121	100	270	139	94	109	111	146
97.5	279	133	105				117	119	164
99.0	294	150	112	302	190				
RCP4.5									
	Model simulations			Kopp et al. (2017)		Slangen et al. (2014)	de Winter et al. (2017)		
Percentile	DP16	LEV14	IPCC	DP16	BA13	-	IPCC	Ritz2015	VW2015
5	64	37	34	44	21	40			
50	108	57	54	96	58	55			
95	153	87	74	174	109	70			
99.0	171	109	82	203	153				

Table D.2: Comparison of model results (Area III) with earlier work on RSLR. Result from Kopp et al. (2017) are taken from the closest point to Area III, which corresponds with the U.S. Virgin Islands tidal gauge. Values of de Winter et al. (2017) have been included for all three Antarctic scenarios they have considered, namely incorporating those proposed by Church et al. (2013), Ritz et al. (2015) and de Vries and van de Wal (2015).

E

Results erosion

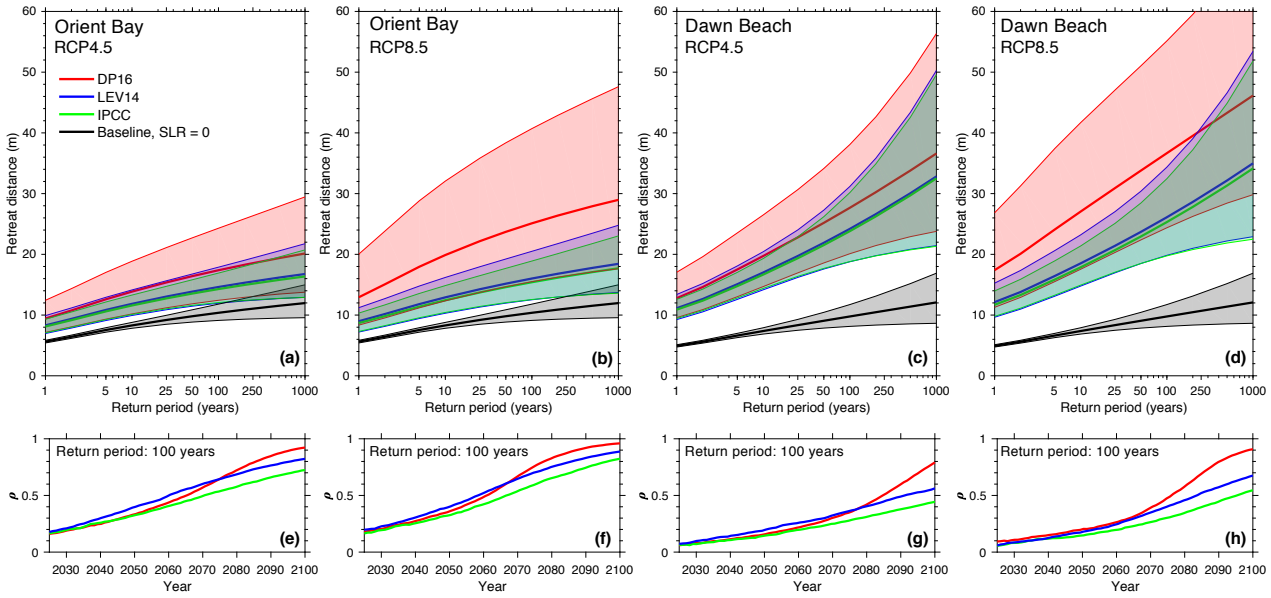

Figure E.1: (a) Return periods of retreat distance due to storm events over the period 2006-2100 for Orient Bay under RCP4.5. Solid line is the median value, whereas the shaded area represent the 90% uncertainty bandwidth. The black line is the baseline case for a situation without SLR. (b) same as (a) but under RCP8.5. (c-d) same as (a-b) but for Orient Bay. (e) Correlation between 2100 SLR and the calculated 1/100 year retreat distance for the 10,000 samples for Orient Bay under RCP4.5. (f) same as (e) but under RCP8.5. (g-h) same as (e-f) but for Dawn Beach. All figures are with considering additional model uncertainty ($\gamma = 1.64$).